

## **General Disclaimer**

### **One or more of the Following Statements may affect this Document**

- This document has been reproduced from the best copy furnished by the organizational source. It is being released in the interest of making available as much information as possible.
- This document may contain data, which exceeds the sheet parameters. It was furnished in this condition by the organizational source and is the best copy available.
- This document may contain tone-on-tone or color graphs, charts and/or pictures, which have been reproduced in black and white.
- This document is paginated as submitted by the original source.
- Portions of this document are not fully legible due to the historical nature of some of the material. However, it is the best reproduction available from the original submission.

FINAL REPORT

NASA Grant 21-002-308

Rocket Investigation of Relativistic  
Electron Precipitation (REP) Events

Author: David J. Simons

Principal Investigator: David L. Matthews

(NASA-CR-145609) RELATIVISTIC ELECTRON  
PRECIPITATION IN THE AURORAL ZONE Ph.D.  
Thesis (Maryland Univ.) 200 p HC \$7.50

N76-11608

CSCI 04A

Unclas

G3/46

03040

RELATIVISTIC ELECTRON PRECIPITATION IN THE AURORAL ZONE

by

David Simons

Dissertation submitted to the Faculty of the Graduate School  
of the University of Maryland in partial fulfillment  
of the requirements for the degree of  
Doctor of Philosophy

1975

APPROVAL SHEET

Title of Thesis: Relativistic Electron Precipitation in the  
Auroral Zone

Name of Candidate: David Simons  
Doctor of Philosophy, 1975

Thesis and Abstract Approved: David L. Matthews  
David L. Matthews  
Research Associate Professor  
Institute for Fluid Dynamics  
And Applied Mathematics

Date Approved: April 24, 1975



## ABSTRACT

Title of Thesis: Relativistic Electron Precipitation in the Auroral Zone

David Simons, Doctor of Philosophy, 1975

Thesis directed by: Professor David L. Matthews

The energy spectra and pitch angle distributions of electrons in the energy range 50 keV to 2 MeV have been determined by a solid state electron energy spectrometer during the Relativistic Electron Precipitation (REP) event of 31 May 1972. The experiment was carried aboard a Nike-Cajun sounding rocket as the University of Maryland component of a joint American-Norwegian (NASA-NDRE) ionospheric investigation.

The difficulty of determining the expected electron flux prior to the experiment required an instrument with a large dynamic range. The design and theoretical modeling of this instrument is described in great detail. The extensive preflight calibrations on the NASA-Goddard 2 MeV Van de Graaff electron-proton accelerator are compared with the theoretical model.

The electron pitch angle distributions are determined from a knowledge of the rocket aspect and the direction in space of the Earth's magnetic field. The rocket aspect determination is therefore treated in depth and a method is developed to compensate for the malfunctioning of the aspect magnetometer.

The electron fluxes during the REP event were highly variable demonstrating correlated energy, flux and pitch angle pulsations with time periods less than one second. Increases in flux were accompanied by marked filling of the loss cone at lower energies (near 50 keV). Within the time

resolution of the experiment, these fluxes were simultaneous with a hardening of the energy spectrum characterized by marked increases of the near relativistic electrons. The higher energy particles showed a much more pronounced loss cone than the lower energy particles during these flux increases. The procedures for determining these results from raw data count to final conclusion are also described.

Drawing upon the quasilinear equations of plasma wave-electron interactions, a theoretical model for the production of relativistic electrons is proposed. A self consistent set of fully relativistic equations for the evolution of the electron distribution function due to the interaction of the electrons with parallel propagating whistler waves is derived in the Appendix. An examination of these equations leads to the conclusion that at comparatively low background electron densities, the anomalous doppler resonance leads to the acceleration of near relativistic particles. The results of a computer solution of the five coupled integrodifferential quasilinear equations confirms this conclusion.

## ACKNOWLEDGEMENT

First and foremost I wish to express my gratitude to my wife Grace whose emotional and intellectual support, tolerance, and encouragement made it possible for me to pursue this work. My dissertation adviser, Dr. David L. Matthews, provided the opportunity to perform the research, able guidance to help bring it to fruition and most important the understanding and freedom that allowed me to grow with this undertaking.

I have learned from and profited so greatly from so many individuals in the course of this research that I can hardly do proper credit to any of them in this small space. My fellow graduate students Dr. Morris B. Pongratz and Dr. John Foster can be only second to my adviser in their contribution to my education. Mr. Carter Gibson and Mr. Clous Christoph designed and constructed all of the electronics. Mr. Carter Gibson was making final adjustments to the payloads when they were already secured to the rockets in Norway. My adviser, colleague and collaborator, Dr. Theodore Rosenberg provided ample aid, comfort and instructional guidance throughout the course of my work. The mechanical work was performed under the able direction of Mr. Ernest Grossenbacher in the IFDAM shop. I particularly wish to thank Mr. John Sisson for his great care and artistry in the construction of the collimators. Mr. Grossenbacher also provided his expertise generously during the early design stages of the mechanical assemblies. The silicon detectors were constructed at the University of Maryland in Dr. George Gloechler's detector laboratory. I particularly wish to thank Mr. Joseph Gigante and Mr. Robert Lungren for the patient work and particularly Mr. Joseph Gigante for sharing his vast store of knowledge of these devices with me. Mr. Gigante provided me with a great deal of advice and training

as to the operation, handling and understanding of solid state detectors. Another vast store of knowledge was provided to me by Mr. S. Brown at Goddard Space Flight Center, who so generously spent so much of his time in helping me prepare for and perform the numerous calibration procedures on the Van de Graaff acceleration. To the entire staff of the NDRE Rocket Range in Andenes, Norway, I am grateful for making our stay so pleasant and fruitful. I must particularly acknowledge the expert guidance of Mr. L. Lorntzen who so able directed the integration of all the experiments on the rockets F33 and F34. I thank Mr. J. Trøim and Dr. T. R. Larsen for their consultations and aid. Dr. L. Lanzerotti of Bell Telephone Laboratories was an enthusiastic collaborator who granted me a great amount of time, interest, training and support. The partial reflection experiment of the Auroral Observatory at Trømsø, Norway, proved to a very crucial adjunct to our experiment. Mr. A. Haug of the University of Norway, Trømsø, provided generously of his time and person in training us in the use of this facility. He made my short stay in Trømsø and Lavensdalen an experience I will always treasure.

I wish to thank Dr. D. Tidman and Dr. C. S. Wu for discussions at various times during the preparation of the theoretical material, and I particularly thank Dr. Wu for his careful reading of the appendix.

Mrs. Margaret Small and Mrs Margaret Keimig come at the end of the acknowledgements only because they have made the final contribution to this work. That they managed to interpret my often cryptographic script can only be miraculous. I am sincerely grateful for their expert typing of this thesis.

I am certain there are many others that I have managed to neglect, but I can only say I am grateful to all who have contributed to this undertaking.

## TABLE OF CONTENTS

Chapter	Page
I. INTRODUCTION.....	1
A. The REP Event.....	1
B. A Brief Review of Magnetospheric Structure.....	3
C. The Trapped Particle Population and the REP.....	6
D. The Organization of this Report.....	9
II. THE DESIGN AND CALIBRATION OF A NINE CHANNEL ELECTRON ENERGY SPECTROMETER.....	10
A. Choosing an Electron Detector.....	10
1. Criteria for Counting Capability.....	10
2. The Advantages of Solid State Detectors.....	11
3. Some Properties of Silicon Detectors.....	13
B. The Collimator.....	16
1. Geometrical Factor.....	16
2. Design of the Shielding.....	22
3. The Aluminum Light Shield.....	26
C. Effects of the Light Shield on Energy Resolution....	28
D. Modeling the Spectrometer Response Functions.....	37
E. Calibrations.....	48
1. The Determination of Optimum Performance.....	48
2. Final Calibrations.....	53
F. Energy Response of the Analyzer to Protons.....	62
G. PCM Telemetry.....	64
III. THE FLIGHT PARAMETERS OF ROCKET F-34.....	66
A. The Trajectory.....	66
B. Determining the Rocket Aspect.....	68
IV. DATA REDUCTION AND EXPERIMENTAL RESULTS.....	82
A. Data Overview.....	82
B. The REP and the PCA.....	86
C. Removing the Roll Dependence.....	91

Chapter	Page
D. The Energy Spectra.....	105
E. Energy and Pitch Angle Structure.....	111
F. Time Series Analysis.....	119
V. SOME THEORETICAL CONSIDERATIONS ON REPS.....	132
A. The REP and the Trapped Particle Population.....	132
B. The Whistler Dispersion Relations.....	134
C. The Quasilinear Diffusion Equations.....	138
D. The Implications of Pitch Angle Anisotropy.....	142
E. Scaling the Various Equations.....	145
F. The Effects of Low Density.....	146
G. Energy Diffusion and the Relativistic Case.....	147
H. Numerically Modeling the Quasilinear Diffusion Equations.....	149
I. Conclusions.....	154
APPENDIX A.1. Modeling the X-Ray Production in the Shielding.	156
APPENDIX A.2. Energy Scaling Parameter, $E_r$ .....	159
APPENDIX A.3. Angular Response of the Collimator.....	160
APPENDIX B. Derivation of a Fully Relativistic Quasilinear Diffusion Equation for Cyclotron Resonant Interactions.....	163



## LIST OF FIGURES

1. The Auroral Oval
- 2.1 The lithium drifted solid state detector.
- 2.2 The schematic collimator-detector geometry.
- 2.3 Cross-section of the cylindrical brass collimator showing the lead inserts and the position of the solid state detector.
- 2.4 Predicted x-ray spectra as seen by the 3 mm thick silicon detector with and without shielding.
- 2.5 Energy loss of electrons in  $270 \mu\text{g}/\text{cm}^2$  of aluminum.
- 2.6 Fraction of electrons transmitted through thin foils as a function of reduced energy.
- 2.7 Energy spectra of transmitted electrons through thin foils.
- 2.8 Most probable scattering angle of normally incident electrons transmitted through thin foils.
- 2.9 Total collection time for positive carriers in 3 mm of silicon at 180 volts bias potential as a function of electron energy.
- 2.10 The basic amplifier system.
- 2.11 The pulse height discriminator.
- 2.12 Amplifier output pulse height at constant input pulse height as a function of input pulse rise time.
- 2.13 Pulse height as a function of energy.
- 2.14 Pulse height spectrum from 150 kev electrons stopping in 3 mm of silicon.
- 2.15 Normalized pulse height spectrum of 150 kev electrons stopping in 3 mm of silicon.
- 2.16 The nine response functions for two spectrometers.
- 2.17 The angular response of the collimator to monodirectional electrons.

- 3.1. Trajectory of Rocket F-34.
- 3.2. Reduced data from the sun sensor.
- 3.3. Euler angles used to define transformations from space coordinates to coordinates fixed in the rocket.
- 3.4. Transformation to space coordinates with Z-axis in the sun direction.
- 3.5. Angles determined from the sun sensor measurement.
- 3.6. Precession cone of the rocket determined in the sun system.
- 3.7. Cross-correlation of the compliment of the pitch angle and the count rate for  $135^\circ$  detector as function of azimuth angle.
- 4.1. Unprocessed count rates for several channels and detectors.
- 4.2. Riometer record for REP.
- 4.3. Proton fluxes due the Polar Cap Absorption event.
- 4.4. The central pitch angle of detector and the count rates in channel 1 for each detector.
- 4.5. Geometrical quantities defining the pitch angle field of view.
- 4.6. The pitch angle response functions.
- 4.7. Typical pitch angle distributions determined over one roll of the rocket.
- 4.8. The average unidirectional flux over different portions of the flight.
- 4.9. Different representations of the energy spectra.
- 4.10. The integral flux shown in parallel with the average energy.
- 4.11. Pitch angle distributions over the peaks and valleys of the pulsations.
- 4.12. Pitch angle distributions over down coming particles as a function of time.
- 4.13. The variation of the energy spectra over the pulsations.

- 4.14. The effective frequency filter due to time averaged sampling.
- 4.15. Power spectral estimates over the averaged data set.
- 4.16. Power spectral estimates over the raw data set.
- 4.1. The approximate dispersion relation and the exact dispersion relation when  $\Omega_p = 26$  khz and  $\omega_p = 18$  khz.
- 5.2. Resonant parallel momentum as a function of frequency at two different electron densities.
- 5.3. The growth rate at two anisotropy ratios.
- 5.5. Rate of change of the distribution with cold density  $0.1/\text{cm}^3$  and anisotropy 1.25.
- A.1. Bremsstrahlung production in targets of  $R_0$  scaled from published results.
- A.2. Geometry for angular response of the collimator.

## CHAPTER I

### INTRODUCTION

#### I.A. The REP Event

The Relativistic Electron Precipitation (REP) event is a subclass of daytime auroral absorption belonging to the Slowly Varying Absorption (SVA) class of absorption events. It has a number of features that have set it aside as a fairly special form of magnetospheric-ionospheric phenomenon. Auroral absorption is the abnormal absorption of cosmic radio noise (CRN) in the ionosphere of the auroral zone as determined by a riometer (Relative Ionospheric Opacity meter). Absorption is caused by increased ionization in the lower ionosphere due to x-rays and precipitating energetic charged particles. The increased ionization leads to resistive dissipation of the transmitted signal (i.e., ionospheric absorption). An absorption event is any period of marked increased absorption.

Ever since Little and Leinbach (1959) developed a sufficiently stable receiver to make absorption measurements over a long period meaningful, ionospheric observers have been using the riometer to monitor ionospheric activity. Absorption events are normally characterized by the physical appearance of the printed riometer record. Hence the name slowly varying absorption characterizes the slow smooth decrease in signal intensity extending over as much as an hour and the usually slower recovery (one or two hours) to the normal level. This slowness during a daytime event is due in part to the sluggishness of the daytime ionosphere. As pointed out by Ansari (Ansari, 1965) this behavior sets these daytime events quite apart from the typical nighttime auroral absorption

which is characterized by rapid fluctuations in the signal intensity. The daytime SVA has been discussed extensively by Ansari (1965), Ortner and Riedler (1964) and Bewersdorff et al. (1968).

The REP event was first distinguished from other SVA's by Bailey and Pomerantz (1965) using a riometer in association with VHF forward scatter radar. The forward scatter experiment gives some idea of the depth of penetration into the atmosphere of the ionizing radiation which is causing the absorption.

Bailey and Pomerantz determined that ionizing particles were penetrating into the atmosphere to a depth below 70 km during certain SVA's. The fluxes of charged particles below the reflection height of the VHF forward scatter radar were sufficient to cause very large absorption of the scattered signal. By modeling the absorption mechanism they inferred that the effective atmospheric cutoff energy for electrons causing this absorption was about 400 Kev. Protons causing the same absorption would have had a cutoff of 10 Mev and were therefore considered much less likely. Bailey and Pomerantz therefore coined the expression Relativistic Electron Precipitation.

The REP is a distinctly daytime event meaning that the geographically widespread absorption is observed in the dayside auroral ionosphere. There is generally little or no local magnetic activity observed, (Ansari, 1965, Bailey, 1968) and REP's occur following the expansive phase of magnetospheric substorms as observed on the night-side of the Earth (Thorne, 1974). In order to put this in perspective we must dwell on the structure of the magnetosphere and define a few terms.

### I.B. A Brief Review of Magnetospheric Structure.

The solar plasma streaming by the Earth encloses the Earth's magnetic field in a cavity which we call the Magnetosphere. This essentially fluid type interaction of plasma and field draws out the Earth's field on the nightside into a long tail and compresses the field on the dayside confining it to something of the order of 10-12 Earth radii ( $R_E$ ). Within about  $6 R_E$  the magnetic field bears some resemblance to a dipole configuration (Dessler, 1968). Farther out than  $6 R_E$  field lines are extended toward the tail on the nightside and compressed on the dayside. A magnetic neutral sheet extends up the tail from about  $10 R_E$  and has been observed to exist well beyond  $80 R_E$  (Ness, 1969). Field lines that extend into the tail past the beginning of the neutral sheet are called open field lines and may very well merge with the solar wind magnetic field some point far downstream. It has not been established whether particles from the solar wind have direct access into the tail. The neutral sheet and the central portion of the tail are bathed in a plasma referred to as the plasma sheet. Within about  $4 R_E$  of the Earth is the stable trapping region which contains a plasma which is shielded from the fairly extreme fluctuations which are observed in association with magnetospheric storms. (Van Allen, 1969). This region has a cold plasma density of about  $100/\text{cm}^3$ . Except during storm conditions, there is a precipitous drop off in density between  $4 R_E$  and  $5 R_E$  called the plasmapause (Carpenter, 1966) where the density falls off to about  $1/\text{cm}^3$ . The region between  $5 R_E$  and the plasma sheet is the region of the magnetosphere that is connected by the magnetic field to the ionosphere of the Auroral Zone. This is a transition region between closed field lines and field lines that extend on the nightside into the magnetotail.



Drastic changes in the magnetic field and particle population of this region accompany magnetic substorms (see below) keeping the region in a state of change. Even during relatively quiet periods there seems to be continual acceleration of particles in this region as manifested by luminosity in the auroral zone. The auroral activity is caused by particles precipitating into the ionosphere at the feet of the field lines (Akasofu, 1968).

Particles trapped in the Earth's magnetic field drift around the Earth due to the gradient and curvature in the magnetic field (gradient drift). These drifting particles effectively connect opposite sides of the magnetosphere into regions called drift shells. Barring perturbations that disturb the adiabatic motion of the particles, a particle on the night-side of the magnetosphere should drift around the Earth and return to the nightside remaining on the same drift shell. In this manner magnetic field lines that penetrate the transition region and even extend out into the magnetosphere have effective communication (by drift shell particles) with the field lines on the dayside. The unsteady state nature of the region external to the nightside plasmapause is carried around to the dayside. The field lines from this region define an area in the Earth's ionosphere called the Auroral Oval (Feldstein, 1969, Akasofu, 1968).

During times of solar activity the solar wind carries disturbances to the magnetosphere. Particularly large magnetospheric disturbances are called magnetospheric storms. Flare-associated energetic particles reaching the Earth's magnetosphere are associated with marked compressions of the magnetic field. These compressions are often followed by successive periods of marked magnetic activity which last for times of one to three hours. These one to three hour events are called substorms.

There are usually several substorms associated with each magnetospheric storm (Akasofu, 1968). As determined by numerous satellite observations there are marked increases in the trapped energetic particle populations ( $E > 1$  Kev) of electrons and protons and a corresponding increase in the auroral activity in the Oval. Large electric fields are induced in the auroral ionosphere causing concentrated currents in the region of the Oval. These currents are called the auroral electrojet. The currents are detected on the ground by the severe fluctuations they cause in the local magnetic field. Ground based magnetometers which monitor the vector components of the local magnetic field record changes of several hundred  $\gamma$  ( $1\gamma = 10^{-5}$  gauss) in the different components of the field. The most intense precipitation and the associated magnetic activity are generally observed in the midnight sector of the Auroral zone. As determined by rocket in-situ observations of electrons and protons, X-ray observations made from high atmosphere balloons, and satellite particle observations, the majority of cosmic radio noise absorption in the ionosphere is contributed by electrons in the 10 Kev energy range. There are significant increases in the trapped electron population for particles in excess of 50 Kev (Lezniak et al. 1968, Lezniak and Winckler, 1970) as well as protons in the 1 to 50 Kev energy range although these particles do not make a major contribution to auroral absorption. It has been suggested by Lezniak and Winckler (1970) that these energetic particles are injected from the tail down into the trapping region near local midnight and then drift from there to other local times.

### I.C. The Trapped Particle Population and the REP.

With this brief introduction we can attempt to place the REP in some context as a substorm-related phenomenon occurring in the morning side ionosphere. The corresponding magnetospheric region would presumably receive excess trapped particles from gradient  $-B$  drifting particle populations injected on the night side near midnight and not directly from the plasma sheet. Little or no magnetic activity suggests there are no local current systems and little, if any, distortion in the local magnetic field. The unusual hardness of the energy spectrum may indicate that the precipitation mechanism for REP's is significantly different from that responsible for nightside precipitation. Looking at Figure 1 of the auroral zone and auroral oval, we see that dayside auroral-zone latitudes actually can be below the auroral oval and are connected therefore to field lines that are closed in the magnetosphere. The REP is reported to extend over a region as great as 1,000 Km (Thorne, 1974) in extent and therefore involves a significant energy source.

The highly unusual nature of a REP in terms of other auroral-zone events makes it a very interesting phenomenon to the auroral and magnetospheric physicist. The possibility that a detailed study of the phenomenon might shed some new light on the entire field of complex ionospheric-magnetospheric interactions is a very appealing one. Ground based measurements such as the VHF forward scatter and riometer only give qualitative indications as to the nature of the precipitating flux while balloon measurements of the Bremstrahlung X-rays can say nothing about the directional distribution of the particle fluxes about the magnetic field. A properly designed in-situ rocket measurement of the actual particle fluxes resolves the question of particle species, energy

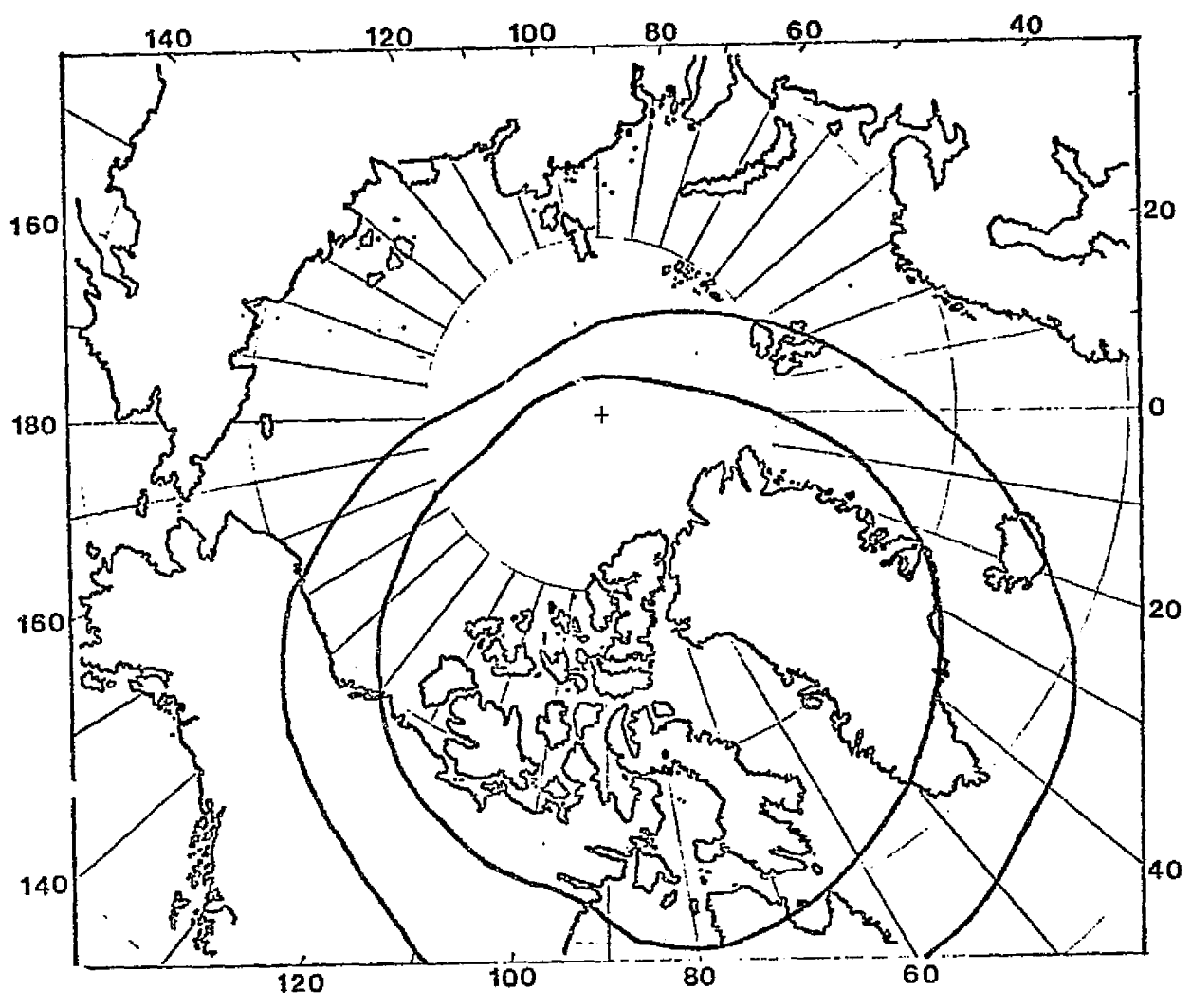


Figure 1. The Auroral Oval

A projection of the auroral oval onto the Earth's surface at about 6:00 UT taken from Akasofu (1968). Northern Scandinavia is in the nighttime auroral oval but may be seen to be well south of it according to this presentation in the morning hours.

① dependence, and pitch angle distributions, and allows for high resolution time analysis. It was hoped that such a rocket-based REP experiment could yield some insight into the complex plasma physical processes which energize the particles that precipitate at various times and places into the upper atmosphere.

I.D. The Organization of This Report.

The following detailed discussion of the REP experiment is divided into four chapters. Chapters 1 and 2 deal with the experimental considerations. Chapter 1 describes the design, construction and calibration of the electron spectrometers while Chapter 2 details the solution of the rocket attitude problem. For those interested principally in the results of the experiments these chapters may be skipped. Chapter 3 describes the data obtained during the REP of May 31, 1972, and the reduction of that data. In Chapter 4 we discuss these experimental results in the light of present magnetospheric theories.



## CHAPTER II

### THE DESIGN AND CALIBRATION OF A NINE CHANNEL ELECTRON ENERGY SPECTROMETER

#### II.A. Choosing An Electron Detector

##### 1. Criteria For Counting Capability

Bailey (1968) wrote an extensive review of the REP based upon three years (1964-1966) of ground based observations in Alaska using the riometer and forward scatter experiments. Bailey's results provided a major source of particle flux data used in establishing design criteria for our in-situ REP experiment. In view of this we will discuss this data before discussing the design of the spectrometer.

The differential absorption of cosmic radio noise at a given height in the ionosphere is a function of the local ionization and the local collision rate between electrons and neutral particles (Sen and Wyller, 1960). Even if one assumes a fixed collision rate height profile, various ionization height profiles may produce the same total absorption (at a single frequency) observed on the ground. By adding the forward scatter data to the riometer data the ambiguity may be removed provided the scattering height is well known. Bailey could not fix the scattering height, but by assuming various heights he could produce a range of flux and hardness parameters for the REP's that he observed. The flux of precipitating particles was assumed to be isotropic over the downward hemisphere with a unidirectional integral flux of the form

$$J(>E) = J_0 e^{-E/E_0} \quad 2.1$$

with  $J$  being the number of particles per  $\text{cm}^2$  per sec. per ster. above  $E$  (in Kev) and  $E_0$  (called the e-folding energy in  $\text{EeV}$ ) being the spectral hardness parameter. In a very crude sense,  $E_0$  controls the amount of ionization produced in the ionosphere and  $J_0$  controls the depth of ionization production.

As an example of Bailey's results we consider the REP of November 13, 1965. Choosing a scattering height of 70 km for the forward scatter produced a spectra with  $E_0 = 68$  Kev and  $J_0 = 7.6 \times 10^5 / (\text{cm}^2 \times \text{sec.} \times \text{ster.})$ , while choosing a scattering height of 75 Km produced a spectrum with  $E_0 = 34$  Kev and  $J_0 = 4.8 \times 10^6 / (\text{cm}^2 \text{ sec ster.})$ . To appreciate the difficulty this presented us with when designing the spectrometer, let us look at the flux at several energies. For the softer of the two spectra the flux at 30 Kev is four times the flux at 30 Kev for the harder spectrum. At 400 Kev however, the flux of the harder spectrum is some 56 times the flux of the softer spectrum. All of the REP's analyzed by the forward scatter-riometer technique same wide range of possible flux values. We were therefore forced to design with the widest possible dynamic range in mind. The major consideration for our device was its ability to cope with as large a range of hardness and flux parameters as possible.

## 2. The Advantages Of Solid State Detectors

Charged particle detection on a sounding rocket calls for comparatively small detection devices with high reliability. The semiconductor type particle detector was the natural choice in the 50 Kev to several Mev range. Such detectors can be small and have straight forward geometry, while energy resolution in this range tends to be

limited more by space available for associated electronics and telemetry information rate, than by the device itself. We wished to be able to detect electrons with energies less than about 2 Mev and greater than some 50 Kev and in addition had to be prepared for a wide dynamic range of particle fluxes.

The semi-conductor detector is essentially a slab of silicon (or germanium) in which a charged particle stops through ionizing interactions resulting in the production of mobile charge carriers in the conduction band of the silicon. These charges are then collected by an electric field which is maintained across the detector. Superficially this is very much the same behavior as a gas proportional counter. The theory of operation is fairly well developed and the literature is extensive. (see Taylor, 1963 or Dearnaley and Northrop, 1966). We will treat the basic operation of the detector only very briefly.

Several different types of semi-conductor detectors are made. Our choice of a lithium compensated (P.I.N.) detector was dictated by the comparatively large depth of silicon necessary to stop 2 Mev electrons and because of the need of an energy threshold below 50 Kev.

The average integrated path length of an electron coming to rest in a material may be determined by use of the Bethe stopping power formula. (Bethe, 1938).

$$-\frac{dE}{dX} = \frac{4\pi e^4 ZN}{mv^2} B \quad (2.2)$$

with B given by

$$B = \frac{1}{2} \ln \frac{mv^2 E}{2I^2(1-B^2)} - \frac{1}{2} \ln 2 (2\sqrt{1-B^2} - 1 + B^2) + 1 - B^2 \quad (2.3)$$

This formula is good for energies below 10 Mev where ionization is the principal energy loss mechanism.  $Z$  is the atomic number of the absorber,  $N$  the number of absorber atoms per  $\text{cm}^3$ ,  $m$  the mass of the electron and  $I$  the mean ionization potential of the absorber. This formula yields a path length which is about 40% greater than the average depth of penetration because of the considerable large-angle scattering. Using the appropriate values for silicon it is easily determined that somewhat over two mm are required to stop one-Mev electrons.

### 3. Some Properties of Silicon Detectors

In barrier layer detectors of the diffused junction and surface barrier type the depletion region is obtained by applying a large voltage. The larger the voltage the deeper the depletion region will be. The highest resistivity silicon (i.e. the purest and most expensive) will tolerate fields of a thousand volts/mm at best before breaking down completely. Depletion depths of a few millimeters have been achieved but at the expense of large leakage currents because of the large reverse bias required. A far more inexpensive device which operates at much lower voltages is the lithium compensated silicon detector. The lower voltages mean less leakage current and therefore less noise.

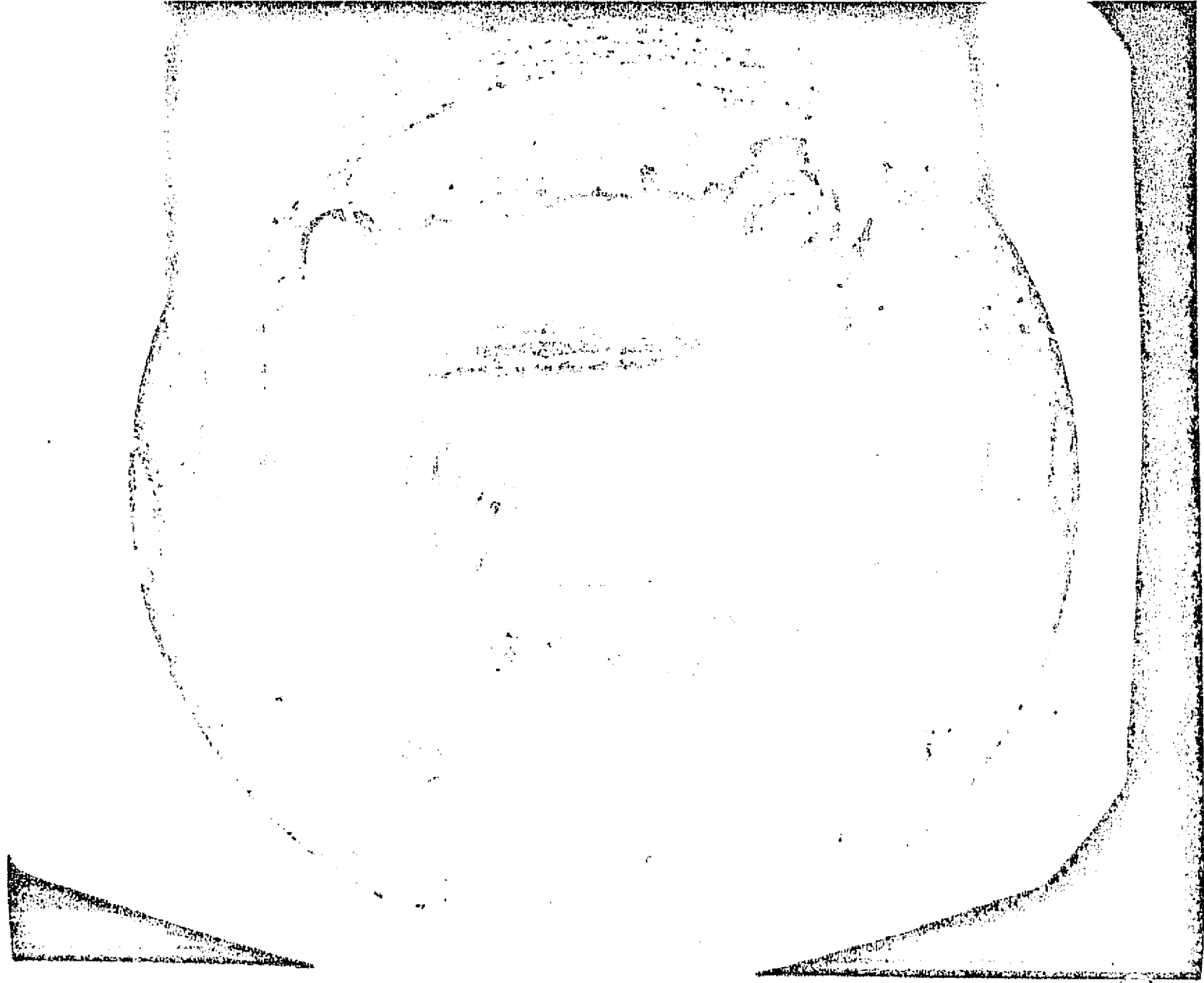
P.I.N. is an abbreviation for p-type-intrinsic-N-type semiconductor detector and describes the physical arrangement of the three basic regions in the lithium compensated silicon detector. A slab of p-type silicon crystal is painted on one surface with an oil suspension of lithium. The lithium is then diffused under high temperature into the crystal. The lithium, a donor impurity, greatly overcompensates the p-type acceptors at one surface of the crystal and results in the form-

ation of an N-P junction at about 300 microns in the crystal.

Temporary electrodes are plated to the crystal surfaces and a reverse bias is then applied across the junction (~ 300 volts). The lithium drifts all the way across the silicon creating a large region of silicon with almost the properties of pure and undoped silicon. The crystal now has an n-type region some 200 to 300 microns deep and an effective intrinsic region with no majority carriers the rest of the way across. The surfaces are etched down and a surface junction is obtained on the intrinsic surface by the application of a thin layer of gold.

(30  $\mu\text{g}/\text{cm}^2$ ). This surface is the entrance surface for charged particles and constitutes a small dead layer. Our detectors had about 160 Å (31  $\mu\text{g}/\text{cm}^2$ ) dead layer of gold. The other surface after etching is coated with aluminum. The intrinsic region (in our detectors about 3 mm thick) is the active part of the detector. In Figure 2.1 we show the detector in its mounting.

150



ORIGINAL PAGE IS  
OF POOR QUALITY



## II.B. The Collimator

The solid state detector was enclosed in a brass and lead collimator. The collimator geometry was determined by considering the possible intensities of electron precipitation that might occur during REP's as well as the angular resolution set by the telemetry and rocket spin.

### 1. Geometrical Factor

The differential flux of particles in a given direction,  $\vec{F}(\hat{u}, \vec{x}, E)$ , sometimes called the unidirectional flux or directional intensity, is usually expressed in units of  $\text{cm}^{-2} \text{ster}^{-2} \text{Kev}^{-1} \text{sec}^{-1}$ .  $\vec{x}$  is a position vector in space,  $\hat{u}$  is the unit vector in the direction of the particle motion,  $E$  is the particle energy, and  $\vec{F}(\hat{u}, \vec{x}, E)$  points along  $\hat{u}$ . The counting rate  $N$ , in units of  $\text{sec}^{-1}$ , of a collimator-detector combination is a function of the geometry of the unit and the efficiency of the detector. For the collimator-detector geometry shown in Figure 2.2,  $N$  is given by

$$N = \int_{t_1}^{t_2} \int_E \int_{S_1} \int_{S_2} \frac{(\vec{F} \cdot d\vec{\sigma}_1)(\hat{u} \cdot d\vec{\sigma}_2) E(E)}{DtD^2} dEdt \quad (2.4)$$

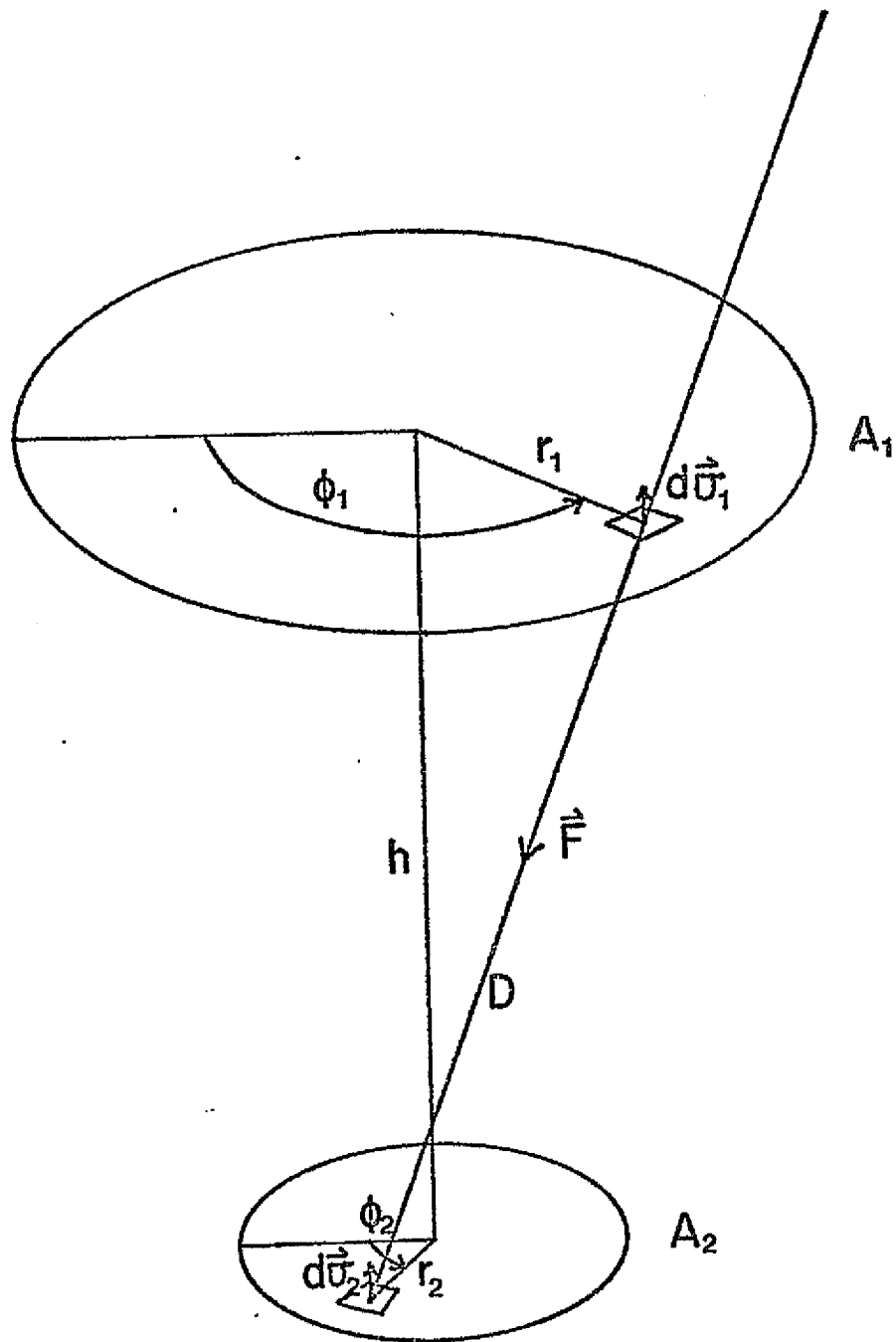


Figure 2.2. Schematic collimator-detector geometry.

where the geometrical terms are defined in Figure 2.2  $E(E)$  is the detector efficiency, which we will treat fully in section II.D.  $Dt$  is the counting interval. Since the collimator does not distinguish between directions in the field of view we must assume some average flux over the aperture. Letting

$$F(E) = \left\langle |\vec{F}(\hat{u}, \vec{x}, E)| \right\rangle_{\vec{x}, \hat{u}, t}$$

we may write equation (2.4)

$$N = G \int_E F(E) E(E) dE$$

where  $G$ , called the geometrical factor, is strictly a function of the collimator-detector geometry. Using polar coordinates  $r_1, \phi_1$  and  $r_2, \phi_2$  in the planes of  $A_1$  and  $A_2$  (see Figure 2.2) separated by distance  $h$  we find that  $G$  may be expressed as

$$G = \int_0^{2\pi} \int_0^{2\pi} \int_0^{R_1} \int_0^{R_2} \frac{\cos^2 \alpha r_1 r_2}{D^2} dr_1 dr_2 d\phi_1 d\phi_2$$

with  $D^2 = r_1^2 + r_2^2 - 2r_1 r_2 \cos(\phi_1 - \phi_2) + h^2$  and  $\cos \alpha = \frac{h}{D}$ . Substituting in these values and performing the integration yields

$$G = \frac{\pi^2}{2} \left\{ R_1^2 + R_2^2 + h^2 - \sqrt{(R_1^2 + R_2^2 + h^2)^2 - 4R_1^2 R_2^2} \right\} \quad (2.5)$$

Since it is very difficult to produce an isotropic flux of energetic electrons in the laboratory, only indirect means of checking

the geometrical factor may be reasonably used. This point is discussed fully in section II.D.

The value that one chooses for the geometrical factor is determined by the expected flux levels, accumulation time interval, the width of the energy channels of the energy analyzer and the capacity of the data accumulators. Following Bailey (1968) we modeled the expected differential energy spectra in the form

$$F = \frac{J_0}{E_0} \exp(-E/E_0) \quad (2.6)$$

with  $E_0$  varying from 25 Kev to 150 Kev and  $J_0$  varying from  $10^9$  to  $10^6$  ( $\text{cm}^{-2} \text{sec}^{-1} \text{ster}^{-1}$ ). Obviously one cannot adequately cover all these possibilities with a single device and achieve optimum performance for all possibilities. We designed for optimum conditions toward the center of the ranges and attempted to extend our limit as far as possible in both directions on hardness and flux levels. The hardest spectrum here yields about  $15/(\text{cm}^2 \times \text{sec} \times \text{ster} \times \text{Kev})$  at 1.0 Mev while the softest spectrum gives essentially nothing at 1.0 Mev. We planned for an integral channel as the highest energy channel. Above 1 Mev the integral flux for the hardest spectrum is of the order of  $1,300/(\text{cm}^2 \times \text{sec} \times \text{ster})$ . For the other energy extreme we consider the flux at 50 Kev which gives the values  $5.5 \times 10^6$  and  $7.8 \times 10^5/(\text{cm}^2 \text{sec ster})$ . At 400 Kev we have  $4.5$  and  $4.6 \times 10^2$ . The data accumulation time was .00853 seconds as set by telemetry requirements. We chose to set the widths of the energy channels at approximately logarithmically increasing values to insure complete coverage of the energy range by our nine channel analyzer. The geometrical factor was designed basically to keep the largest expected

TABLE 2. 1- Model Count Rates with  $F = \frac{J}{E_0} \exp(-E/E_0)$

Sample energy interval (kev)	Max. counts per channel	$J = 1.6 \times 10^8$ $E_0 = 50$ kev	$J = 1.4 \times 10^8$ $E_0 = 75$ kev	$J = 1.0 \times 10^8$ $E_0 = 100$ kev	$J = 7.0 \times 10^7$ $E_0 = 150$ kev
40-60	1023	1011	820	518	286
60-90	1023	928	885	607	362
90-150	1023	789	991	783	540
150-220	511	256	491	479	410
220-340	511	76	253	330	379
340-600	255	8	62	131	255
600-1000	255	1	2	10	51
1000-1800	255	1	1	1	4
1800- $\infty$	255	1	1	1	1

flux in the lowest channel within the counting capability of the accumulators. The three lowest channels had 10 bit accumulators with a maximum count rate then of 1023 counts per accumulation period. The next two accumulators had nine bits and the remaining four had eight bits. Table 2.1 demonstrates count rates for a set of hypothetical energy intervals and model spectra using a geometrical factor of  $.005 \text{ cm}^2 \times \text{ster}$ . As can be seen, considerable latitude was available. This is particularly true for the higher energy channels in which we provided a much higher count rate capability than would be necessary for a pure exponential spectrum.

It can be seen from equation 2.5 that with the geometrical factor chosen, there are still two free parameters, which may be varied to determine the angular width of the collimator acceptance cone. It was anticipated that the rocket would have a roll rate of 5 roll/sec. or an angular rate of about 15 degrees per accumulation interval. 15 degrees then became a reasonable angular width for the collimator. This width is indicated by the angle  $\gamma$  in Figure 2.3. The remaining free parameter was adjusted to set the length of the collimator within the constraints of space in the rocket. Table 2.2 lists all the relevant dimensions of the collimator.

Table 2.2

Collimator Dimensions

$$R_1 = .325 \pm .0025 \text{ cm}$$

$$R_2 = .170 \pm .0025 \text{ cm}$$

$$h = 2.467 \pm .0127 \text{ cm}$$

$$\gamma = 15.0 \pm .3 \text{ degrees}$$

$$G = .0048 \pm .0003 \text{ cm}^2 \text{ ster}$$

## 2. Design of the Shielding

There are several other important design considerations for the collimator. Particles on the edge of the acceptance cone will scatter when hitting the collimator surfaces. These particles will have distorted energy spectra, as well as being outside the defined field of view. They will therefore introduce errors if they reach the detector and are counted. Particles stopping in the collimator wall will also produce Bremsstrahlung x-rays. While the walls may be sufficiently thick to stop 3 or 4 Mev electrons they may not be thick enough to prevent significant x-ray count rates in the 3mm thick silicon detector.

The scattering of electrons off the walls of the interior of the collimator cannot be prevented. One attempts to reduce the problem by: (1) reducing the surfaces in direct line of sight of the detector surface and the entrance aperture, (2) providing scattering volumes in which scattered particles may be reduced in energy and absorbed, and (3) orienting surfaces so that scattering particles are diverted toward the scattering volumes and away from the detector. In Figure 2.3 we show a diagram of the collimator in cross-section. The only surfaces in direct view of the detector surface and the entrance aperture are the sharp edges of the collimator baffles. These edges defined the acceptance cone and the geometrical factor. The acceptance cone was checked directly with energetic electrons. We will discuss this fully in section II.D.

Again using the Bethe formula (eq. 2.3) we determined that 2.24 mm of brass was the average range of 3 Mev electrons. Adding 40% for straggling and insurance we decided that 3.2 mm of brass was sufficient for the outer layer of the collimator. This was then backed with 3.9 mm

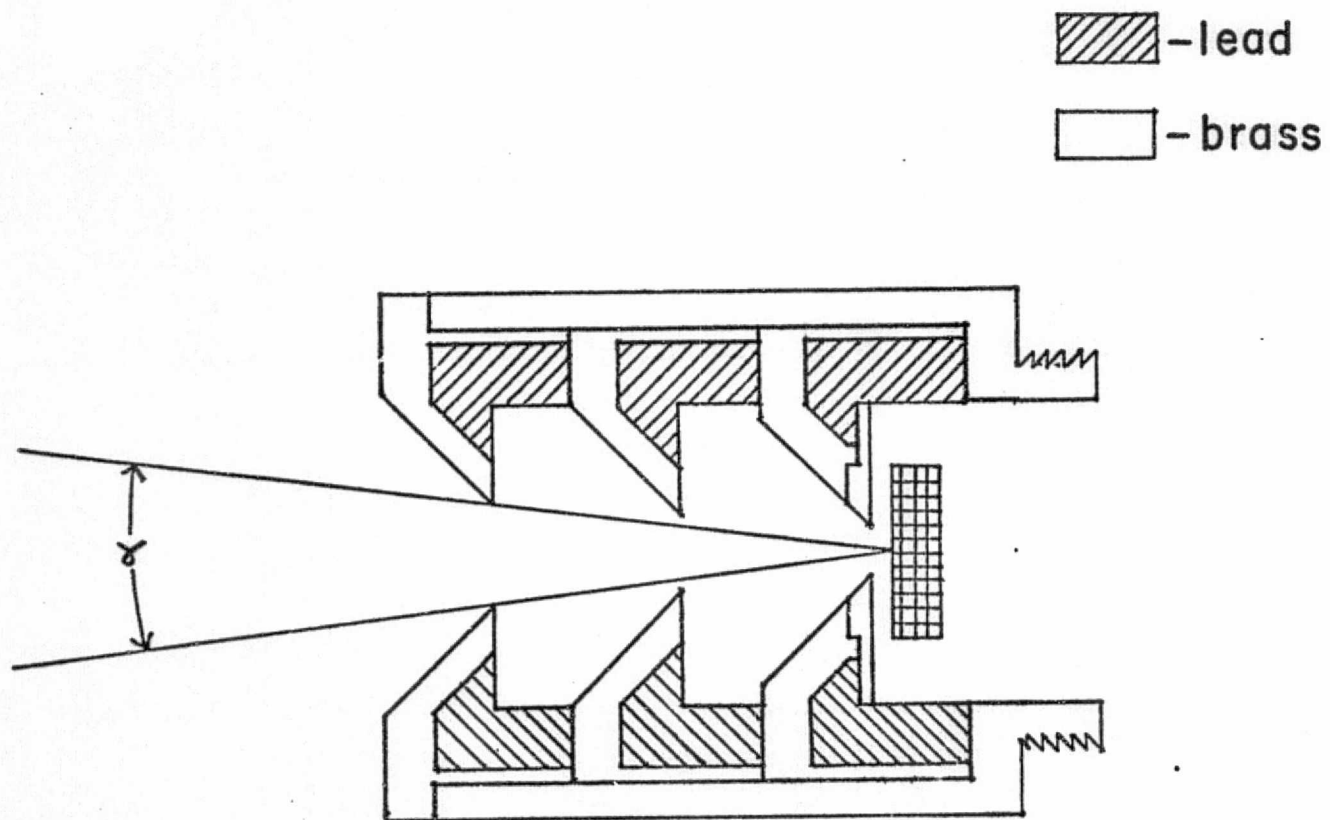


Figure 2.3. Cross-section of the cylindrical brass collimator showing the lead inserts and the position of the solid-state detector.



of lead to attenuate the x-rays. It is important to note that the bremsstrahlung production cross-section in lead is about three times greater than in brass so that one prefers if possible to stop all the electrons in the brass. Direct line of sight between the lead and the detector was avoided to exclude x-rays produced by scattered electrons hitting the lead.

The weight and size of the collimator were very important since it had to be carried on a rocket. We were forced therefore to keep the lead shielding to a bare minimum. We modeled the x-ray production in an attempt to determine this minimum shielding. We chose a very simple geometry for the task. A unidirectional flux of electrons of differential spectra of the form of eq. 2.1 was assumed normally incident on a plane target of brass and lead. A 3 mm thick silicon detector was assumed placed behind the target and the energy spectrum detected in the silicon was determined. This was then compared with the spectrum of the incident electrons. The calculation is described in detail in Appendix A-1. The results from the calculations for no lead are compared with the calculations for .39 cm lead in Figure 2.4.

We have assumed that for the x-rays the detector had an effective geometrical factor of  $2\pi \text{cm}^2 \text{ster}$ , where A is the area of the detector. It can be seen from Figure 2.4 that 3.9 mm of lead provided sufficient shielding for the case of a relatively hard spectrum. We used 3.9 mm of lead in the actual collimator and as will be seen later the spectrum encountered during the rocket flight was softer than this example. In section II.D we will compare these results with those obtained on the Goddard Space Flight Center Van de Graaff accelerator.

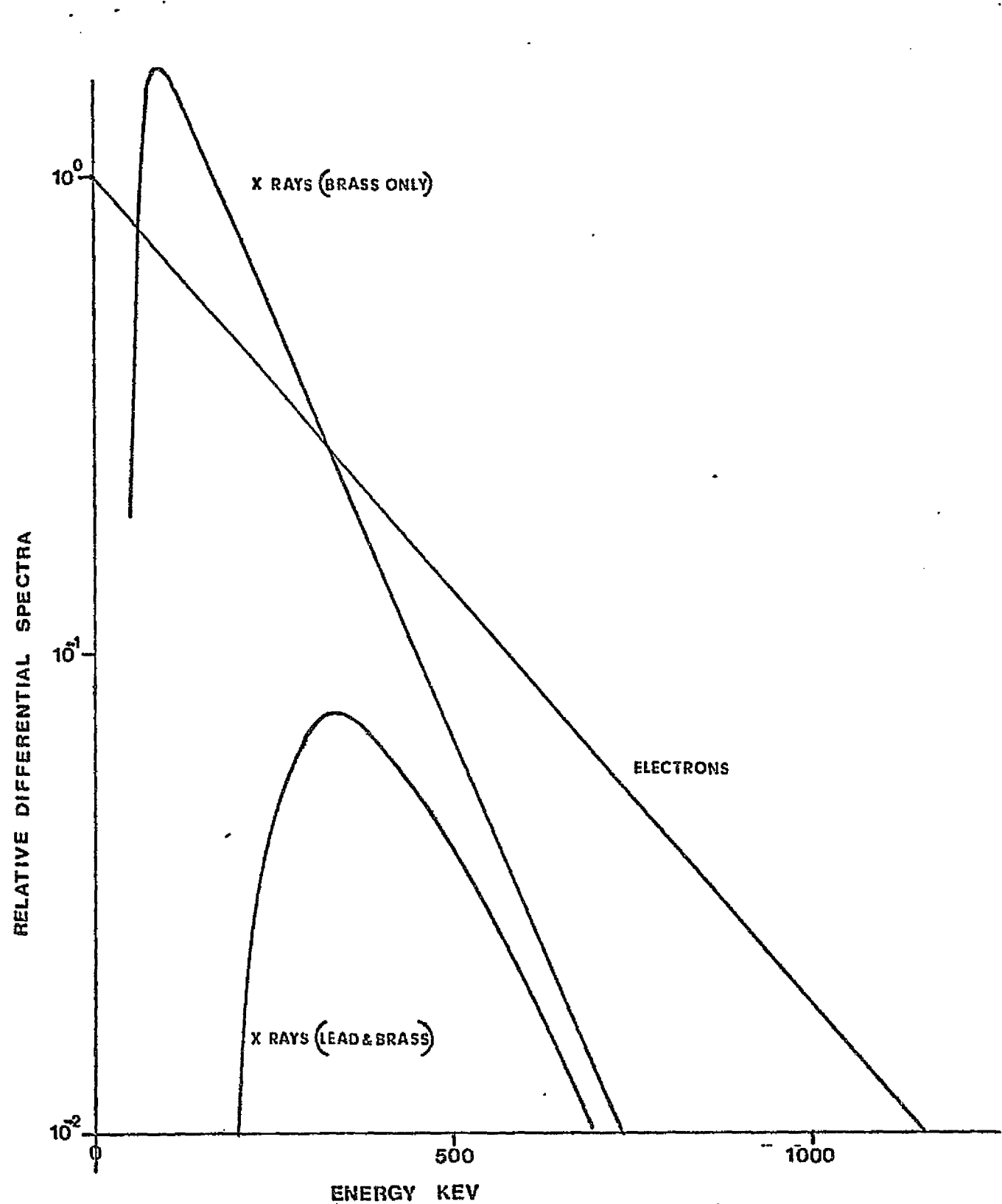


Figure 2.4 . The predicted x-ray spectrum as seen by the 3 mm. thick silicon detector with and without lead shielding.

### 3. The Aluminum Light Shield

Since silicon detectors are highly light sensitive a light shield was included in the collimator to front the detector. We chose aluminum because of its high reflectance and opacity even into the ultra violet. Table 2.3 lists transmission coefficients for aluminum at several wavelengths.

The aluminum foils for the windows were prepared by flash vacuum plating onto small glass slides that were dipped in a twenty per cent solution of polyvinyl pyrrolidone in ethyl alcohol. The thickness of the aluminum was determined with an interferometer. Each slide was examined for pin holes under an intense light. The regions with no pin holes were determined and etched around with a stylus. These regions were then floated off the slides by using distilled water to dissolve the polyvinyl pyrrolidone. The aperture of the collimator was placed under the foils and the distilled water allowed to evaporate. The surfaced adhesion of the aluminum to brass was sufficiently strong to withstand the 34 g accelerations of the Nike-Tomahawk shake test, so no additional adhesive was required.

TABLE 2.3 - Transmission and Reflectance of Aluminum Films at various wavelengths. (taken from Hass and Waylonis, 1961)

Film Thickness	Wavelengths									
	2200 A		3000 A		4000 A		5460 A		6500 A	
	R%	T%	R%	T%	R%	T%	R%	T%	R%	T%
3200 A	88.5	3.2	90.0	1.8	91.1	1.1	90.4	0.5	89.6	0.4
4000 A	90.6	1.1	91.4	0.5	92.1	0.4	91.2	0.2	90.3	0.2
5000 A	91.5	0.3	92.0	0.1	92.5	<.1	91.5	<.1	90.6	<.1

### II.C. Effects Of The Light Shield On Energy Resolution

10,000 Å of aluminum is a dead layer of  $270 \mu\text{gm}/\text{cm}^2$ . Figure 2.5 gives the energy loss of various energy electrons in this thickness of aluminum. A 30 Kev electron loses about 2 Kev. The energy loss becomes even less as the energy of the electrons is increased, so that for the largest portion of the energy region of interest, the foil causes little distortion in the average energy. There are other possible distortions that should be considered as a slight digression into the energy loss process will reveal.

As an electron traverses a material like aluminum it loses energy by numerous ionizing (i.e. inelastic) collisions with atomic electrons. The vast majority of these involve almost no angular deflections (Bethe 1936, Landau 1946). In addition the electron undergoes elastic collisions with the screened nuclei of atoms in which it may suffer sizeable angular deflections. Radiative energy loss due to production of bremsstrahlung is unimportant in both collisional processes for primary electron energies below 10 Mev. (At a primary electron energy of 1.5 Mev the ratio of collisional to radiative energy loss in aluminum is  $6.9 \times 10^3$  (Berger and Seltzer, 1964)). Since the energy loss and the angular scattering are essentially stochastic processes, the electrons emerge from a thin foil with a distribution of energies and directions. The propensity of electrons to lose a varying amount of energy over any short distance is usually referred to as energy straggling and it is well described by the Landau distribution. (Dearnaley and Northrop, 1966). We see then that unidirectional monoenergetic incident particles emerge from a thin foil with a distribution in both energy and direction. Some particles are scattered back in the initial direction and lost completely.

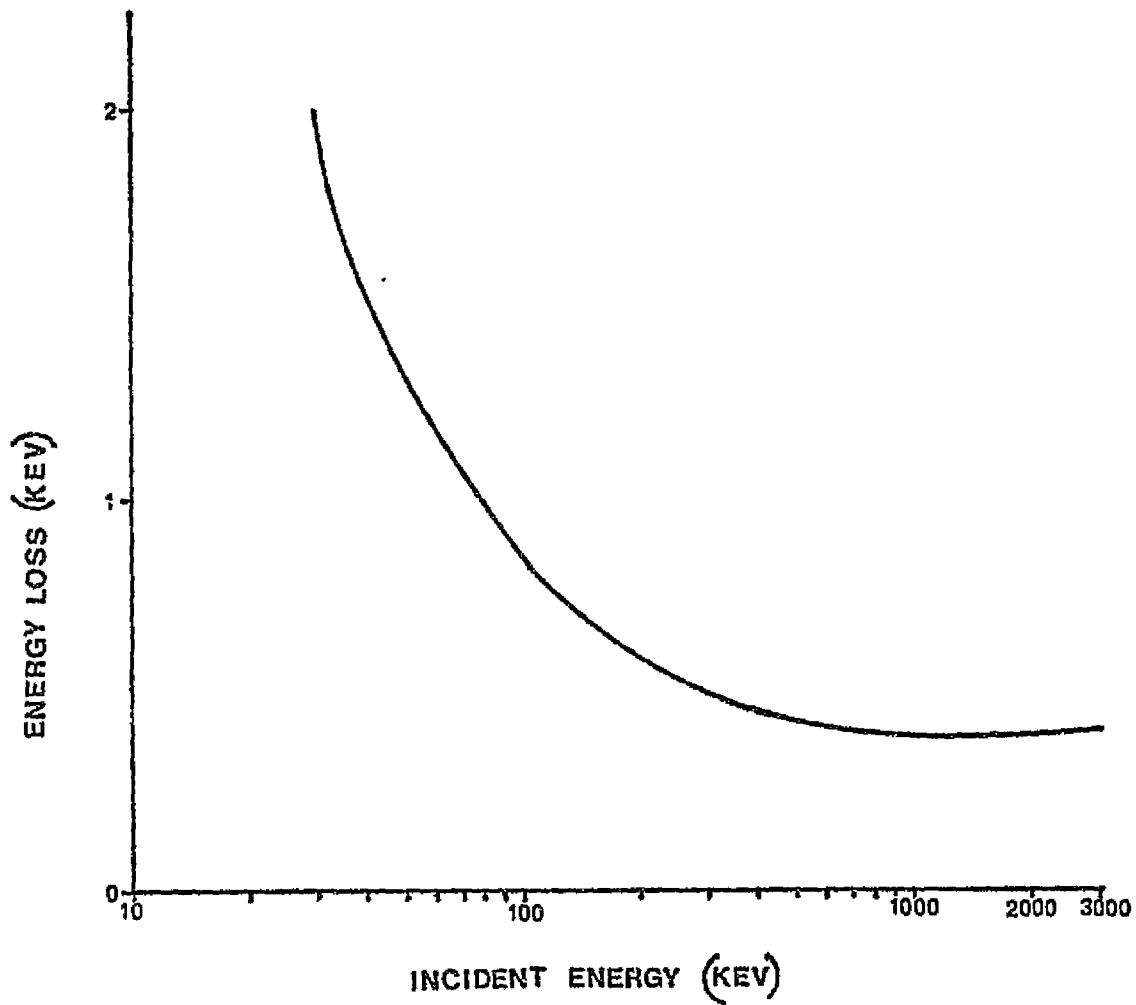


Figure 2.5. Energy loss of electrons in  $270 \mu\text{g}/\text{cm}^2$  of aluminum.

We are therefore required to examine the transmission probability as well as angular and energy distributions.

Experimental and theoretical data does exist over the energy range of interest although the coverage is not very complete. The data that does exist indicates that extrapolation to energies not specifically covered can be done with a fairly high degree of confidence.

Kanter (1961) has determined the transmission coefficient,  $\eta_T$ , for electrons in the energy range 1 to 10 Kev through various thickness of aluminum foil. The beams as a function of reduced energy,  $\bar{E}$ , were normally incident and the transmitted particles were measured over  $2\pi$  steradians. The transmission coefficient may be expressed as

$$\eta_T = \frac{\text{transmitted particles over } 2\pi \text{ steradian}}{\text{incident number of particles}} \quad (2.7)$$

The coefficient is normally scaled in terms of the reduced energy  $\bar{E}$  which is given by the relation  $\bar{E} = E/E_r$  with  $E$  as the energy of the incident electrons and  $E_r$  as the penetration energy of the foil as defined in appendix A-2. Figure 2.6a is a slightly modified version of Kanter's results for aluminum. It has been modified for easier comparison with Figure 2.6b which is for the energy range 500 Kev to 5 Mev determined from the results of Berger and Seltzer (1968). The agreement is quite good even though the energy ranges are very different. In Figure 2.6c is a curve determined from the empirical formula of Kobetich and Katz (1968). The empirical formula is very simple to use since it can yield values at all energy without scaling from a graph. For this reason we used Kobetich and Katz's results. For 40 Kev electrons,  $\bar{E}$  is about 4 for a 10,000 Å aluminum foil. It is evident that from

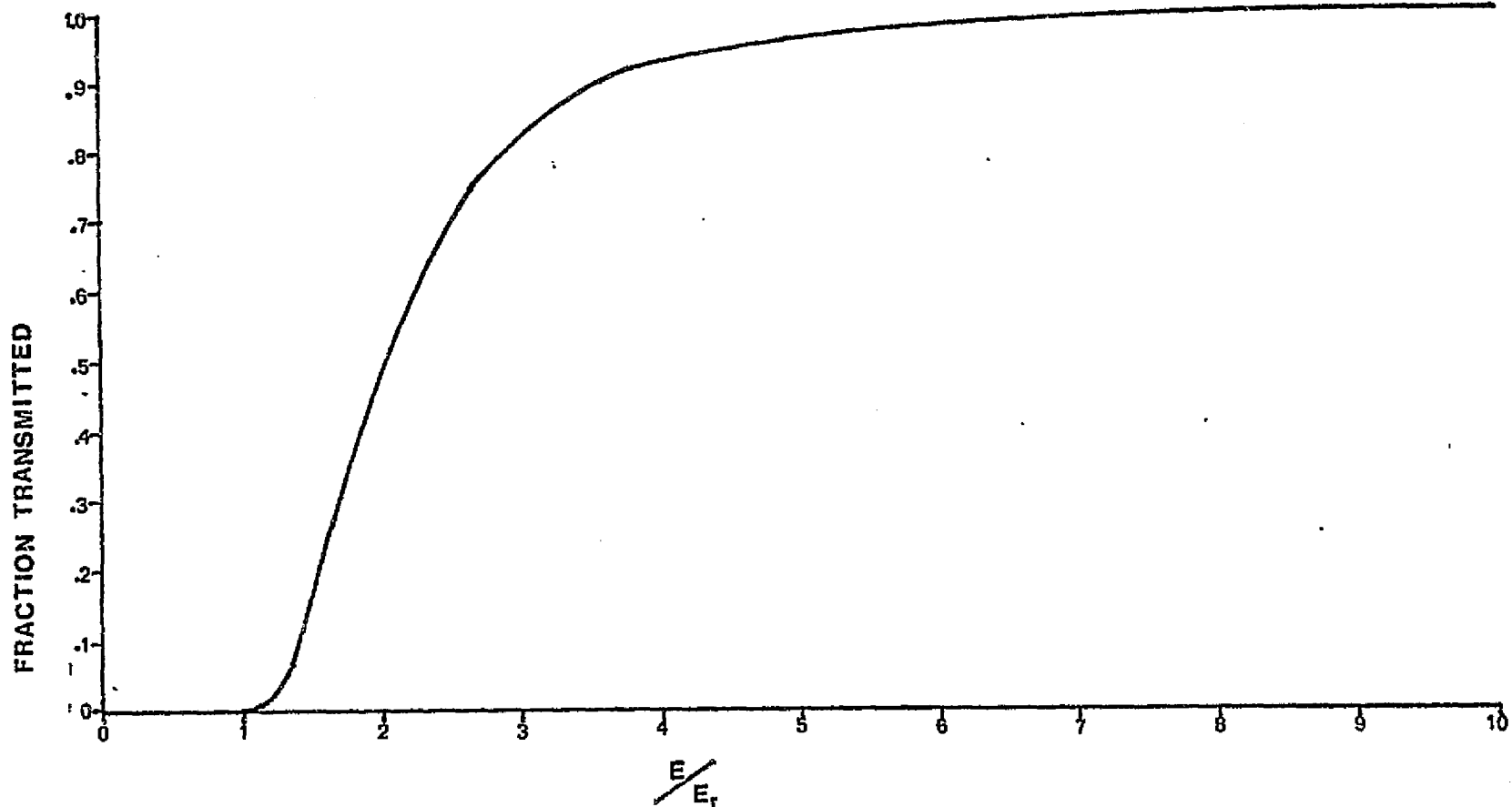


Figure 2.6a. Fraction of electrons transmitted through thin foils as a function of reduced energy .[ 1 to 10 kev determined experimentally, Kanter (1961)]



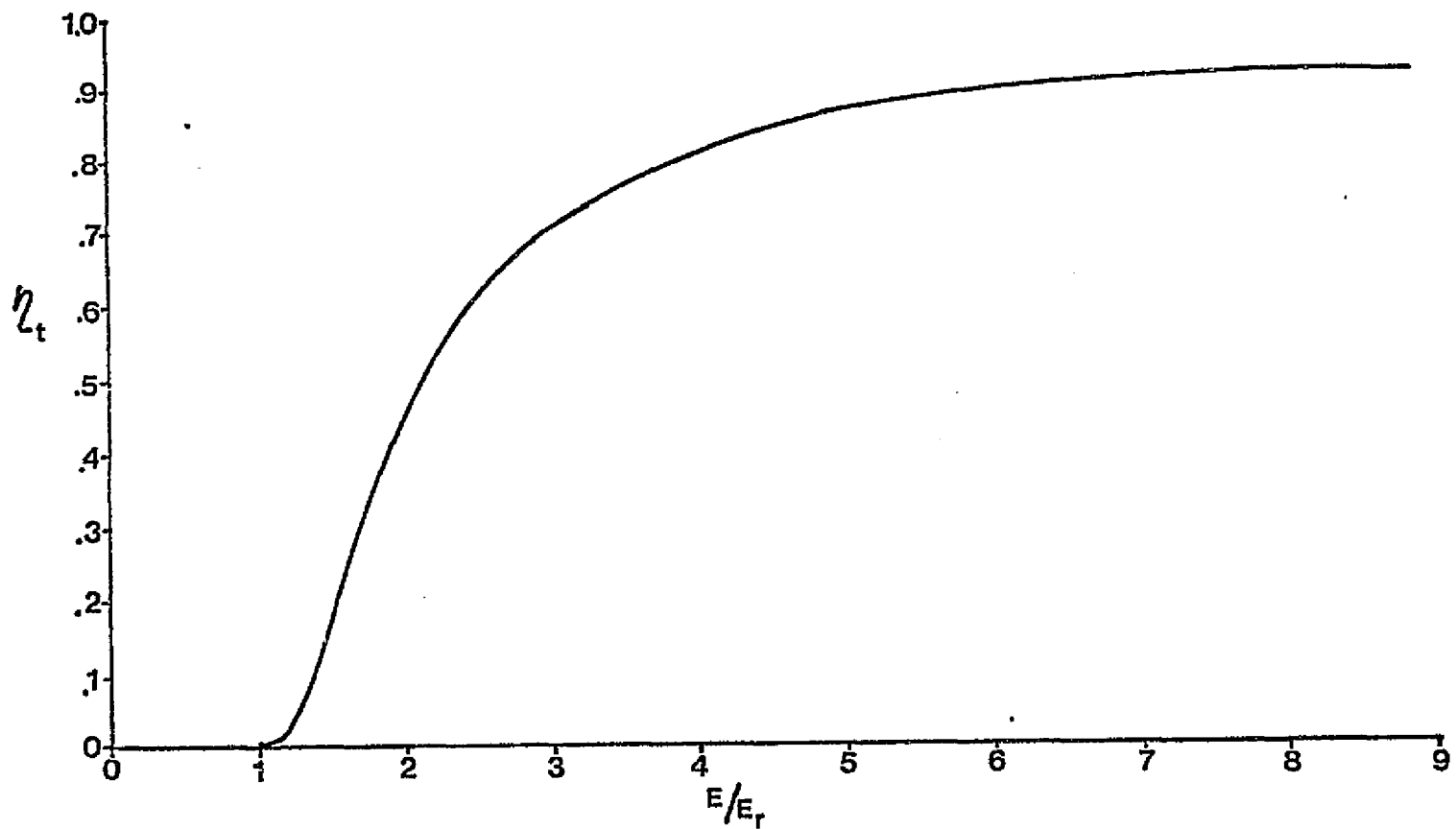


Figure 2.6b. Fraction,  $\eta_t$ , of electrons transmitted through thin foils as a function of reduced energy. [500 to 5,000 kev determined theoretically, Berger and seltzer (1969)]

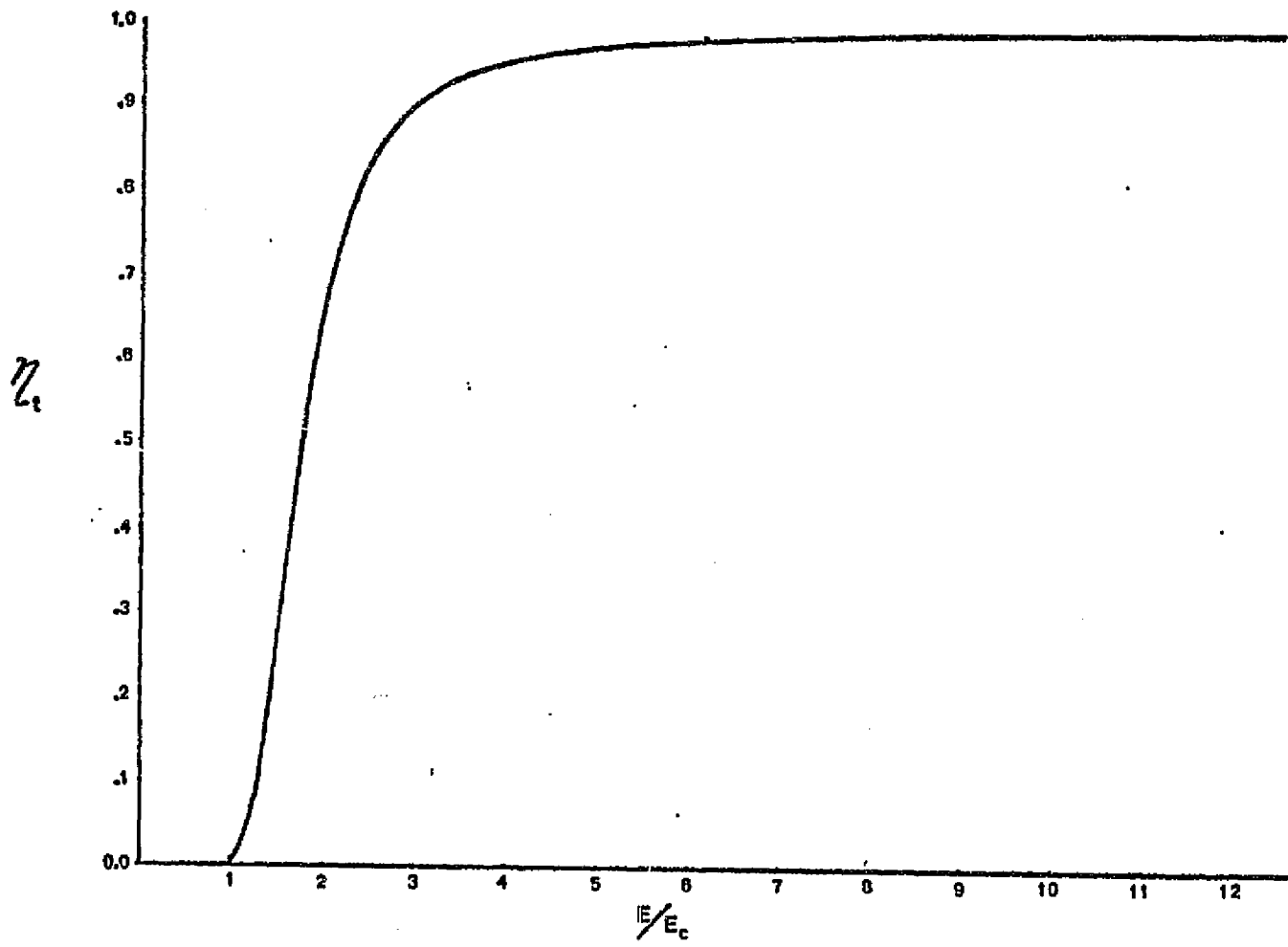


Figure 2.6c. Fraction,  $\eta_t$ , of electrons transmitted through thin foils as a function of reduced energy. [From empirical formula of Kobetich and Katz (1968)]

Figure 2.6c that the correction is quite insignificant over most of the energy range of interest.

Figure 2.7 shows energy spectra of transmitted particles for incident beams of monoenergetic particles scaled at two values of  $E$  again taken from Berger and Seltzer (1968). Interpolating we can determine that for an incident energy of 40 Kev the resolution (Full-Width-Half-Max) is of the order of 3.5 Kev. This resolution obviously improves with increasing energy. As we will see this is small compared to the detector-amplifier energy width.

The final problem associated with the foil is the angular scattering and like the other problems is most pronounced at lower energy. Figure 2.8 shows a plot from Kanter (1961) of the most probably scattering angle as a function of the reduced energy,  $E$ . For  $E = 4$  (about 40 Kev) the most probably scattering angle is less than fifteen degrees from the normal, but some 5% of the particles have scattering angles greater than 50 degrees. As the solid state detectors have a significantly larger dead-layer off to one side (see Fig. 2.1) something on the order of 2% of the lowest energy counts may be lost.

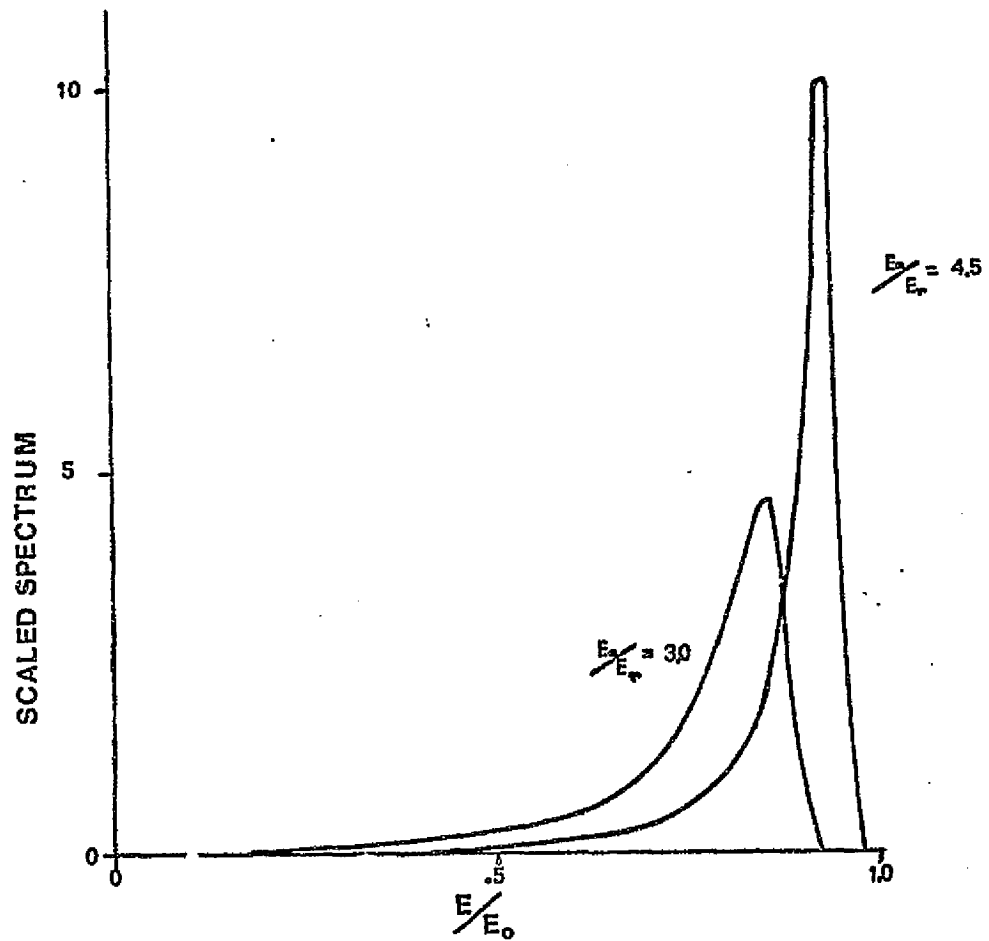


Figure 2.7. The energy spectra of transmitted electrons according to Berger and Seltzer (1968)

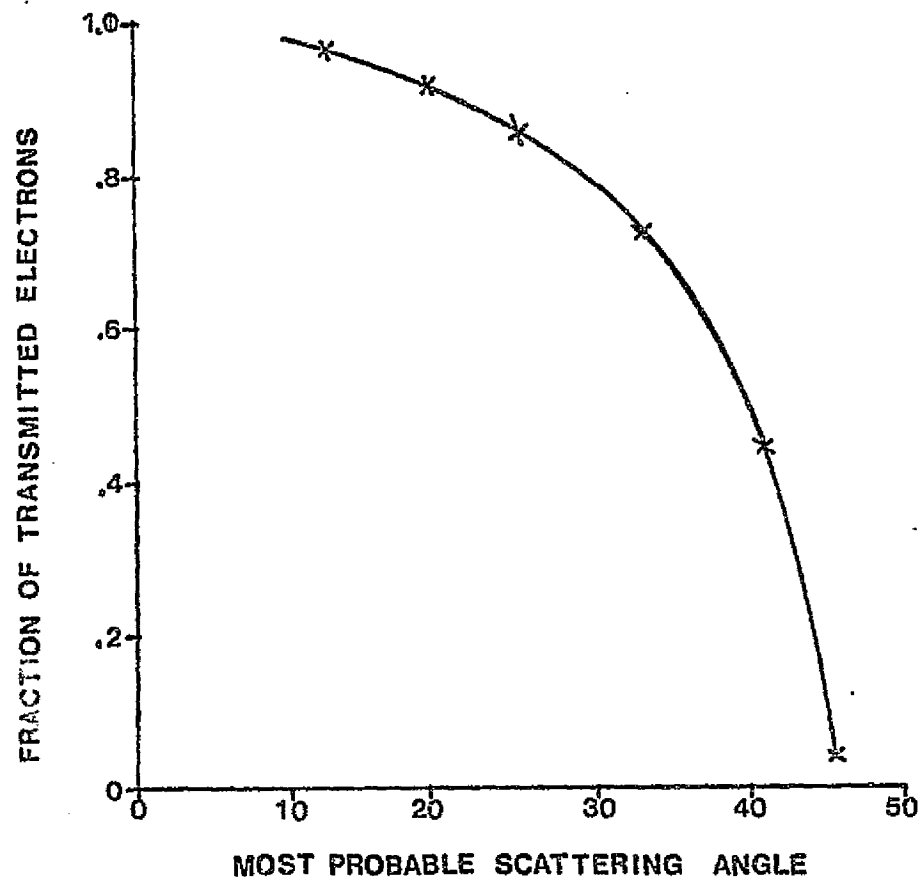


Figure 2.8. The most probable scattering angle of normally incident electrons transmitted through thin foils taken from Kanter (1961).

#### II.D. Modeling The Spectrometer Response Functions

For energies below 10 Mev electrons lose energy mainly in ionizing collisions with atomic electrons. Secondary and tertiary particles are produced with most having kinetic energies smaller than the average ionization potential of the absorber atoms. (Dearnaley and Northrop, 1966). The cascading particles continue the process of impact ionization until their kinetic energies are all below  $E_g$ , the energy necessary to raise one electron out of the valence band of the silicon into the conduction band. (Taylor, 1963). There are several processes other than production of conduction electrons and holes which act as final repositories for energy so that on the average the final energy to charge pair ratio is slightly higher than  $E_g$ .  $E_g$  for silicon is 1.08 ev per electron-hole pair (Dearnaley and Northrop, 1966) while the measured mean energy per electron-hole pair produced by ionizing radiation is  $W = 3.6$  ev. Neglecting any charge loss processes we would expect

$$Q = Ee/W \quad (2.8)$$

to be collected on the electrodes.  $E$  is the energy of the incident particle and  $e$  is the electron charge. For a 100 Kev electron stopping in silicon this formula yields  $5.3 \times 10^{-15}$  coulombs. This means we require a very sensitive charge integrating preamplifier as the first stage of an amplification system.

As we have indicated the average energy loss per path length for electrons stopping in different materials varies inversely with energy below an Mev. This means that energy deposition or ionization is an increasing function as an electron penetrates into a silicon detector.

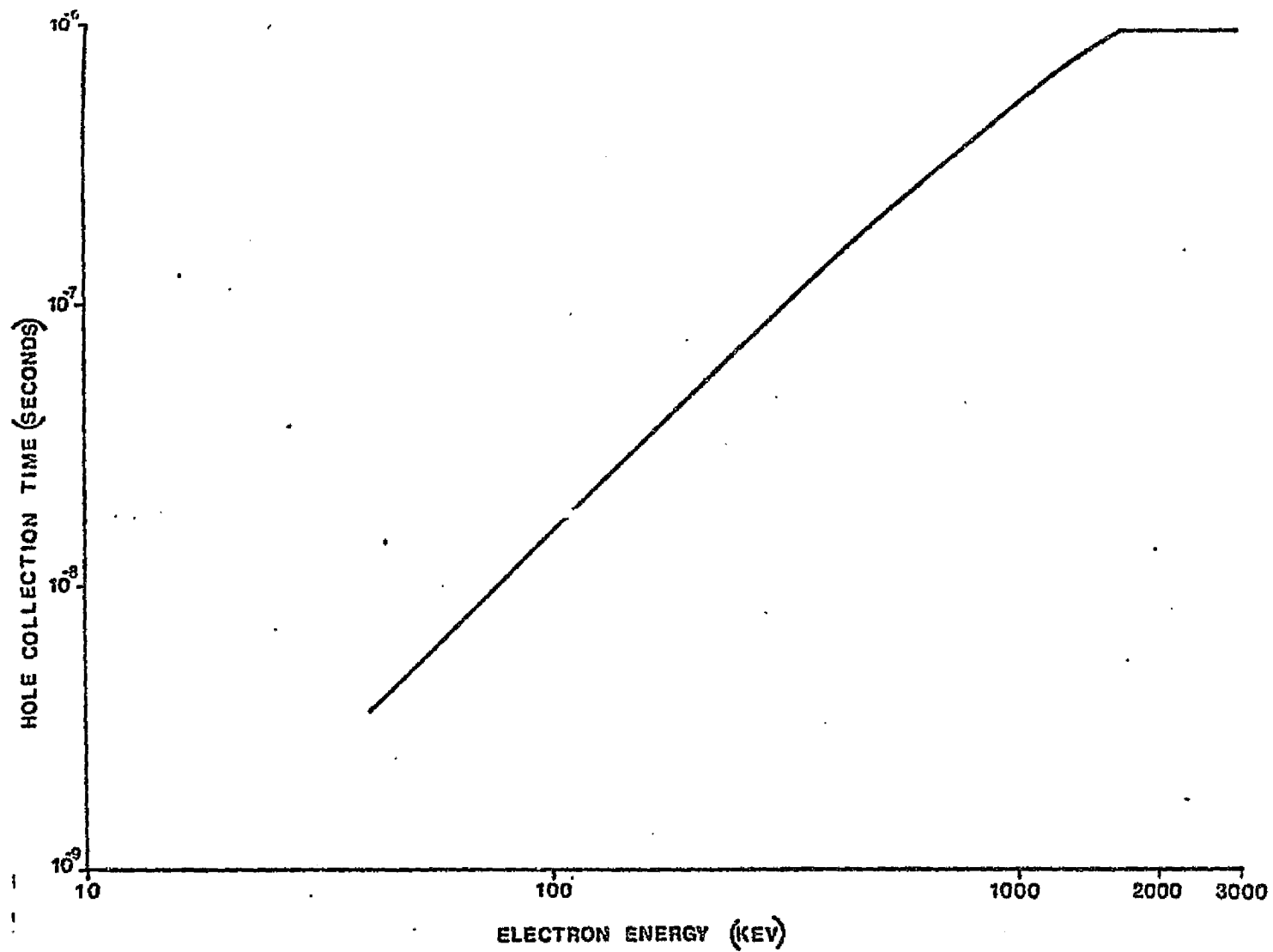


FIGURE 29. TOTAL COLLECTION TIME FOR POSITIVE CARRIERS IN 3 MM. OF SILICON AT 180 VOLTS BIAS POTENTIAL AS A FUNCTION OF ELECTRON ENERGY.

A significant quantity of collectable charge is thereby produced very near to the end of the particle path (Kobetich and Katz, 1968). The collection time of the charge or equivalently the pulse rise time of detector signal is a function of the particle energy. With this fact in mind one normally designs pulse circuits with time constants longer than the longest expected pulse rise times. This provides for complete charge collection and a linear relationship between charge and particle energy. If one chooses to make the pulse circuit time constants of the same order as the charge collection times, thereby gaining increased count-rate ability, the collected charge and particle energy are no longer linearly related and the energy resolution is degraded at high energies. With the wide dynamic range of predicted particle fluxes in REP events, our main concern was for a great count rate capability. As we also did not intend to take advantage of the fine energy resolution at high energy available from the P-I-N detectors, short pulse circuit time constants seemed to provide a very reasonable compromise for our experiment.

The charge sensitive preamplifier and post-amplifier combination were to have a maximum average count rate of 200 Khz. Allowing for random spacing between counts we set a minimum time resolution of the order 500 nsec. In Figure 2.9 we show a graph of positive charge collection time versus particle energy for our three mm thick detectors. For energies in excess of 700 Kev the collection times are as long or longer than the 500 nsec time constants, thus giving us a non-linear pulse height vs. energy relation.

In Figure 2.10 we show the basic amplifier system. The initial stage is a charge sensitive preamplifier, which is followed by two post



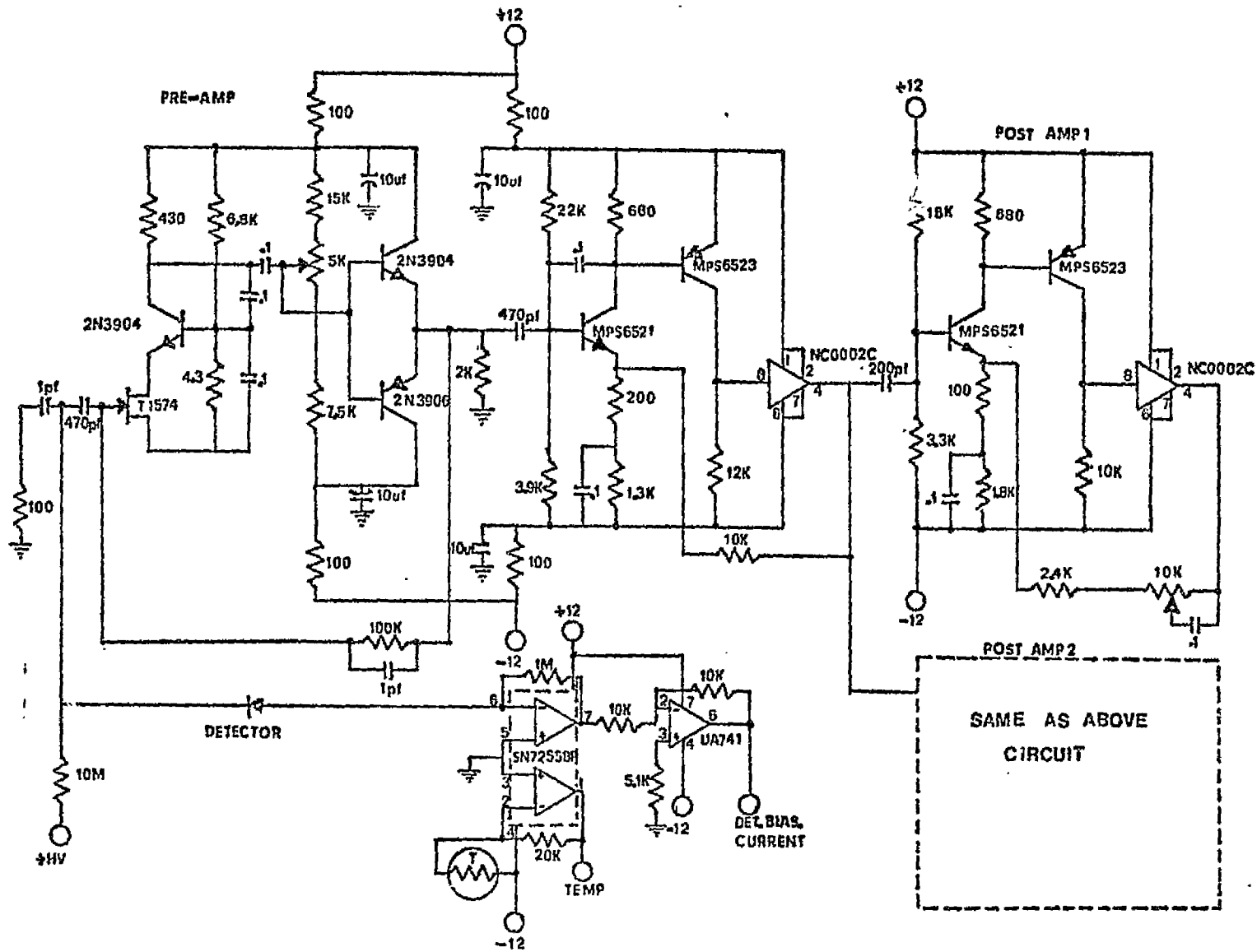


FIGURE 2.10. THE BASIC AMPILFIER SYSTEM.

amplifiers in parallel with each other. The pulse height discriminators are shown in Figure 2.11. The five lowest discriminators received the pulse signal from postamplifier A and the four highest received the pulse signal from postamplifier B. The discriminator logic allowed only one counter to receive a pulse for each charge pulse on the detector. The discriminators were also inhibited during the time a pulse was being processed. The charge terminator at the input of the preamplifier enabled us to calibrate a fast rise time (less than 10 nsec.) pulse generator in terms of equivalent energy pulse. As the rise time of these pulses were very short compared to 500 nsec. we have, therefore, a source of equivalent energy pulses that would yield a linear output pulse height versus equivalent energy (charge) input.

Also shown in Figure 2.11 are the detector bias current and temperature monitor. The normal detector reverse bias currents were of the order of a few microamps. Any large deviations were indicative of break-down. The over-all noise of the detector amplifier system was quite temperature dependent so that significant degradation of resolution would occur at high temperatures. The monitors were included as warnings of these possible malfunctions.

As we have indicated, the output pulse height of the amplifier systems as a function of input pulse height and rise times is a very important characteristic of this system. Figure 2.12 shows a typical calibration determined with a variable rise time linear pulser. What is displayed is the amplifier efficiency,  $E$ , defined by the relation

$$E = \frac{\text{gain at rise time } t}{\text{gain at rise time of 10 nsec}}$$

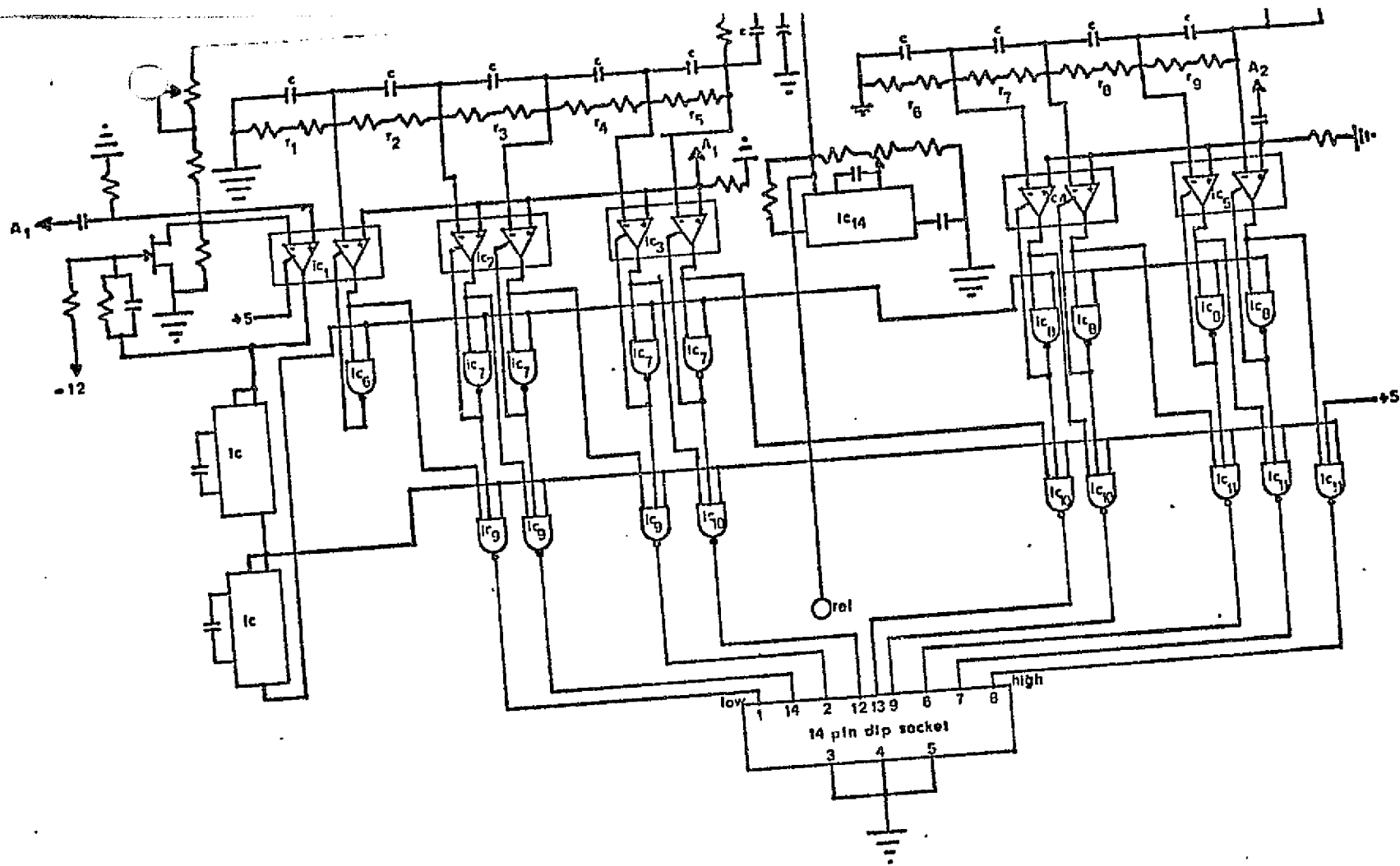


FIGURE 2.11. THE PULSE HEIGHT DISCRIMINATOR.

The amplifiers were perfectly linear as a function of input pulse-height so that these curves were independent of pulse-height. As we see the efficiency begins to fall off at about 100 nsec rise time, which is one-fifth of the preamplifier time constant.

The resistor string across the top of Figure 2.11 is a simple voltage divider. The relative values of these voltages determine the level at which each discriminator triggers. If the system were linear it would be necessary only to make these voltages proportional to the desired energy thresholds. Since the output pulse height was not linearly related to the energy of the incident electrons we had to use a somewhat more involved procedure:

For each preamplifier-post amplifier combination we determined the efficiency as a function of rise time (Figure 2.12). Knowing the charge collection time as a function of energy we then produced the output pulse height as a function of incident energy by performing the convolution of  $E$  with the collection time. The collection time was determined by calculating the time required for the most distant charges produced by the ionizing electrons to be swept to the electrodes of the detector. The entrance surface for the electrons was the p-type gold surface of the detector. As the junction is maintained at a reverse bias the positive carriers (holes) are collected at the gold electrode and the negative carriers (electrons) are collected at the aluminum electrode. The total rise time of the electron charge collected on the aluminum electrode is therefore independent of energy since total collection requires the electrons be swept across the entire thickness of the detector. The rise time of the hole charge on the gold electrode is given approximately by the expression

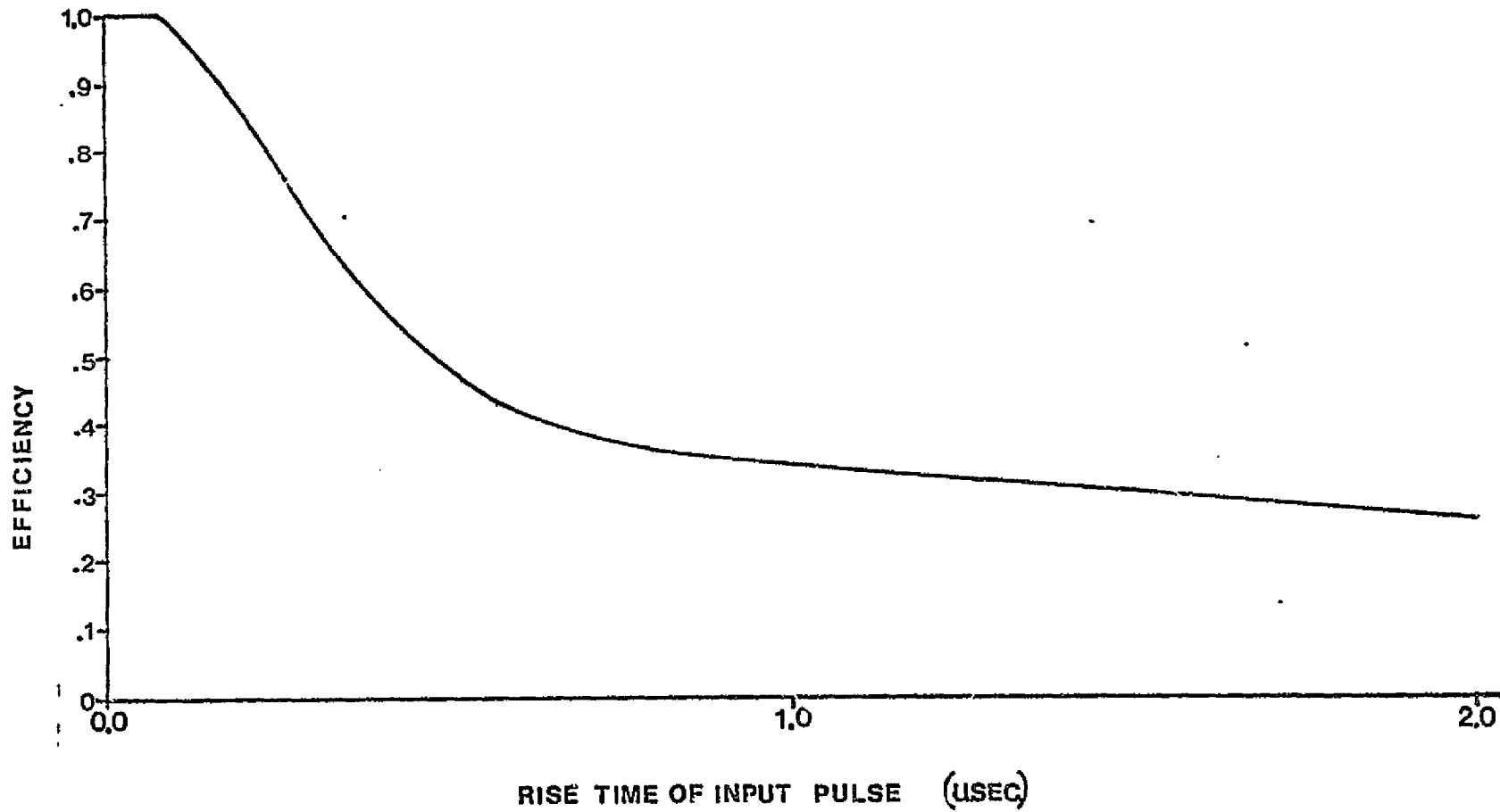


Figure 2.12. Amplifier output pulse height at constant input pulse height as a function of input pulse rise time.

$$\tau_{cp} = \frac{dr}{\mu_p V} \quad (2.9)$$

where  $d$  is the detector thickness,  $r$  the depth of penetration of the ionizing particle,  $\mu_p$  is the hole mobility and  $V$  is the potential between the electrodes (Dearnaley and Northrup, 1966). As shown by Weber (1964) the average penetration depth of electrons into various materials is well represented by the formula

$$r = AE \left(1 - \frac{B}{1+CE}\right) \quad (2.10)$$

where  $E$  is the energy of the incident electron and  $A$ ,  $B$ , and  $C$  are constants characteristic of the stopping medium. This formula was applied to the graph of penetration depth vs. energy given by Dearnaley and Northrup (Dearnaley and Northrup, 1966) with the resulting values of

$$A = 2.205 \times 10^{-3}$$

$$B = .9476$$

$$C = 2.292 \times 10^{-3}$$

Combining equations 2.9 and 2.10 we produced the curve of hole charge collection time vs. energy as shown in Figure 2.9. This result was then folded through the efficiency curves for each preamplifier-postamplifier combination to produce the pulse-height vs. energy curve shown in Figure 2.13. The pulse height is expressed in equivalent energy units. The relationship is linear up to an electron energy of 320 Kev at which energy the hole rise time becomes greater than 0.1  $\mu$ sec and part of the hole charge is lost. The vertical lines superimposed on

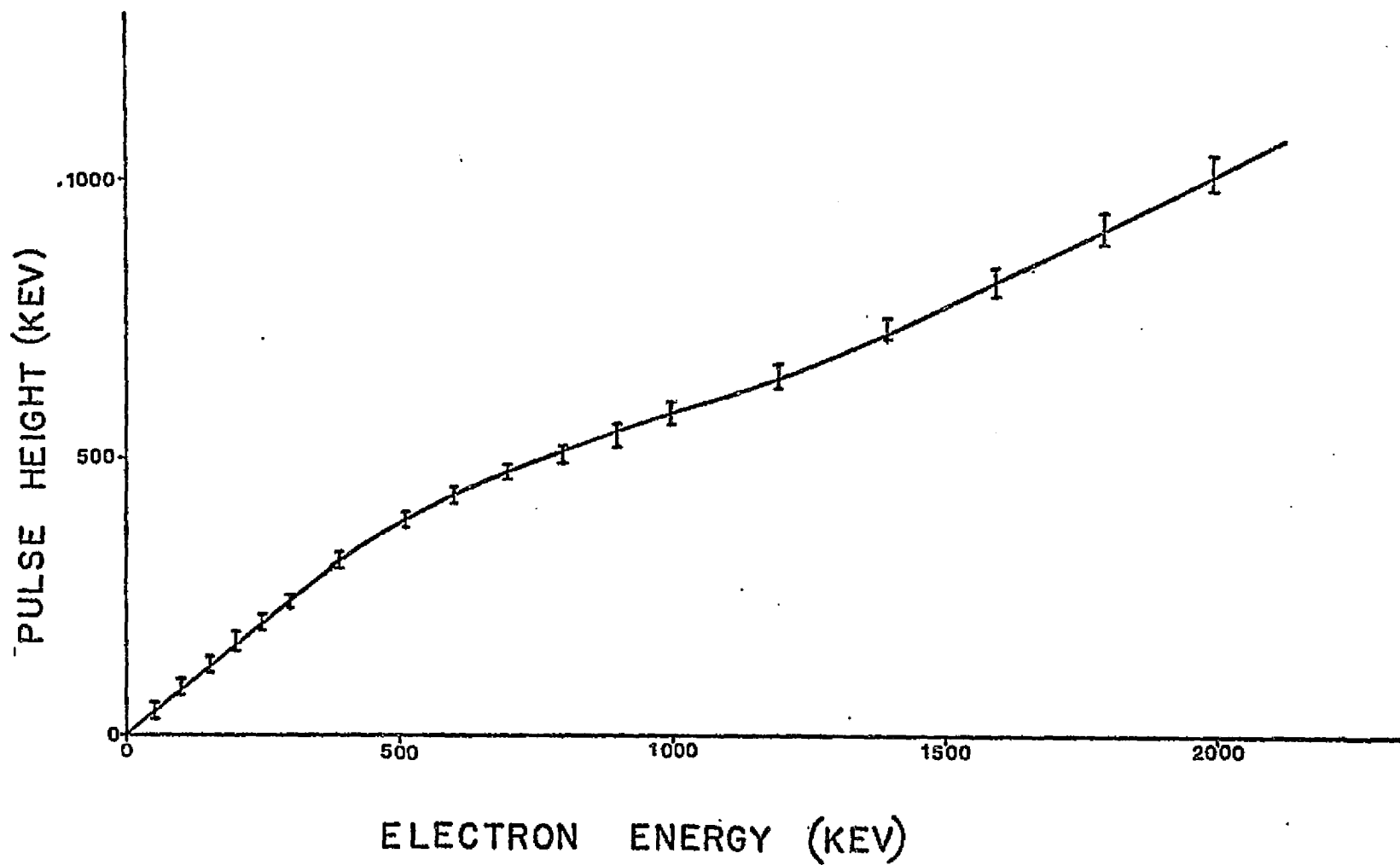


Figure 2.13. Pulse height as a function of energy.

The solid line is the theoretically determined pulse height. The vertical lines were determined experimentally.

the curve are the pulse heights measured from electrons produced on the 2 Mev Van de Graaff accelerator at Goddard Space Flight Center. We will discuss this further in the next section.

The values of the resistors in the pulse height discriminator were now determined (in a straight forward manner) from this curve. The final equivalent energy triggering level of each discriminator was checked with the 10 nsec rise time pulses from the linear pulser.



## II.E. Calibrations

The calibration of our detectors and associated electronics was performed on the 2 Mev Van de Graaff and 100 Kev electron-proton accelerators at Goddard Space Flight Center. These calibrations were carried out in two stages. The first stage was a determination of the optimum performance characteristics and dead-layers of our lithium drifted solid state detectors using electronics with relatively long circuit time constants and electron beams of low flux. The pulse height analysis was performed by a 10,000 channel Nuclear Data Pulse Height analyzer. The second stage was the calibration of the completed flight model nine channel electron energy spectrometer with collimator and aluminum window.

### 1. The Determination Of Optimum Performance

The detectors were placed in the scattering chamber on a moveable table which could be positioned by remote control to allow for small rotations and lateral movements. A 5 cm<sup>2</sup> lithium drifted solid state detector which could be moved in and out of the electron beam was positioned between our detectors and the chamber entrance. We used this "monitor" as a check on the beam intensity. The electrons were magnetically analyzed before injection into the scattering chamber and therefore had energy resolution far better than the 25 Kev resolution of the system being calibrated (on the order of .1%).

The pulse height spectrum for each sampled detector was taken at numerous energies between 100 Kev and 2.0 Mev. A typical spectrum is shown in Figure 2.14a for a 150 Kev beam. The large gaussian shaped peak is called the absorption peak and is the result of particles leaving all their energy in the active region of the detector. The long

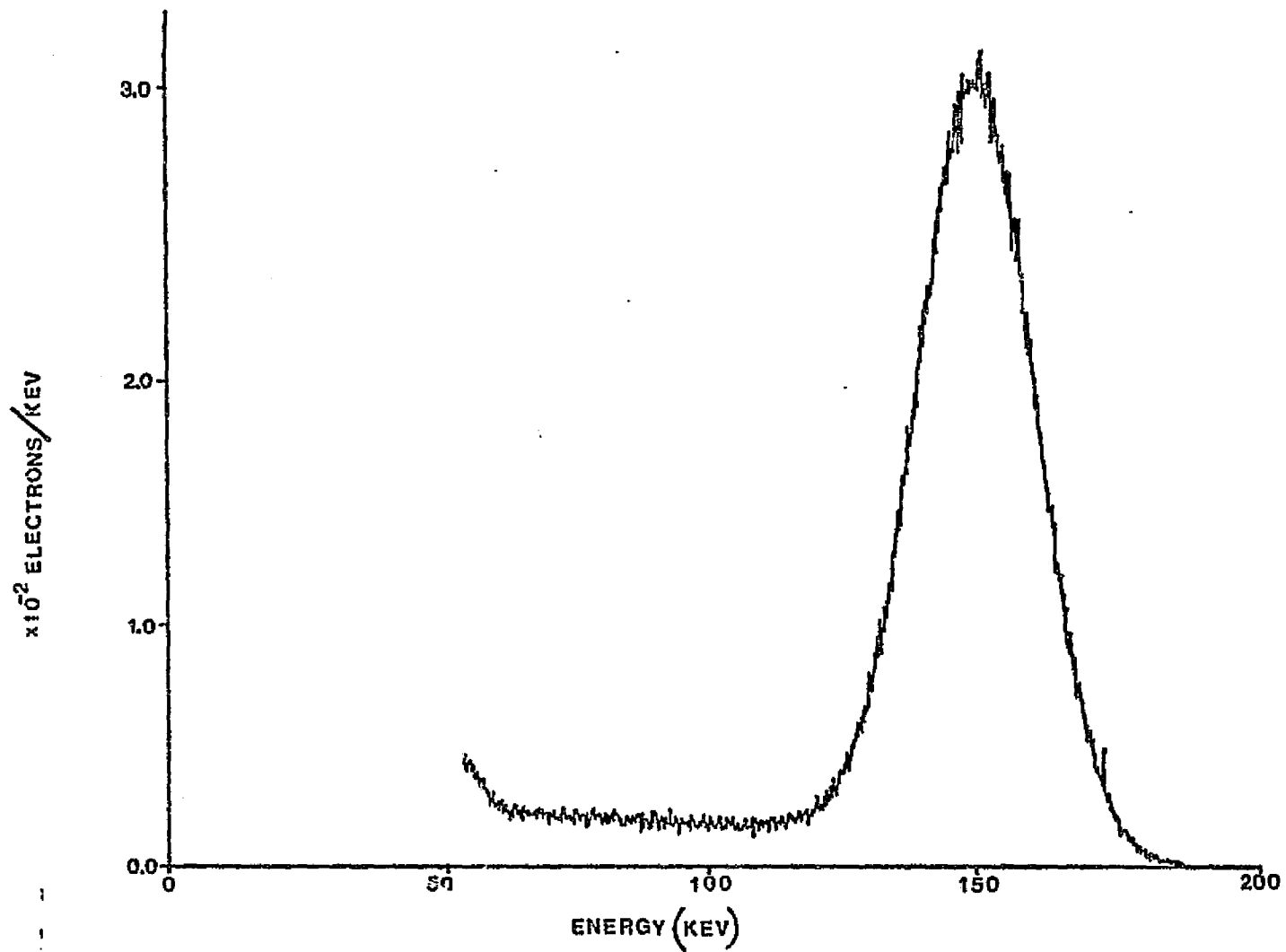


FIGURE 2.14A. MEASURED PULSE HEIGHT SPECTRUM FROM 150 KEV ELECTRONS STOPPING IN 3 MM OF SILICON.

tail extending toward lower energies results mainly from particles escaping out the front of the detector and a small portion out through the sides. This is termed the escape component. The increase toward lower energy (near 50 Kev) is due to noise counts above the lower threshold of the analyzer.

The monitor detector, like the ones being calibrated, has a lower threshold and a thin gold layer on the entrance surface of about  $20 \mu\text{gm}/\text{cm}^2$ . This meant that we could not rely on the monitor to obtain absolute counting efficiency. Though the corrections were generally small (less than 10%) we adjusted efficiencies to correspond with the tabulations in Berger and Seltzer (1969). They have written a monte carlo computer program which follows the life histories of 10,000 electrons and their secondaries as they stop in various materials. Berger and Seltzer (1969) contains complete results of energy deposition spectra for electrons stopping in silicon and comparisons of the theoretical results with numerous experiments for the energy range 150 Kev to 10 Mev. For each energy of interest we produced the theoretical spectra according to the procedures outlined in Berger and Seltzer (1969). Such a spectrum is shown in Figure 2.15b. We then normalized the measured spectra by setting the area within one full-width-half-maximum of the absorption peak equal to the same area under the theoretically determined spectra. The normalized spectra corresponding to that in Figure 2.14 is shown in Figure 2.16. For energies greater than 2 Mev for which we could not obtain actual electron measurements we adopted the spectra from Berger and Seltzer (1969).

The spectra determined on the Van de Graaff, renormalized as we have explained and corrected for transmission through the aluminum foil gave us a set of functions  $F(e,E)$ , where  $e$  is the abscissa in

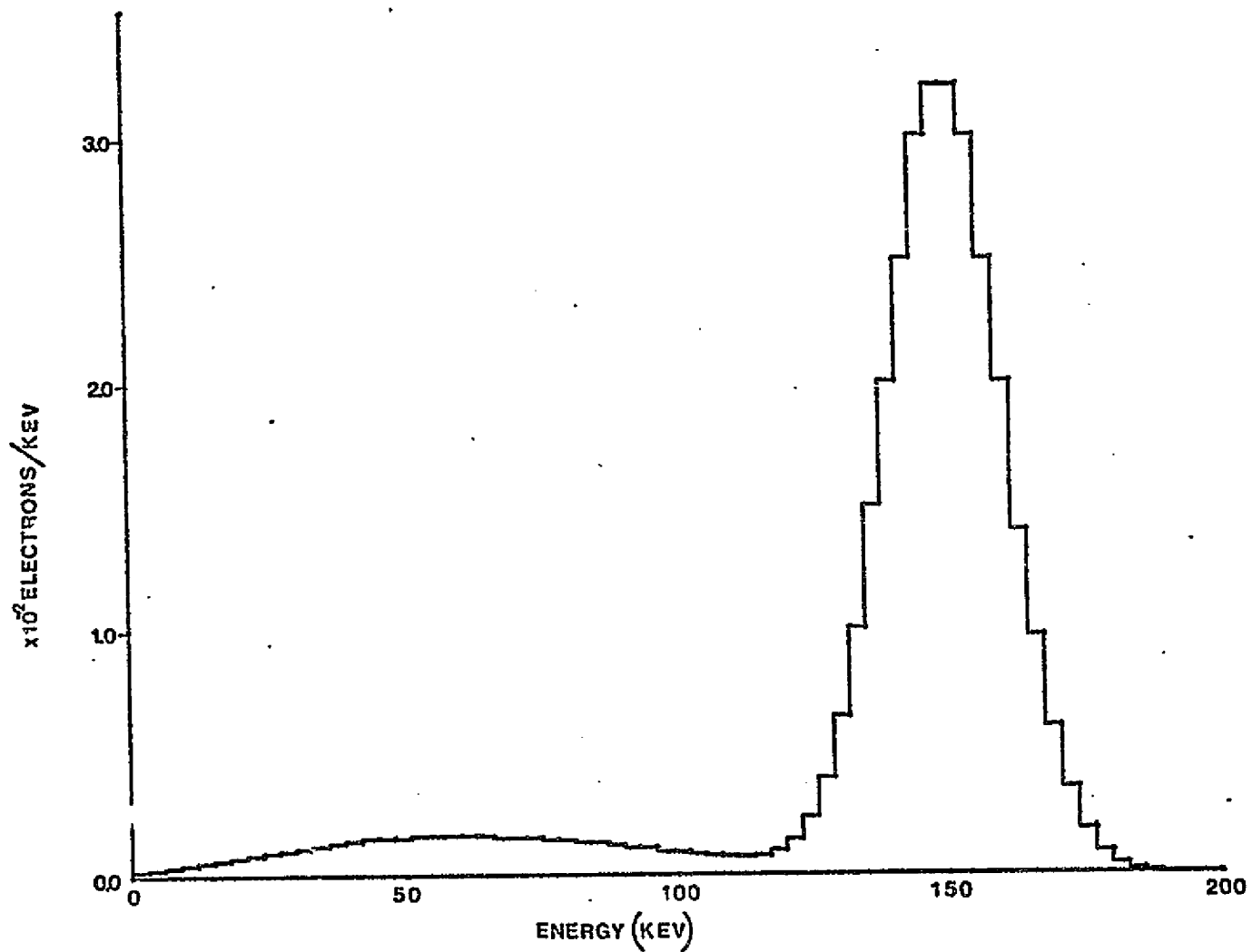


FIGURE 2.14B. THEORETICAL PULSE HEIGHT SPECTRUM OF 150 KEV ELECTRONS STOPPING IN 3 MM OF SILICON (BERGER AND SELTZER, 1969).

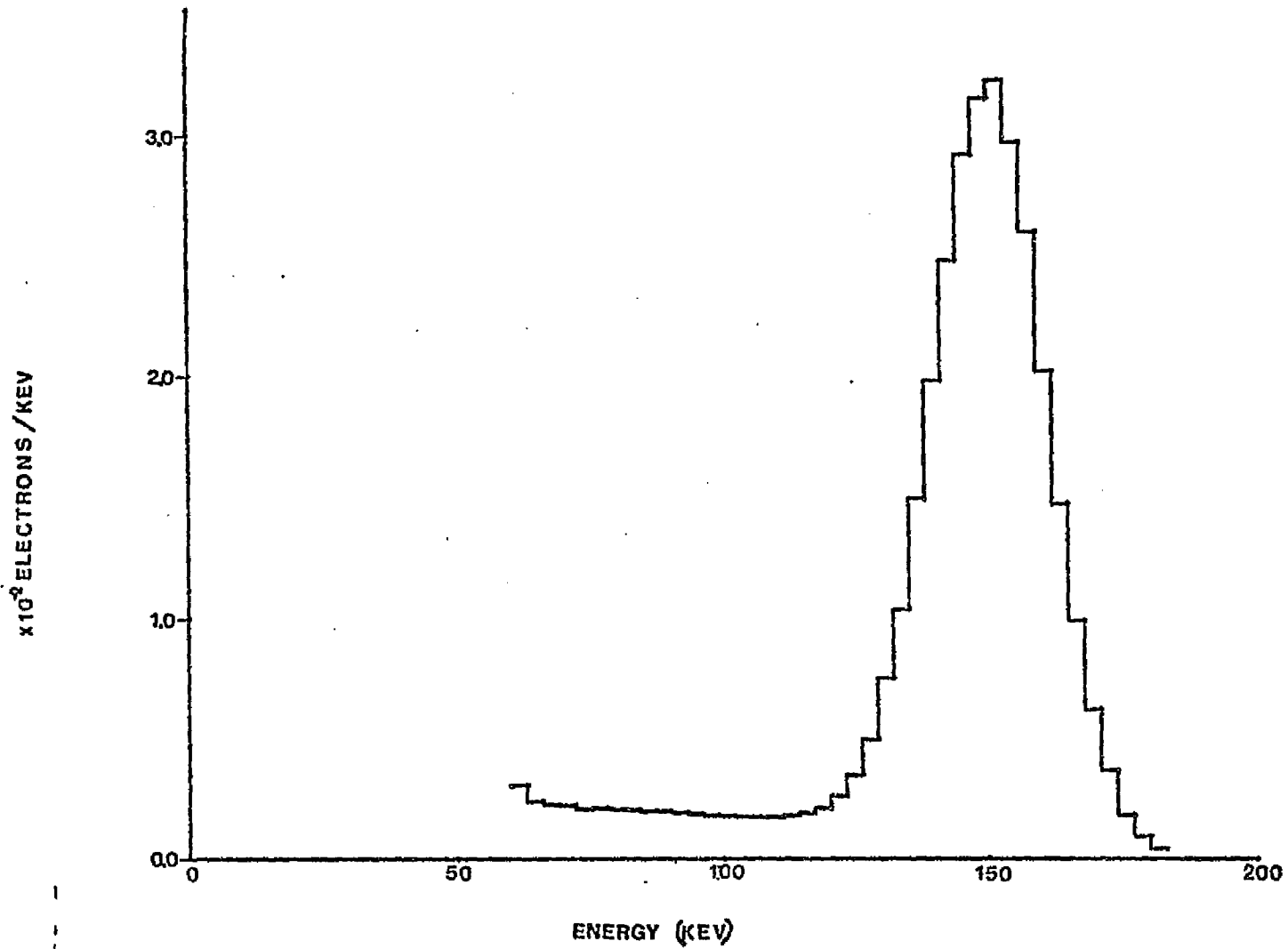


FIGURE 2.15. RENORMALIZED PULSE HEIGHT SPECTRUM FOR 150 KEV ELECTRONS CORRESPONDING TO FIGURE 1.14A.

Figure 2.15 and  $E$  is the energy of the incident electrons. To determine the response of a channel from the nine channel analyzer with lower threshold  $e_1$  and upper threshold  $e_2$  to electrons of energy  $E$  we evaluate the integral

$$R(E) = \int_{e_1}^{e_2} F(e, E) de \quad (2.11)$$

The nine response functions for two spectrometers are shown in Figs. 2.16a & b by the solid lines. We built six complete systems and determined the response functions in the above manner for each system.

## 2. Final Calibrations

During the second stage of calibrations there were five specific characteristics of the completed systems that we checked: (1) the non-linear pulse height vs. energy relation discussed in section II.D, (2) the energy response functions of the nine channel spectrometers, (3) the dependence of the response functions on particle count rates, (4) the efficiency with which x-ray counts were excluded by the collimator shielding, and (5) angular acceptance of the collimator.

The collimator-preamplifier assembly with the aluminum light shield was mounted on a remotely controlled moveable table with a  $5 \text{ cm}^2$  solid state detector again used as a "monitor". To reduce scattering in the collimator the electron beam entered the scattering chamber through a 2 mm diameter aperture and the table position was adjusted until a maximum counting rate was achieved.

The pulse height vs. energy relationship was determined by using electrons of eighteen different energies between 50 Kev and 2 Mev. The

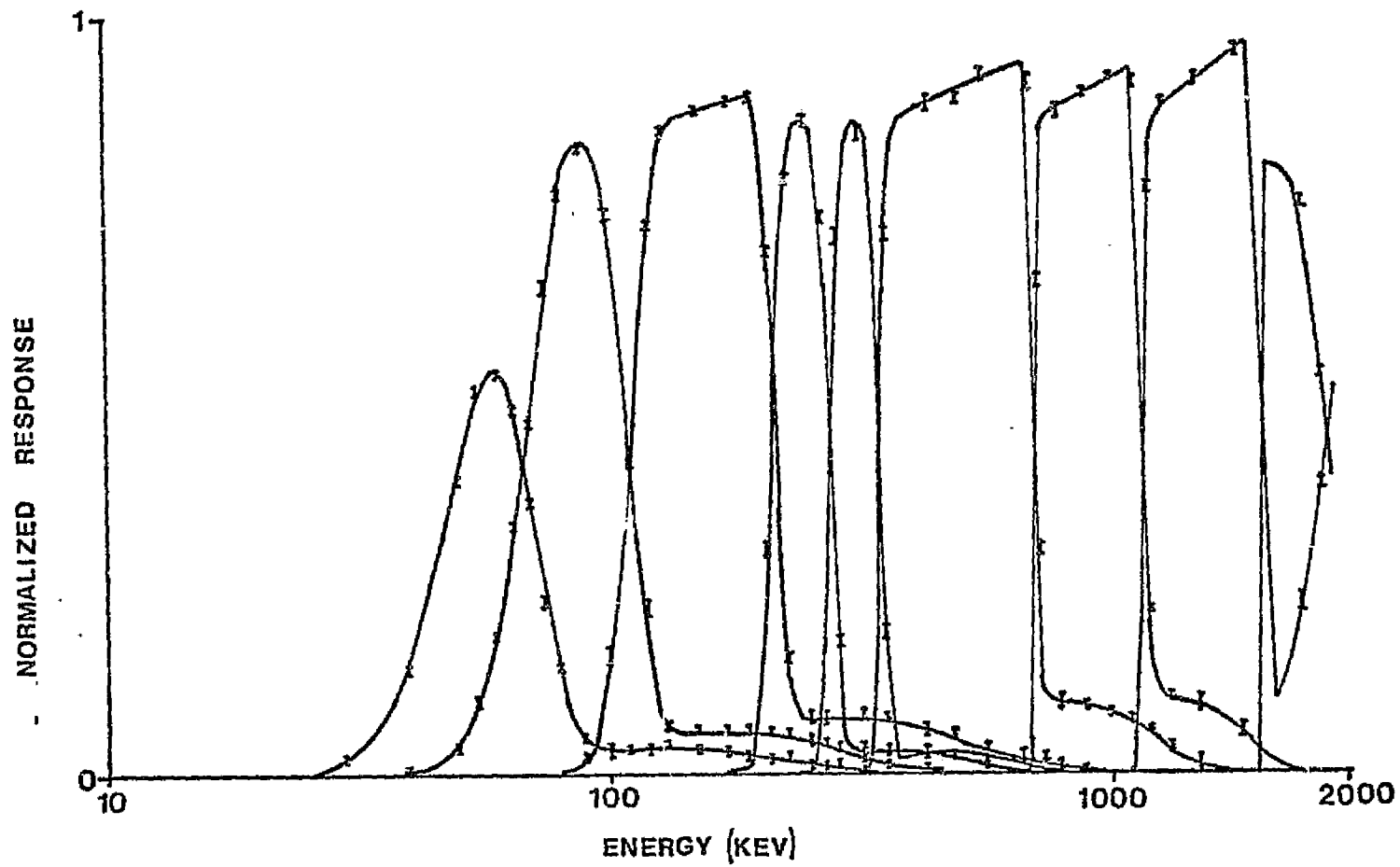


Figure 2.16a. The nine response functions for spectrometer 3.

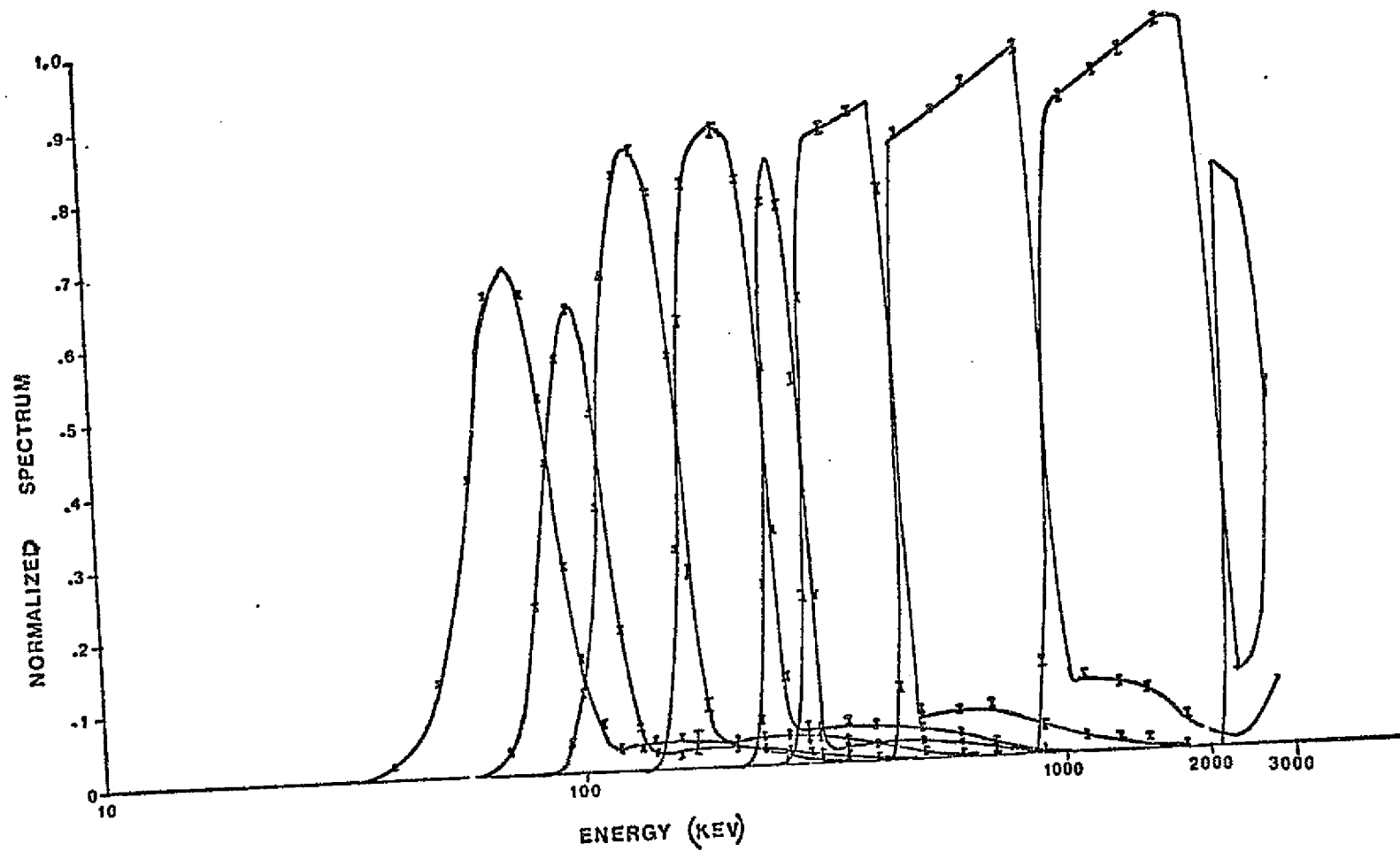


Figure 2.16b. The nine response functions for spectrometer 5.



output from the postamplifiers was displayed on an oscilloscope while electrons were incident on the detector and a calibrated linear pulser provided a reference signal to determine the equivalent energy pulse height. The results for one such calibration are shown by the crossed lines in Figure 2.13. The agreement between the modeled relation and the measured one were in each case of the same quality as shown in this example.

To determine the response functions of the nine channel analyzer required 40 energies between 20 Kev and 2 Mev. The beam intensity was checked with the monitor detector before and after each energy. If the intensity of the beam varied by more than ten per cent the data were re-taken. To determine the absolute efficiency the count rate in the monitor detector was corrected for transmission through  $20 \mu\text{gm}/\text{cm}^2$  of gold (the entrance electrode of the monitor detector) and for counts below the noise threshold (using the data from Berger and Seltzer (1969)). The crossed lines in Figure 2.16 are the points determined in this manner. The error indicated by these points is due strictly to the variations in the beam intensity over the counting period since each point was determined by well over 20,000 counts. The response function as determined by the integrals in equation 2.11 were in excellent agreement with the points determined in this calibration procedure, as is evident from Figure 2.16.

For selected energies between 50 Kev and 2 Mev, points on the response functions were also checked at six different beam intensities. The intensities were adjusted so as to give approximate count rates of 10, 25, 50, 100, 150 and 200 kilohertz in the detectors. The values for several energies and different count rates for one such calibration are

shown in table 2.4. In each case there was no significant change in the value of the points determined. This result implied that the pulse circuitry introduced no count rate dependence and that there was no pulse pile-up at even the high rate of 200 kilohertz. It was to this end that we designed the pulse circuitry with such short time constants.

The collimator opacity to x-rays was the next characteristic that was checked. The first element of the collimator baffles was removed and replaced by an identical piece with no entrance aperture. The collimator was then subjected to beams of electrons of varying intensity and several energies between 50 Kev and 2 Mev. Table 2.5 shows the results of this determination. In each case the x-ray count rates are very small so that we could ignore them when performing the final analysis of the data.

The geometrical factor  $G$  for the collimator was determined by the parameters  $R_1$ ,  $R_2$  and  $h$  as defined in Figure 2.2 and related to  $G$  by equation 2.5. As it is very difficult to produce an isotropic beam of energetic electrons we had to attempt to determine the parameters by a less direct approach than measuring  $G$  itself. We constructed a mounting which allowed us to rotate the collimator-detector housing about an axis that passed directly through the center of the exposed face of the solid state detector. The detector and collimator were exposed to a monodirectional beam of electrons while supported on the rotatable table. The beam was diffuse and covered the entire aperture of the collimator. This assembly was then rotated in steps of one degree about the axis while the count rate was monitored. In this fashion we determined the angular response of the collimator to a monodirectional beam making an angle  $\alpha$  with the collimator axis. This response is

TABLE 2.4 - Uncorrected counting efficiencies at several rates for discriminator 3. (GSFC - April 14, 1972)

E=100 kev	Approximate particle rate at detector			
	10Hz	50Hz	150Hz	200Hz
CH - 1	.115	.116	.115	.115
CH - 2	.775	.775	.773	.773
CH - 3	.021	.022	.023	.021
CH - 4	0.0	0.0	0.0	0.0
CH - 5	0.0	0.0	0.0	0.0
CH - 6	0.0	0.0	0.0	0.0
CH - 7	0.0	0.0	0.0	0.0
CH - 8	0.0	0.0	0.0	0.0
CH - 9	0.0	0.0	0.0	0.0

E=300 kev	Approximate particle rate at detector			
	10Hz	50Hz	150Hz	200Hz
CH - 1	.0179	.0173	.0180	.0175
CH - 2	.0243	.0242	.0242	.0241
CH - 3	.0517	.0517	.0515	.0520
CH - 4	.735	.736	.736	.738
CH - 5	.152	.155	.154	.153
CH - 6	0.0	0.0	0.0	0.0
CH - 7	0.0	0.0	0.0	0.0
CH - 8	0.0	0.0	0.0	0.0
CH - 9	0.0	0.0	0.0	0.0

E=1200 kev	Approximate particle rate at detector			
	10Hz	50Hz	150Hz	200Hz
CH - 1	2.00E-4	2.07E-4	2.03E-4	2.03E-4
CH - 2	4.27E-4	4.27E-4	4.33E-4	4.26E-4
CH - 3	2.19E-3	2.18E-3	2.17E-3	2.21E-3
CH - 4	6.58E-3	6.57E-3	6.62E-3	6.57E-3
CH - 5	3.95E-3	3.99E-3	3.94E-3	3.98E-3
CH - 6	6.81E-2	6.81E-2	6.78E-2	6.79E-2
CH - 7	1.95E-1	1.96E-1	1.91E-1	1.92E-1
CH - 8	7.59E-1	7.51E-1	7.62E-1	7.59E-1
CH - 9	0.0	0.0	0.0	0.0

TABLE 2.5 - X-ray counts per electron at several energies.

Energy (kev)	<u>CH-1</u>	<u>CH-2</u>	<u>CH-3</u>	<u>CH-4</u>	<u>CH-5</u>	<u>CH-6</u>	<u>CH-7</u>	<u>CH-8</u>	<u>CH-9</u>
400	0.0	0.0	0.0	0.0	.20E-6	.21E-4	0.0	0.0	0.0
600	0.0	0.0	0.0	.43E-6	.62E-6	.31E-5	.40E-6	0.0	0.0
800	0.0	0.0	0.0	.71E-6	.11E-5	.69E-5	.41E-5	0.0	0.0
1000	0.0	0.0	0.0	.12E-5	.14E-5	.94E-5	.77E-5	.29E-6	0.0
1500	0.0	0.0	.19E-6	.30E-5	.35E-5	.27E-4	.30E-4	.10E-4	0.0

shown in Figure 2.17 by the short horizontal lines. Using the values of  $R_1$ ,  $R_2$  and  $h$  given in table 2.2 we determined numerically what this angular response should be. (This calculation is described in appendix A-3). These values are shown by the solid line in Figure 2.17. As can be seen from the figure the measured width of the collimator is slightly broader than the width determined from the measured values of the parameters but well within the error bars. This excess might be due to a small amount of elastic scattering from the sharp edges of the baffles. Increasing the values of  $R_1$  or  $R_2$ , or decreasing the value of  $h$  will not account for this slight bowing, in that the measured angular width goes to zero at the predicted value of  $\alpha$ .

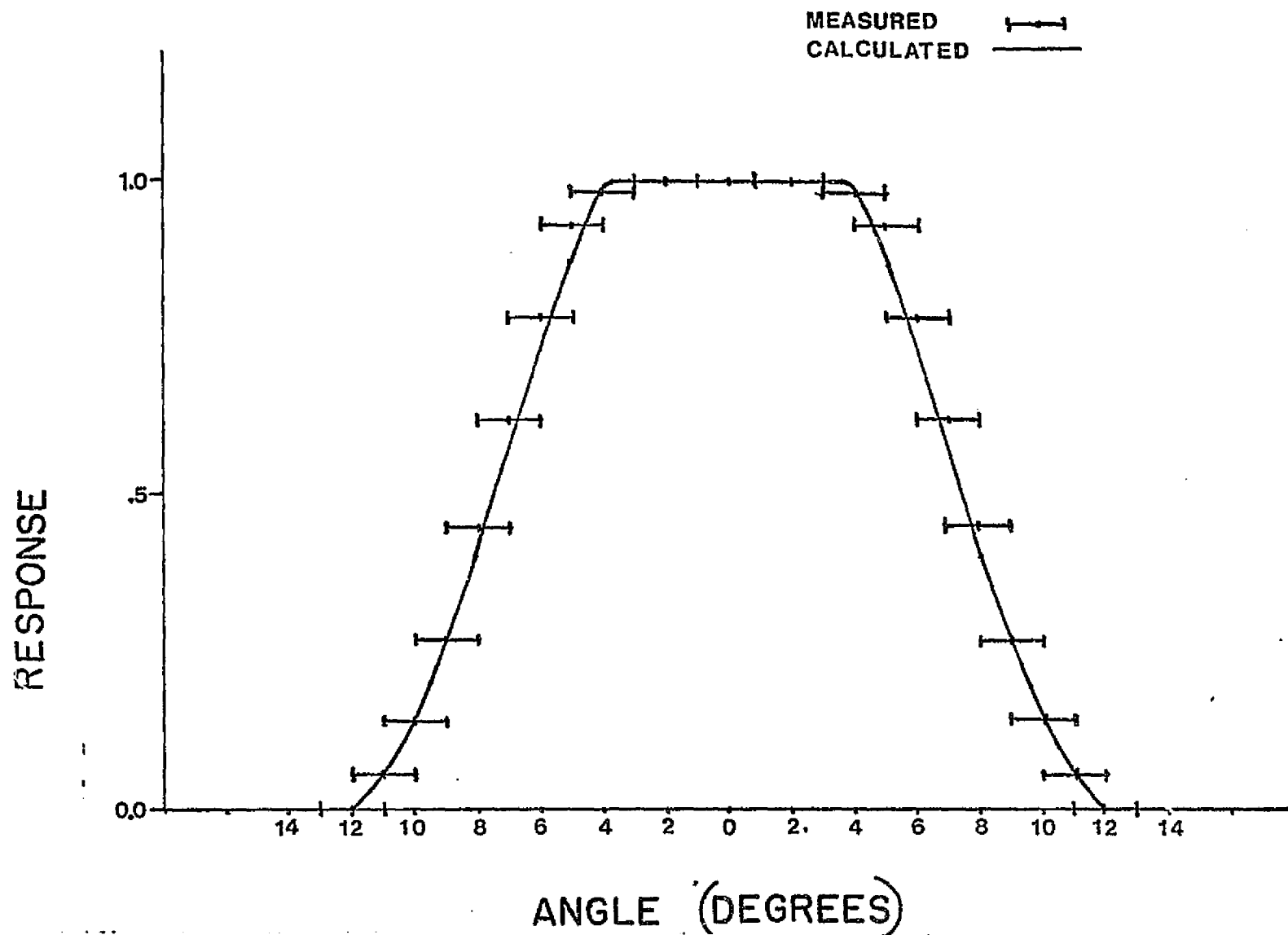


Figure 2.17. Angular response of the collimator to monodirectional electrons.  
The solid line was determined according to the formulas developed in appendix A.3. The horizontal lines were experimentally determined.

## II.F. Energy Response Of The Analyzers To Protons

The pulse height coming from the peramplifier and postamplifier combination, as we have indicated, was a function of the particle energy. This was due to the dependence of the charge collection time on the depth of penetration of the ionizing particles into the silicon detector. The particle penetration depth is a function of the particle's mass and charge as well as energy. One should therefore anticipate that the equivalent energy thresholds of the analyzer would be charge species dependent. Though it was anticipated that the primary source of ionization would be electrons, we had to be prepared to identify protons if they were present and compensate for them in the data analysis. There was a separate proton detector included in the rocket instrumentation.

Protons straggle far less than electrons because of their greater mass. In addition a one Mev proton will penetrate only on the order of 17 microns into silicon. (Northcliffe and Schilling, 1970). At a depth of 17 microns the hole charge was completely collected so that the response of the energy analyzer was linear to the proton energies of interest. The effect of the  $270 \mu\text{gm}/\text{cm}^2$  of aluminum in the light shield and the  $31 \mu\text{gm}/\text{cm}^2$  of gold on the entrance electrode was determined by the use of the stopping power tables in Northcliffe and Schilling (1970). As in the case of the determination of the electron response functions we took into account the charge collection deficit of the negative carrier while assuming the holes were completely collected (see section 2-D). Table 2.6 lists the equivalent energy thresholds of one of the electron spectrometers.

TABLE 2.6 - Energy Response of 45-degree spectrometer  
to Protons.

	Proton Energy (kev)
CH-1	173 - 185
CH-2	185 - 214
CH-3	214 - 270
CH-4	270 - 339
CH-5	339 - 364
CH-6	364 - 506
CH-7	506 - 736
CH-8	736 - 1320
CH-9	1320 - $\infty$



## II.G. PCM Telemetry

The data from the rocket was returned in Pulse Code Modulated (PCM) binary format. The carrier frequency was 240.2 MHz and the bit rate was  $1.2 \times 10^5$  bits/sec. The bit stream was subdivided into 8-bit words, 32-word frames and 32-frame master frames. A single 8-bit word was 66.4  $\mu$ sec long. All three of the spectrometers and the BTL proton experiment accumulated data simultaneously over an accumulation time of 8.53 msec. At the end of this period the counts were stored in a buffer and read serially into the bit stream while the spectrometers were accumulating fresh data. This accumulation period was four frames (32 words) long. The spectrometers each required 10 words while the BTL proton detector required nine words. The data from each of these detectors was therefore injected into the bit stream once every four frames using the same 10 data words each frame as shown in table 2.7. This is referred to as subcommutating. The tenth word on the BTL proton experiment was set at 11111111 to serve as a synch-word and thereby identify the position in the four detector cycle. The analog monitoring data (usually referred to as housekeeping data) such as the detector temperature and current monitors was converted to digital (A to D) and subcommutated once every 32 frames into the bit stream. Table 2.7 lists the basic telemetry frame.

TABLE 2.7-Telemetry Channel Assignment F-34

Video: Frequency 240.2 Mhz

Information rate: 8 bits/word X 32 words/frame X 469 frames/  
is 120,064 bit/sec

Each word 66.4 microseconds

Each bit 8.3 microseconds

bit #	0	1	2	3	4	5	6	7	
word 0	1	1	1	0	0	0	1	0	synch-word
1	0	1	0	0	0	0	1	1	synch-word
2	0	0	0	0	0	0	0	0	open
3	sub-com digital Z								
4	sub-com analog data								
5	Faraday receivers 15.011 MHz								
6	Search coil								
7	Faraday receivers 3.883 MHz								
8	Channeltrons protons 0 degrees								
9	Channeltrons electrons 45 degrees								
10	Channeltrons electrons 90 degrees								
11	UOM and BTL electron-proton experiments								
12			"			"			
13			"			"			
14			"			"			
15			"			"			
16			"			"			
17			"			"			
18			"			"			
19			"			"			
20			"			"			
21			"			"			
22	Search coil								
23	UOM								
24	UOM								
25	UOM								
26	UOM								
27	UOM								
28	UOM								
29	Gerdien probe								
30	NDRE Sun sensor								
31	NDRE Lyman-Alpha probe								

## CHAPTER III

### THE FLIGHT PARAMETERS OF ROCKET F-34

#### III.A. The Trajectory

The rocket's trajectory was determined by a slant range system. The actual trajectory parameters were prepared by the ballistics section of the Andöya Rocket Range, NDRE. In Figure 3.1 we show a diagram of this trajectory. The rocket attained a maximum altitude of 154.43 km at 197 seconds after lift-off. The average flight azimuth was 320 degrees. The rocket attained 90 km altitude at 80 seconds into the flight and remained above this altitude until 314 seconds. For the portion of the flight above 90 km the rocket traveled  $113.5 \pm .9$  km horizontally at azimuth 320 degrees which is some 86 km north and 73 km west.

The aspect determination depended upon the direction of the magnetic field and the direction of the sun. The magnetic field direction was taken from Wiley and Barish (1970). From this model it was determined that the azimuth of the magnetic field varied from 0 degrees to - 1.3 degrees over the entire trajectory, while the dip angle varied from  $72.5^\circ$  to  $72.8^\circ$ . The solar elevation was  $28.9^\circ$  and the solar azimuth was  $102.4^\circ$  at the time of launch. The solar position would have changed by less than  $.3^\circ$  over 400 seconds. We therefore took the magnetic field direction and the sun direction as constants for the aspect determination.

We also note at this point that according to Stassinopoulos (1970) the magnetic field line at 100 km at the position of the rocket extended out to 6.4 Earth radii at the equatorial plane. - -

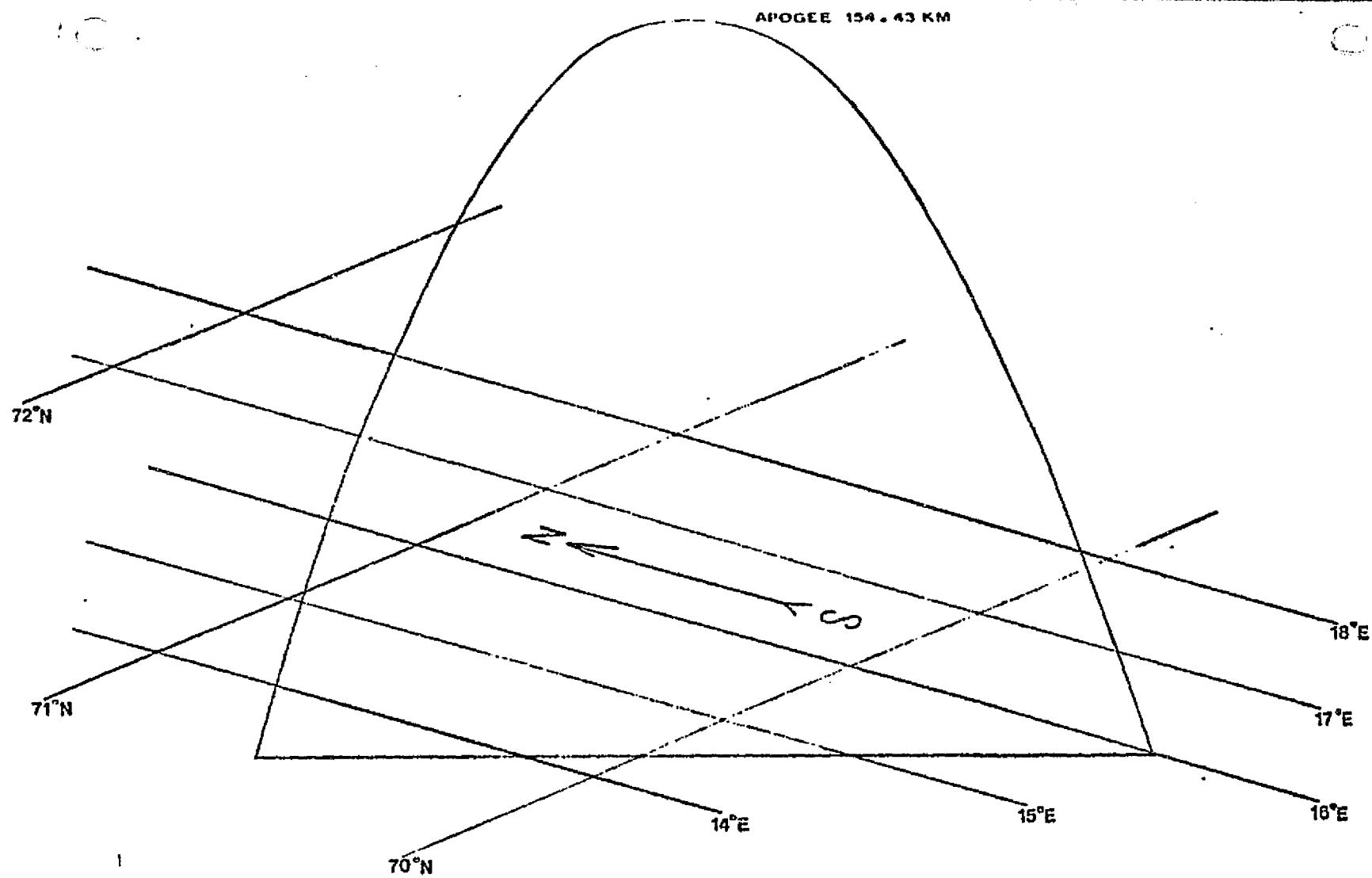


FIGURE 3.1. TRAJECTORY OF ROCKET F-34

### III.B. Determining The Rocket Aspect

The flux of the precipitating particles must be determined with respect to a reference system fixed on the Earth. The obvious choice is one with the Z-axis along the local magnetic field of the Earth since many of the properties we wish to determine relate directly to the magnetic field. The rocket carried an aspect magnetometer, which determined the angle between the rocket axis and the magnetic field as well as giving an accurate account of the rocket's spin rate. In addition, there was a solar aspect sensor which determined the angle between the rocket axis and the sun direction as well as giving a measure of the spin rate. Knowing the elevation and azimuth of the sun and the direction of the local magnetic field it is possible with the data from the sun sensor and the magnetometer to determine the orientation of the rocket in space at all times.

Unfortunately after 70 seconds into the flight the magnetometer data were lost. After a number of unsuccessful attempts we discovered that the electron data from the downward looking spectrometer could be used to determine the information lost by the magnetometer. The procedure was somewhat involved but many of the conclusions of this research are based upon the reliability of the procedure so it warrants detailed discussion.

Figure 3.2 shows the angle between the normal to the rocket axis and the sun direction as a function of time determined from the sun sensor data. (E. Thrane, private communication). The altitude of the rocket from 85 seconds to 300 seconds is above 90 kilometers where the pressure of less than .75 microns is small enough that the drag due to air be neglected and we may assume that the rocket was in free fall. The nose cone was spin-balanced about the rocket axis so that this axis was a rotational

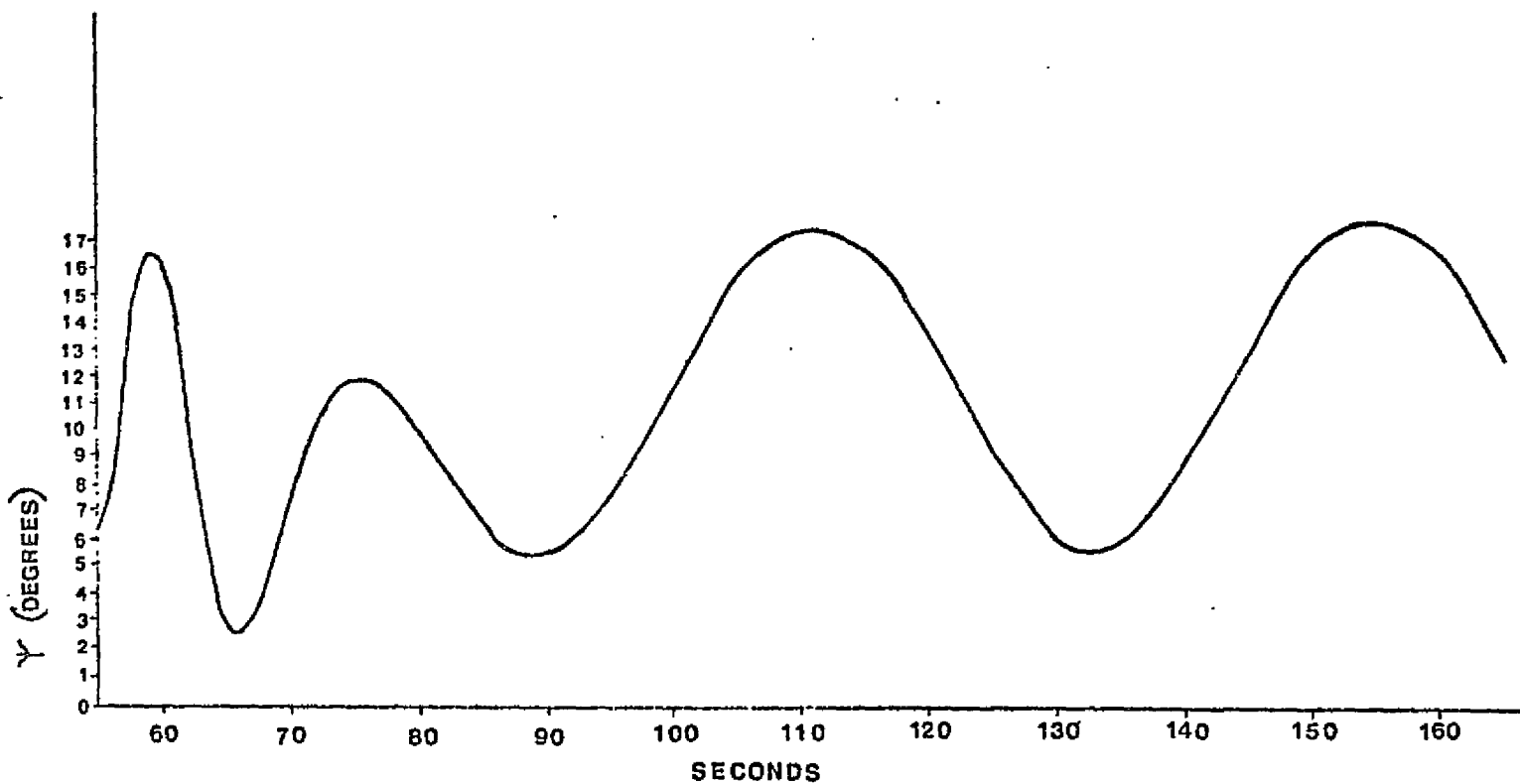


FIGURE 3.2. REDUCED DATA FROM THE SUN SENSOR.

THE ANGLE  $\psi$  IS THE ANGLE BETWEEN THE DIRECTION OF THE NORMAL TO THE ROCKET AXIS AND THE DIRECTION OF THE SUN IN THE PLANE FORMED BY THE ROCKET AXIS AND THE DIRECTION TO THE SUN.

symmetry axis. The free fall motion then consisted of a rotation about the symmetry axis at an angular frequency  $\omega$  and a precession of the spin axis about the direction of the angular momentum at an angular frequency  $\Omega$ . (Goldstein, 1950).

To determine the equation of motion of the rocket it is conceptually simplest to use three coordinate systems which have the same origin and are related by three sets of Euler angles.

1. The rocket coordinate system with  $Z_R$  along the rocket axis,  $X_R$  along the magnetometer axis and  $Y_R$  chosen to form a right handed set.
2. The angular momentum system with  $Z_L$  along the direction of the total angular momentum and  $X_L$  and  $Y_L$  fixed within a right hand system as explained below.
3. The sun-rocket system with  $Z_S$  along the sun direction,  $X_S$  in the local Earth horizontal plane and  $Y_S$  chosen again to form a right handed set.

We are interested here in only the 3 degrees of rotational freedom and will therefore have to fix some of the additional coordinates we are creating.

Figure 3.3 shows the choice of Euler angles that transform from coordinates 1 to coordinate 2. The transformations consist of three simple rotations. One in the  $X_L - Y_L$  plane, followed by a rotation in the  $Y' - Z_L$  plane and the last in the  $X' - Y''$  plane. Angle  $\alpha$  is the half coning angle of the rocket precession about  $Z_L$ .  $X'$  labels the line of nodes which moves around the origin in the  $X_L - Y_L$  plane as the rocket processes so that angle  $\xi$  is the angle of precession. Angle  $\phi$  is the rocket roll angle and is measured from the moving line of nodes.

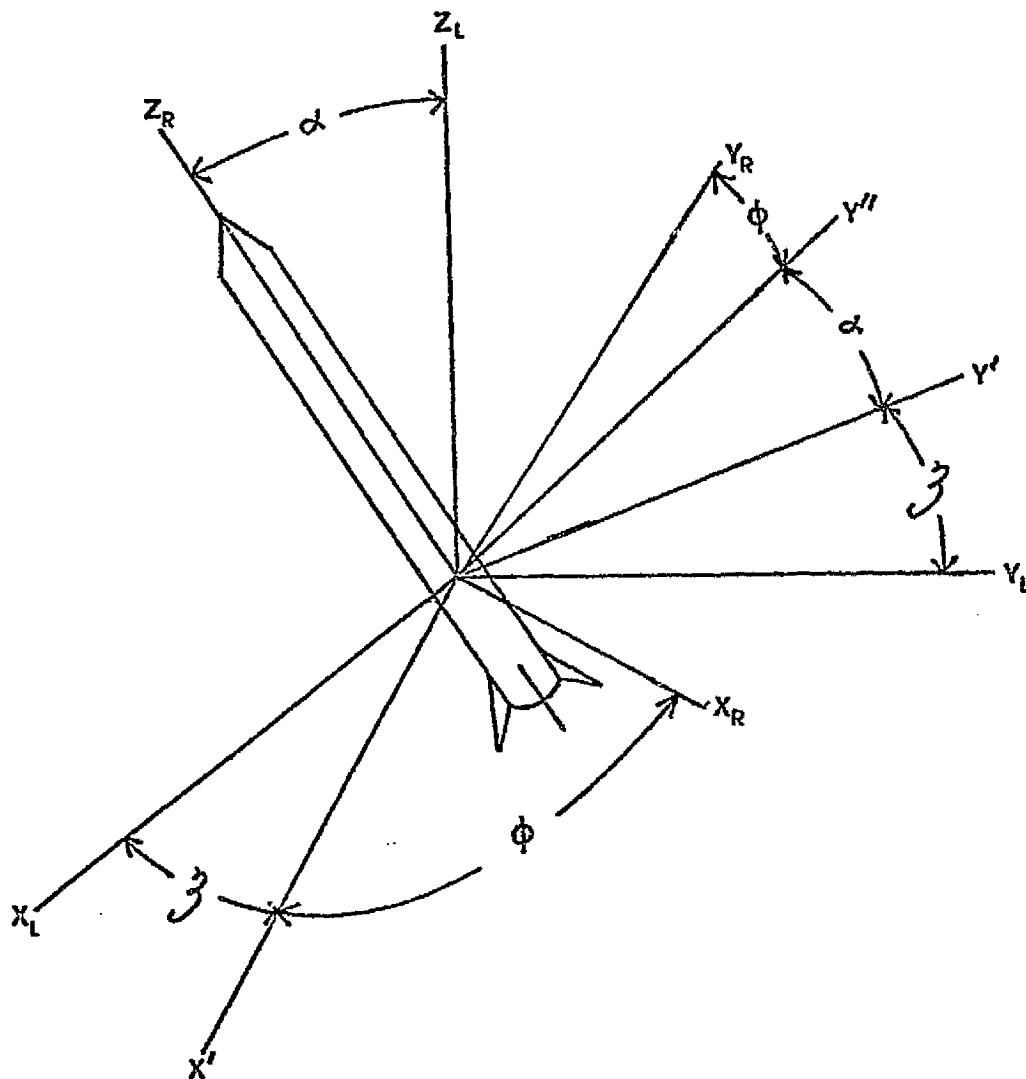


Figure 33. The Euler angles used to define the transformation from angular momentum space coordinates to coordinates fixed in the rocket.



In Figure 3.4 we show the choice of Euler angles that transform from coordinates 2 to coordinates 3. We have set the angle between  $X_L$  and the line of nodes to zero removing one of the excess degrees of freedom. This fixes the direction of  $X_L$  and  $Y_L$ .

The unit vector pointing along the rocket axis in the rocket system is

$$\hat{u}_R = \begin{pmatrix} 0 \\ 0 \\ 1 \end{pmatrix}$$

By performing the successive transformation we express this in the sun-rocket system 3

$$\hat{u}_R = \begin{bmatrix} \cos\psi \sin\alpha + \sin\psi(\cos\mu \cos\xi \sin\alpha + \sin\mu \cos\alpha) \\ \sin\psi \sin\xi \sin\alpha - \cos\psi(\cos\mu \cos\xi \sin\alpha + \sin\mu \cos\alpha) \\ - \sin\mu \cos\xi \sin\alpha + \cos\mu \cos\alpha \end{bmatrix} \quad (3.1)$$

The sunsensor look direction, the rocket axis and the sun direction are related as shown in Figure 3.5

The angle  $\chi$ , which is the angle between the sun direction  $Z_S$  and the normal to the rocket axis (sunsensor look direction), is measured once per roll by the sunsensor. The angle  $\bar{\chi}$  between the rocket axis and  $Z_S$  is related to the projection of  $\hat{u}_S$  on  $Z_S$  by the expression

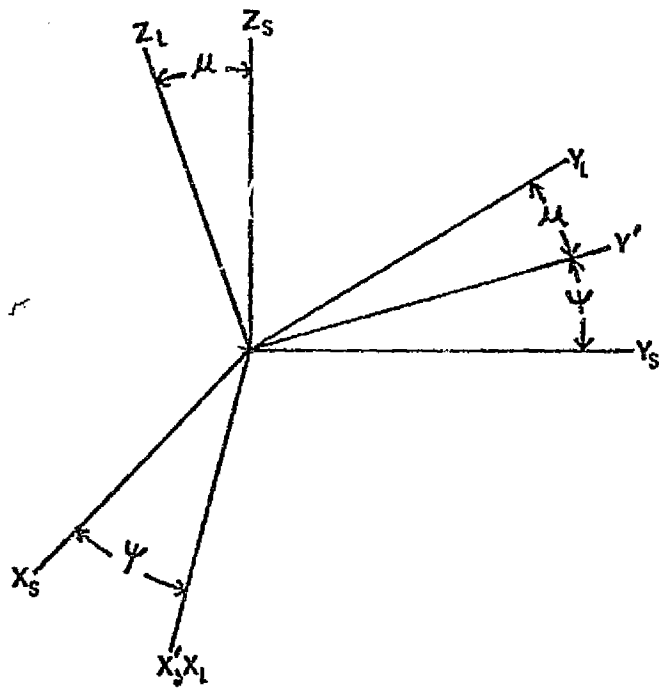


Figure 3.4. Transformation to space coordinates with z-axis in sun direction.

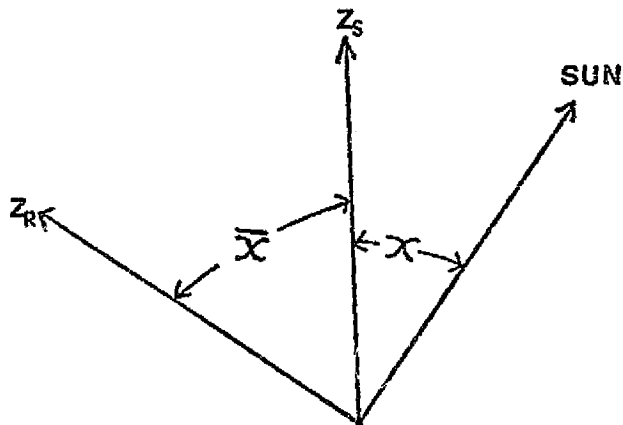


Figure 3.5. Angles determined from sunsensor measurement.

$$\sin\chi = a \cos\xi + b = \cos\bar{\chi} \quad (3.2)$$

with

$$a = -\sin\mu \sin\alpha \quad (3.3)$$

$$b = \cos\mu \cos\alpha$$

We are interested in determining the angles  $\mu$  and  $\alpha$  which may be expressed in terms of  $a$  and  $b$  by the relations

$$\mu = \frac{1}{2} \left[ \cos^{-1}(a+b) + \cos^{-1}(b-a) \right] \quad (3.4)$$

$$\alpha = \frac{1}{2} \left[ \cos^{-1}(a+b) - \cos^{-1}(b-a) \right]$$

We will take  $\xi = \Omega t + \xi_0$  where  $\Omega$  is the precession angular frequency and  $\xi_0$  is an initial angle between the  $X_R$  axis and the line of nodes. The period  $\tau = 2\pi/\Omega$  is determined from the data in Figure 3.2 from which in turn we determine  $\Omega$ . The values of  $\sin\chi$  are related to  $a$  and  $b$  by

$$\begin{aligned} \sin\chi_{\max} &= a + b \\ \sin\chi_{\min} &= -a + b \end{aligned} \quad (3.5)$$

To take advantage of the large number of data points determined from the sunsensor, rather than use relations (3.5), we least-squares fit the equation (3.3) to the data in Figure 3.2, solving for the constants  $a$  and  $b$ . Equations (3.4) then determined the two possible sets of solutions for  $a$  and  $b$  shown in table 2.1. The second set of solutions would imply

that the rocket turned nose down for part of the precession and nose up for part of the precession. The transversal magnetometer continued to function until shortly before the doors of the rocket were opened. The indications were that the rocket had only a small precession cone before the magnetometer began to malfunction at 57.1 seconds. The doors opened at 57.6 seconds which is the time when the solar aspect sensor began to function. It would have required a sizeable impulse to change the rocket's orientation from the small precession cone at 57.1 seconds to the very large cone indicated by solution set 2 in table 3.1. As we will discuss in more detail later, the second solution may also be partly excluded by an examination of the particle data.

Table 3.1

1	2
$\mu = 78.21^\circ \pm 2^\circ$	$\mu = 173.96^\circ \pm 2^\circ$
$\alpha = 6.04^\circ \pm .5^\circ$	$\alpha = 101.79^\circ \pm .5^\circ$

Of the initial five unknown parameters  $\xi$ ,  $\phi$ ,  $\alpha$ ,  $\mu$  and  $\psi$  we have determined three:  $\xi$ ,  $\alpha$  and  $\mu$ .  $\phi$  is the rocket roll angle with respect to the line of nodes. We take  $\phi = \omega t + \phi_0$  and determine  $\omega$  by the following considerations. The sunsensor recorded the time between the crossings of the sunsensor look direction and the sun direction. As the line of nodes makes one  $360^\circ$  precession every precession period the sunsensor data recorded one more sun crossing than the number of rolls. We simply count the number of crossing over the total of full precessions and subtract the number of precessions. This result is divided into the time to determine the roll period which is then converted to a frequency.

The value of  $\omega$  determined by this procedure was identical to that determined from the auto-correlation analysis of the particle data which will be explained in section 3.E.

The determination of  $\phi_0$  was somewhat more arduous and proceeded as follows. The sunsensor look direction is given in the rocket coordinate system 1 by

$$\hat{U}_{SS} = \begin{pmatrix} 1 \\ 0 \\ 0 \end{pmatrix}$$

In the sun rocket system (3) this becomes

$$\hat{U}_{SS} = \begin{bmatrix} \cos\psi(\cos\xi\cos\phi - \sin\xi\cos\alpha\sin\phi) - \sin\psi\{\cos\mu(\sin\xi\cos\phi + \cos\xi\cos\alpha\sin\phi) \\ - \sin\mu\sin\alpha\sin\phi\} \\ \sin\psi(\cos\xi\cos\phi - \sin\xi\cos\alpha\sin\phi) + \cos\psi\{\cos\mu(\sin\xi\cos\phi + \cos\xi\cos\alpha\sin\phi) \\ - \sin\mu\sin\alpha\sin\phi\} \\ \sin\mu(\sin\xi\cos\phi + \cos\xi\cos\alpha\sin\phi) + \cos\mu\sin\alpha\sin\phi \end{bmatrix}$$

The Z-component of  $\hat{U}_{SS}$  was a maximum when the sun direction crossed the lock direction of the sunsensor. The sunsensor sees the sun when

$$\frac{dU_{SS,t}}{dt} = 0 \quad (3.6)$$

Solving for  $\phi_0$  we find

$$\phi_0 = -\omega t + \tan^{-1} \left\{ \frac{\tan\mu\cos(\Omega t + \xi_0)(\Omega + \omega\cos\alpha) + \omega\sin\alpha}{\tan\mu\sin(\Omega t + \xi_0)(\omega + \Omega\cos\alpha)} \right\} \quad (3.7)$$

The numerous values of  $t$  were then substituted in to equation (3.7) determining a set of values of  $\phi_0$  which were in turn averaged to determine the final value of  $\phi_0$ . As it happened no single value of  $\phi_0$  determined by equation (3.7) differed from  $\phi_0$  by more than  $.005^\circ$ .

Figure 3.6 shows to what extent the rocket aspect is determined by the angles so far determined. The rocket axis moves on the surface of a cone. The axis of the cone is titled at an angle  $\alpha$  with respect to the  $Z_S$ -axis. The angle  $\psi$ , which is the last unknown angle, is the azimuth of the cone in the  $X_S - Y_S$  plane.

As the angle  $\alpha$  fixes the angle that  $L$  makes with the  $X_S - Y_S$  plane, we see from Figure 3.6 that the angle  $\delta$  between  $L$  and  $B$  is fixed once  $\psi$  is determined. The angle  $\delta$  was to be determined directly from the magnetometer data. Since the magnetometer failed we resorted to using the particle data itself to fix the value of  $\psi$  which in turn fixed  $\delta$ .

To elucidate, in Figure 4.1 we show the count rates of several

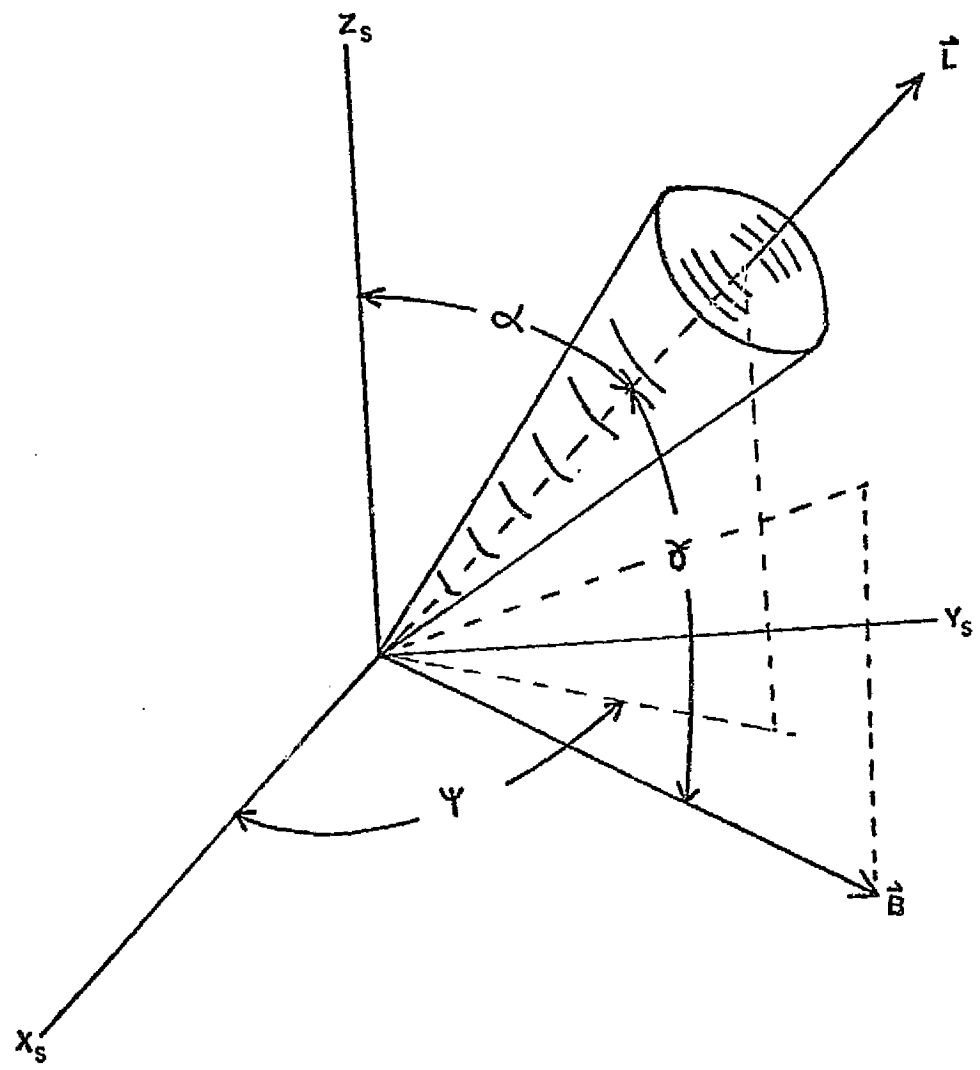


Figure 3.6. Precession cone of the rocket determined in the sun system. The angle  $\psi$  remained to be determined from the particle data.

channels of the  $45^\circ$ ,  $90^\circ$  and  $135^\circ$  detectors. The  $135^\circ$  detector was to look mainly down the field line, the  $90^\circ$  detector was to look mainly perpendicular to the field line and the  $45^\circ$  detector was to look mainly up the field line. Since it is generally expected that the majority of particles are coming down the field in a precipitation event it is consistent that the  $45^\circ$  detector always had a higher count rate than the  $135^\circ$  detector. The  $90^\circ$  detector which crossed over from up looking to down looking therefore showed a great variation over a single roll. Of the three data sets, that of the  $135^\circ$  detector had the best defined maximum which appeared as a narrow peak once per roll. From the preceding considerations we have made the assumption that this maximum on the average corresponds to the lowest pitch angle viewed by the detector in its periodic sweep. Using all of the constants previously determined we calculated the angle between the magnetic field and the detector look direction. (This is the complement of the particle pitch angles) as a function of  $\psi$  for all times of the flight of the rocket during free fall. For the correct choice of  $\psi$  the peaks of the data set from the  $135^\circ$  detector should lie on the peaks of the look direction angle and the valleys on the valleys. Because of the vagaries of counting statistics and the time resolution of .00853 second the peaks of the data vary from perfect symmetry and exact roll position. To overcome this we calculated the cross-correlation of the angle with the data at 0 sec lag for various values of  $\psi$ . This function is shown in Figure 3.7. We chose the value of  $\psi$  at the peak of this curve as the best fit value and the half width at half maximum as the uncertainty.

In table 3.3 we list the final values for all the determined constants.



Table 3.3

$$\psi = 1.1^\circ \pm .5^\circ$$

$$\xi_0 = -1.65^\circ \pm .10^\circ$$

$$\phi_0 = 231.13 \pm .03^\circ$$

$$\mu = 78.21^\circ \pm 2^\circ$$

$$\alpha = 6.049^\circ \pm .5^\circ$$

$$\delta = 118.9^\circ \pm 1.0^\circ$$

$$w = 1943 \pm 16^\circ/\text{sec}$$

$$\Omega = 8.287 \pm .035^\circ/\text{sec}$$

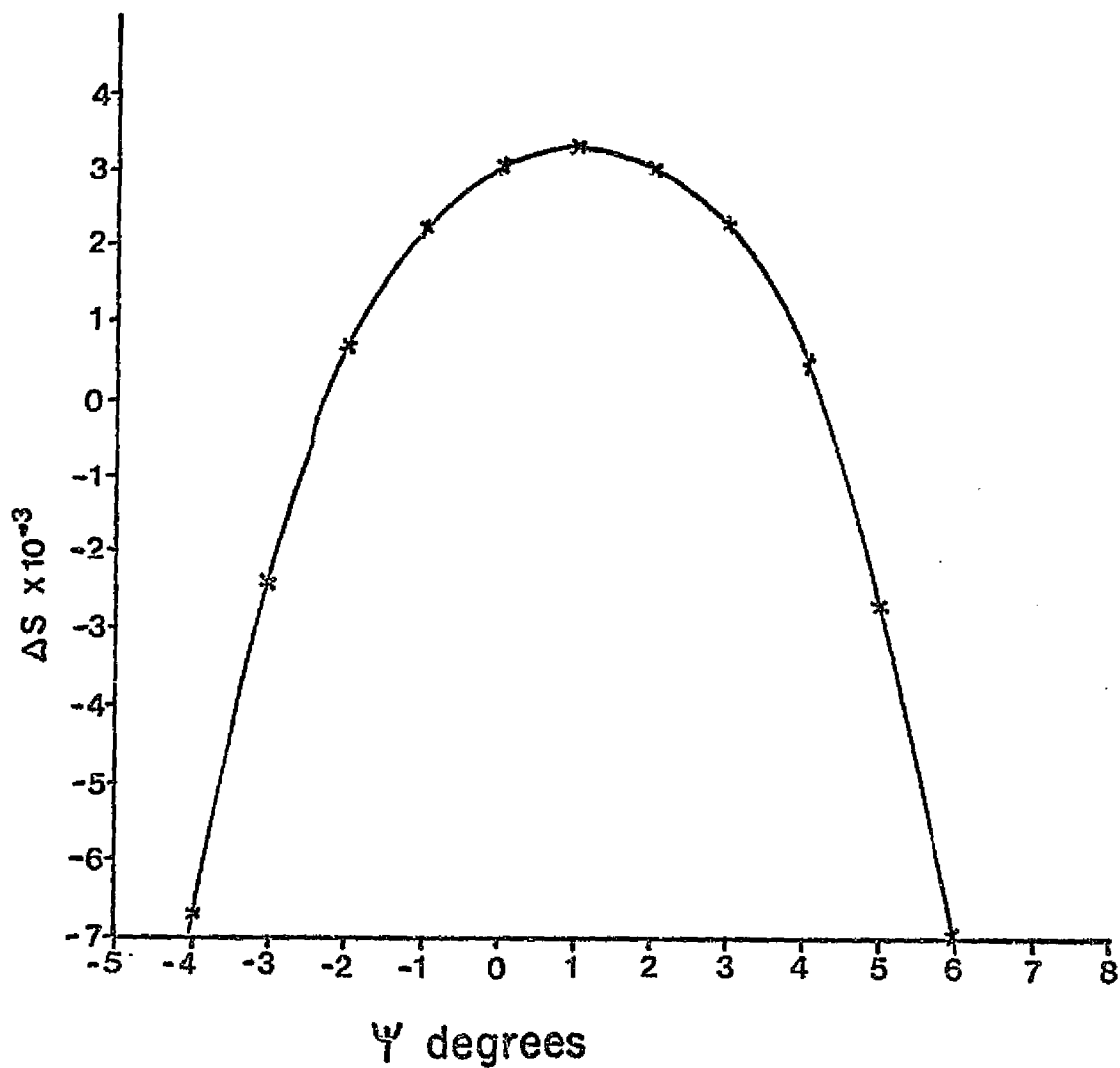


Figure 3.7. Cross-correlation of the compliment of the pitch angle and the count rate for the 135 degree detector. The angle  $\psi$  is shown in figure 2.6. An arbitrary constant was subtracted from the actual value of  $S(\psi)$  to enhance the variation for plotting.

## CHAPTER IV

### DATA REDUCTION AND EXPERIMENTAL RESULT

#### IV.A. Data Overview

The data in the nine channels of each of the three spectrometers was recorded simultaneously over a .00853 second collection period. Figure 4.1 is a display of the output of several channels of the three detectors over a few seconds of the flight. This is simply a display of the unprocessed count rates.

Several pieces of information are immediately extractable from these figures without any detailed analysis. The strong periodicity that is so evident for the  $90^\circ$  and  $135^\circ$  detectors is at the roll rate of the rocket, 5.4 rev/second. This indicates a strong spatial dependence in the flux of precipitating particles. There is also a distinct mirror symmetry about the peaks. Since the detectors sweep by the same pitch angle twice per roll (going first from high pitch angle to low pitch and then from low pitch angle to high pitch angle) this is an indication that the spatial structure is basically a pitch angle structure. In this particular sample the roll rate is not very evident for the  $45^\circ$  detector. Since it too sweeps out a range of pitch angles this is an indication of pitch angle isotropy over the downward hemisphere. There are some periods when a weak roll dependence is evident which is the return to anisotropy. There are also apparent periodicities in the amplitude envelope of all six channels shown in Figure 4.1. We will examine these periodicities in greater detail later.

The number of counts in each channel as was indicated in Chapter I is a measure of the energy spectra. No channel at any time experienced

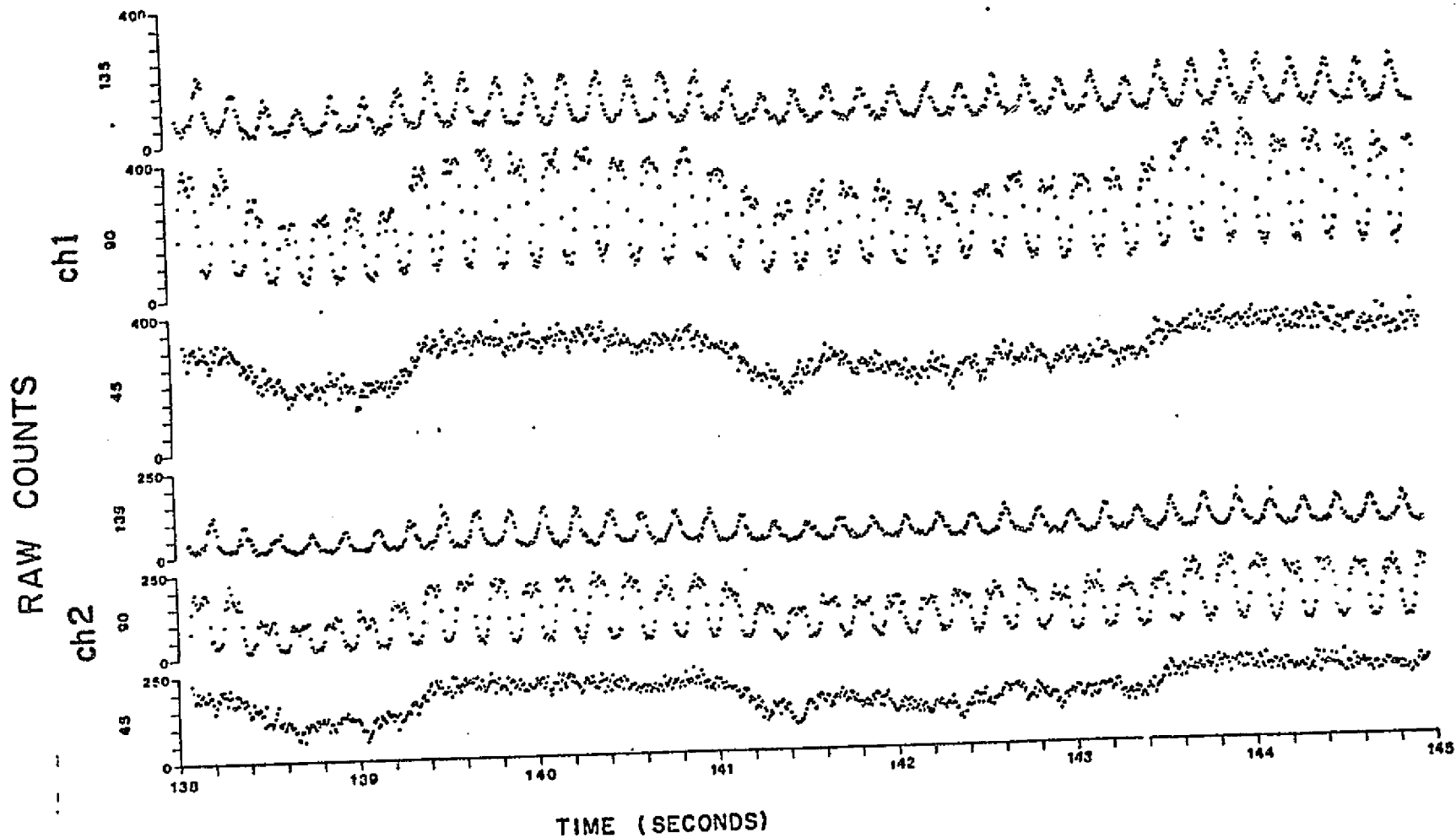


FIGURE 41. UNPROCESSED COUNT RATES FOR SEVERAL CHANNELS AND DETECTORS.

overflow. In fact count rates only exceeded one-half of the maximum in channel one during the most intense periods of the flight. The spectra fell off quite steeply from channel 1. The count rates in channels 6, 7, 8 and 9 rarely exceeded 10 counts per accumulation period although they had considerably more counts at times than the sample spectra for the softer cases in table 1.1 would have lead us to expect. As will be explained, we have excluded the data from channels 8 and 9 from our final result because there are good indications that they are contaminated with proton counts.

From preliminary examination of the data we obtained some idea of the direction that our initial analysis should take. There is strong time dependent pitch angle structure as well as time dependent energy structure. The resolution of spatial dependence from time dependence can not be accomplished unambiguously on a moving rocket. The best one can hope to do is set some limit on the size of the spatial features and ask if they are likely.

The basic data collection period of .00853 seconds corresponds to a spatial distance determined from the rocket horizontal velocity. At the top of its trajectory the rocket had a horizontal velocity of .48 km/sec. The basic distance then is determined to be about 4.1 meters. One might argue that the Larmor radius is a minimal coherence distance for particles in a magnetic field. 4.1 meters is the Larmor radius of an electron with an energy of about 1 Kev. For energies less than this, spatial features on the order of a Larmor radius are unresolved while for energies greater than this such features appear as time variations in the flux. As we will see the apparent time structure of the low energy electrons (about 50 Kev) and the high energy electrons (above 600 Kev) is very closely

parallel. The Larmor radius of a 600 Kev electron is some 4.26 times the Larmor radius of a 50 Kev electron and might be expected to give a larger coherence length for the 600 Kev electron. No such difference is apparent in the data. Though hardly a conclusive argument, this reasoning does take us a bit along the way to accepting the apparent time variation in the flux as not arising from spatial structure.

#### IV.B. The REP And The PCA

The REP of 31 May 1972 began at 6:30 UT as observed by the riometer in Andenes. The riometer record is shown in Figure 4.2 (Matthews and Simons, 1973). 1.0 db of this absorption was due to a solar proton event which had begun on 28 May 1972.

To provide additional criteria for the launching of the rocket we were manning the partial reflection facility of the Auroral Observatory at Tromso. This experiment provided real time indication of the height of ionization in the D-region. We required that there be significant ionization below 75 km before we would accept an absorption event as an REP. At 6:30 UT there was a marked hardening in the precipitation as evidenced by a sudden increase in the absorption of the reflected signal from 65 kilometers altitude. This absorption persisted for some five minutes, disappeared and then reappeared six minutes later at approximately 6:14 UT. The absorption below 65 km then continued until 6:30 UT. The rocket was launched at 06:19 UT and reached apogee at 06:22 UT. From the riometer data (Figure 4.2) it can be seen that the absorption had already begun to decrease during this period. The returns from the partial reflection experiment indicated however, that the detectors were taking data during the time of the most sustained hard precipitation.

As explained in the introduction it seemed quite unlikely that protons were the primary cause of absorption during REP's but it was considered essential to include a proton experiment among the complement of experiments to be carried aboard the rocket F-34. The proton experiment was designed at Bell Telephone Laboratories and built at the University of Maryland. By the use of coincidence logic between two solid state detectors and a magnetic field across the entrance aperture

C. 2

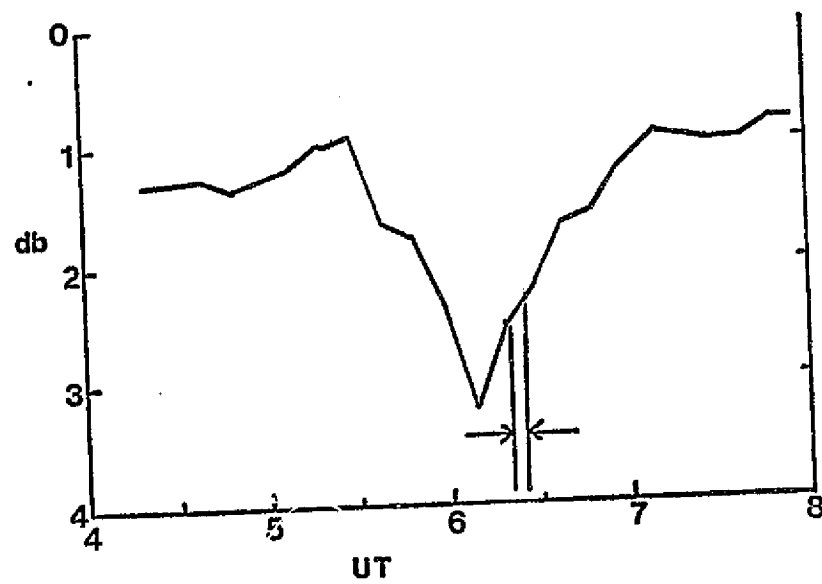


Figure 4.2. Riometer record taken from Matthews and Simons (1973).



the proton detector excluded all electrons from being counted (private communication L. Lanzerotti, 1972). This allowed us to design our electron detector without providing for exclusion of protons.

Before it was possible to determine the actual electron fluxes, it was necessary to determine the extent of possible proton contamination of the data. The PCA proton fluxes are shown in Figure 4.3. These measurements are taken from several sources. Three energy points are from the Bell Telephone Laboratory proton experiment on the explorer 41 (Exp-41) satellite (private communication L. Lanzerotti, 1973) which was located at about  $18R_E$  in the noon sector. Also shown in Figure 4.3 are two points taken from the BTL-proton experiment on F-34. We show in addition the average flux calculated from channel 8 of our electron detector assuming the counts were all due to protons.

The equivalent energy thresholds for protons detected in the electron spectrometer were quite different from the thresholds for electrons (see section I-F). We show the equivalent thresholds for channels one through nine in table 1.6. The proton fluxes are insignificant when compared to the electron fluxes for channels one through six. The average flux of electrons in channel 7 determined for the entire flight is possibly contaminated by as much as 15%. We have determined this value by extrapolating between the points from the proton experiments shown in Figure 4.3. It is obvious from Figure 4.3 that all of the counts in channel 8 and 9 may be accounted for by the protons, though an extrapolation between the Exp-41 points indicates that about 70% of the counts in channel 8 are attributable to electrons. In table 4.1 are shown the predicted average count rates in channel 7, 8 and 9 based upon Explorer 41 satellite data (L. Lanzerotti, private communication) Compared to these are the

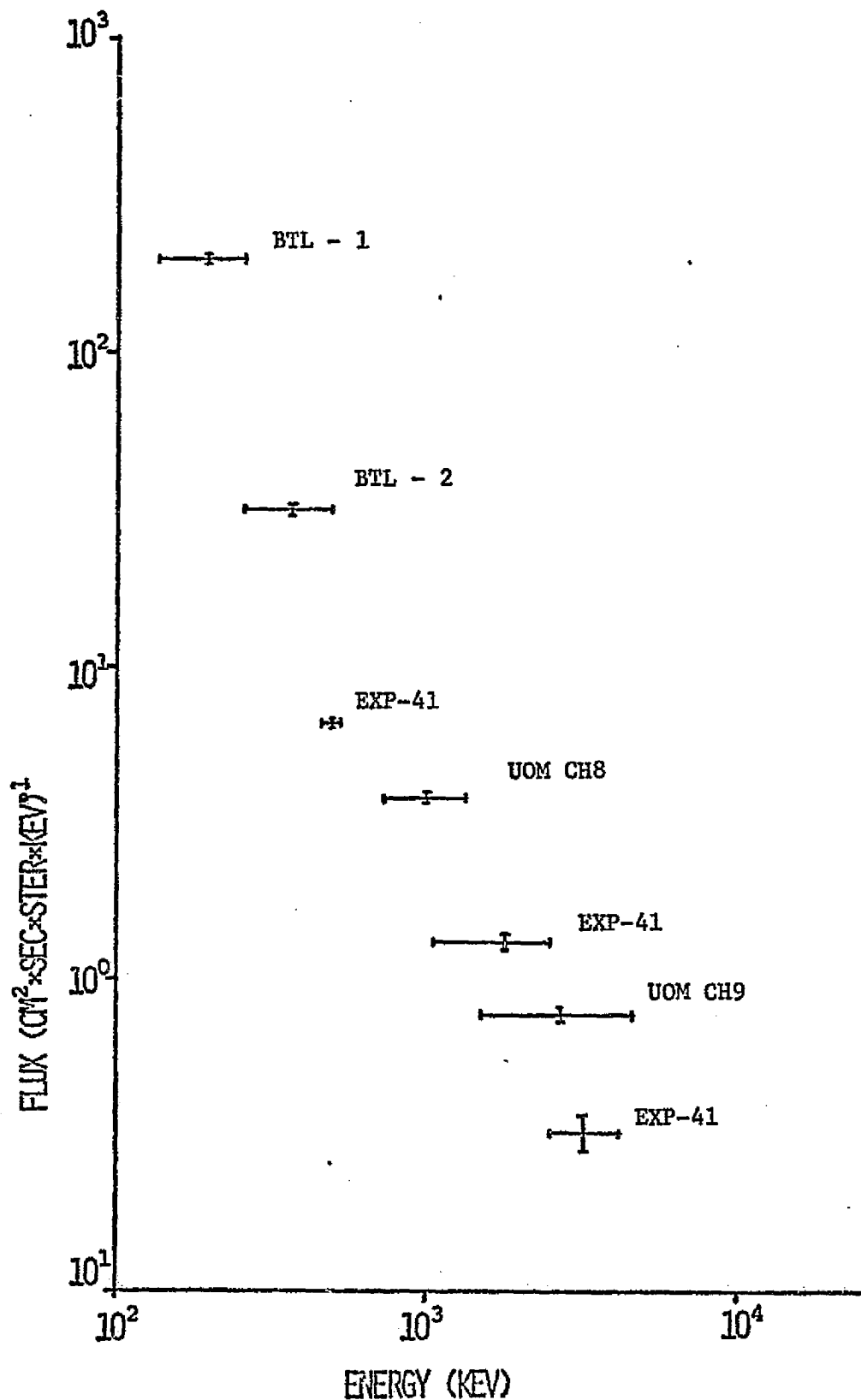


Figure 4.3. Proton fluxes due to Polar Cap Absorption as determined from several sources. BTL-Bell Telephone Laboratory proton experiment on F-34, EXP-41-Bell Telephone Laboratory proton detector on satellite Explorer 41, UOM-University of Maryland electron experiment of F-34.

actual count rates. The conclusions have been drawn above.

Table 4.1

Count rates from Protons compared to actual count rates

	<u>From Exp-41 data</u>	<u>actual count rates</u>	<u>% proton contamination</u>
CH7	.095/period	.268/period	16.8
CH8	.0661/period	.091/period	72.5
CH9	.074/period	.060/period	100.0

#### IV.C. Removing The Roll Dependence.

The time structure so obvious in the raw data indicated that unfolding the roll dependence was a reasonable first step. As the detector sampled the complete pitch angle distribution twice for each roll of the rocket we decided to take one roll as the basic data period assuring two passes at each pitch angle. If the time variation in the flux is slower than the roll rate then our averages are well representative of the actual time structure in the pitch angle. If the time variations in the flux are greater than the roll rate then the results are a frequency filtered component of the true time variation. We will examine this point more fully in section 4.F.

As the detector swept through various pitch angles during a data collection period the central look direction vector of the collimator,  $V_{ID}$ , pointed to different pitch angle as a function of time. The curve of small dots in Figure 4.4 shows the pitch angles covered by the vector  $V_{ID}$  for each of the three detectors. In this curve three dots delineate each data collection period; one for the initial pitch angle, one for the pitch angle half way through the collection period and one for the final pitch angle. A careful examination of the figure shows that the points are not equally spaced in pitch angle. This unequal spacing indicates that the width of the pitch angle field of view is different for different data collection periods and this width is a function of position along these curves. It can also be determined from Figure 4.4 that although the detectors never looked at the same pitch angle simultaneously they did none-the-less have overlapping pitch angle coverage.

During a single sampling period particles enter the collimator from all pitch angles within the field of view. Each pitch angle contributes

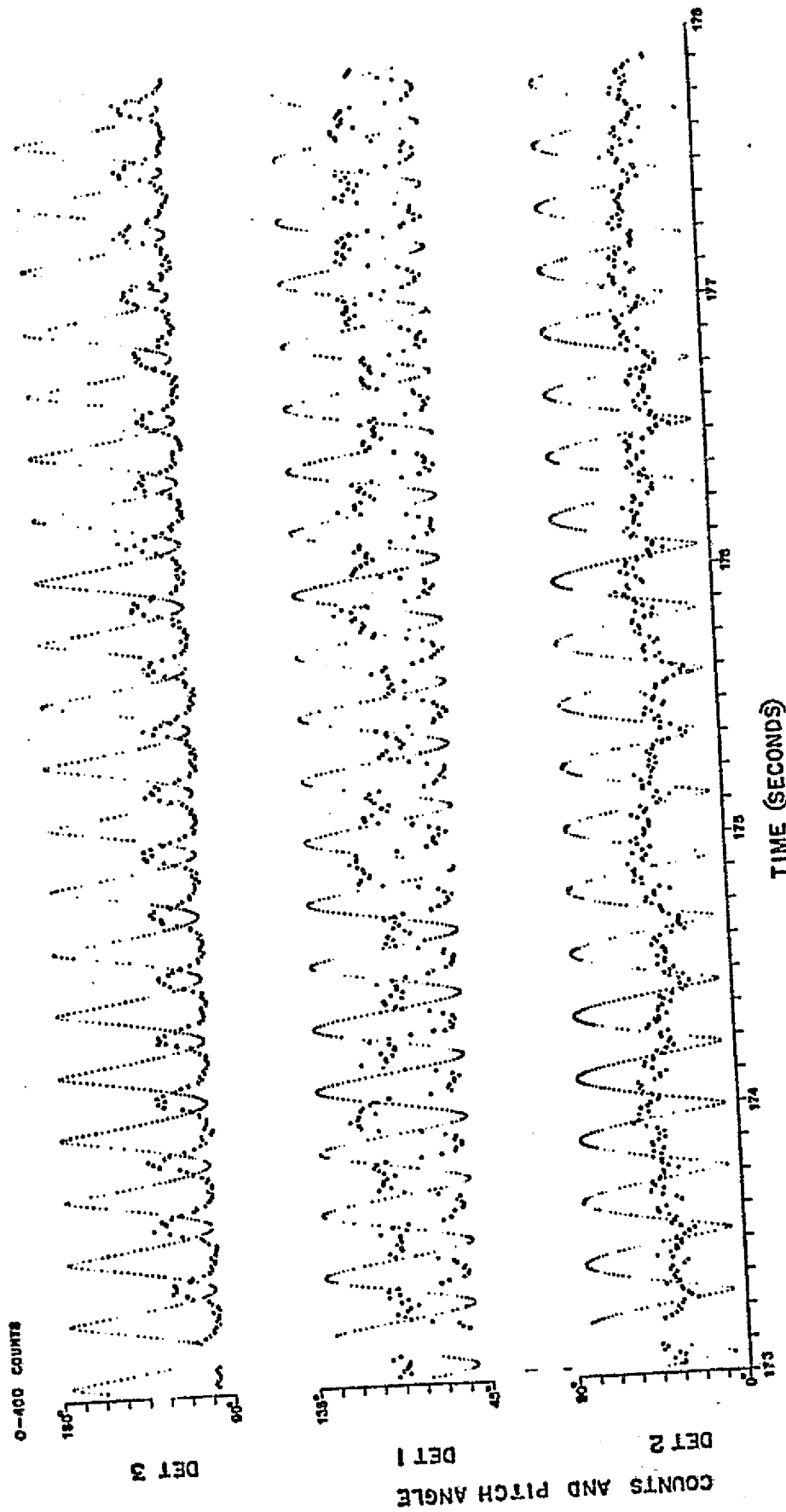


Figure 4.4. The central pitch angle of precipitating particles (small dots) and count rates (large dots) in channel 1 for each detector.

flux in proportion to the area exposed to it and the length of time the area is exposed. If we let  $F$  be the total flux of particles that enters the detector during a period  $\Delta t$  then

$$F = \int_t^{t+\Delta t} \int_{\alpha} [G(\alpha, t) J(\alpha, t)] d\alpha dt \quad (4.1)$$

where  $G(\alpha, t)$  is a geometrical term determining the pitch angle weighting or response of the detector at time  $t$ .  $J(\alpha, t)$  is the integral flux at pitch angle  $\alpha$  and time  $t$ . In terms of the geometrical quantities defined in Figure 4.5 we may also write

$$F = \int_t^{t+\Delta t} \int_{\phi_1} \int_{\phi_2} \int_{r_1} \int_{r_2} \frac{\cos^2 \gamma}{D^2} J(\alpha, t) r_1 r_2 dr_1 dr_2 d\phi_1 d\phi_2 dt \quad (4.2)$$

with  $D^2 = r_1^2 + r_2^2 - 2r_1 r_2 \cos(\phi_1 - \phi_2) + h^2$  and  $\cos \gamma = h/D$ . The vector  $V_p$  passes through the differential areas  $\hat{\sigma}_1$  and  $\hat{\sigma}_2$  making an angle  $\alpha$  with  $B$ , the magnetic field. The angle  $\gamma$  is the angle between the magnetic field and the look direction vector,  $V_{LD}$ , of the collimator. As should be obvious from equation (4.2) and the considerations of Appendix A-4 the pitch angle response discussed here is not the same function as the angular response of the collimator discussed in section I-D and is in fact a more complex function.

By taking the dot product of  $V_p$  and  $B$  we can obtain a relation between the pitch angle  $\alpha$  and the variables of integration in equation 4.2.

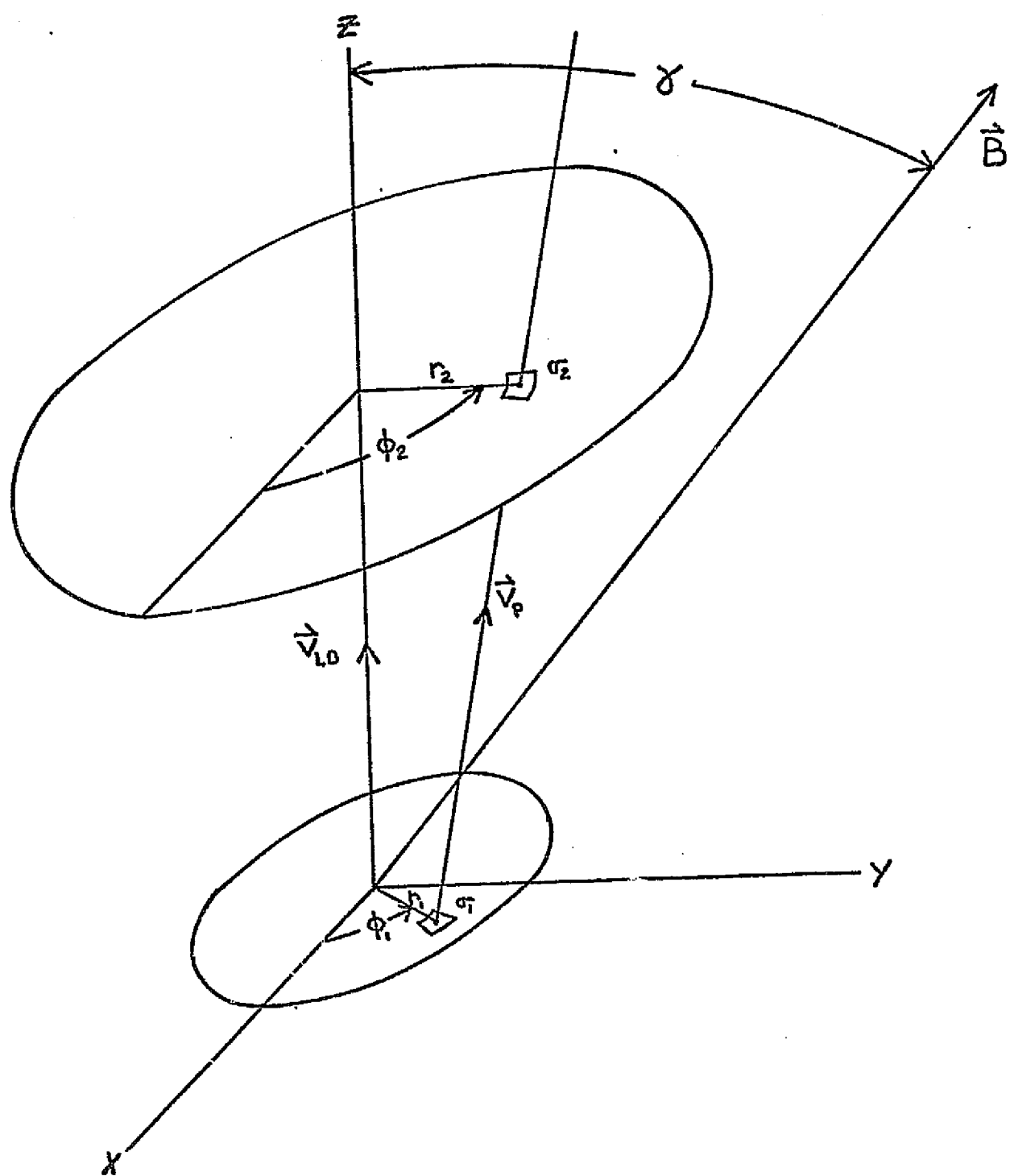


Figure 4.5. Geometrical quantities defining the pitch angle field of view.

$$(r_1 \sin \phi_1 - r_2 \sin \phi_2) \sin \gamma + h \cos \gamma = D \cos \alpha \quad (4.4)$$

This equation may be used to replace one of the four variables  $r_1$ ,  $r_2$ ,  $\phi_1$ , or  $\phi_2$  in equation 4.2 with  $\alpha$  so that  $\alpha$  becomes a variable of integration as in equation 4.1. Making this substitution we obtain the result

$$F = \int_t^{t+\Delta t} \left[ \int_{\alpha} \int_{\gamma} \int_{\phi_1} \int_{\phi_2} \frac{\cos^2 \gamma}{D^2} r_1 r_2 \frac{\partial \gamma_1}{\partial \alpha} d\gamma_2 d\phi_1 d\phi_2 \right] d\alpha dt \quad (4.5)$$

where we may immediately identify the function  $G(\alpha, t)$  as

$$G(\alpha, t) = \int_{r_2} \int_{\phi_1} \int_{\phi_2} \frac{\cos^2 \gamma}{D^2} r_1 r_2 \frac{\partial \gamma_1}{\partial \alpha} dr_2 d\phi_1 d\phi_2 \quad (4.6)$$

With the time dependence entering through the function

$$r_1 = r_1(\alpha, \gamma(t), r_2, \phi_1, \phi_2) \quad (4.7)$$

For any given data acquisition period we may determine  $G(\alpha, t)$  by numerically integrating equation 4.6 for a fixed value of  $\alpha$  and  $\gamma$ . We have instead determined the function  $G(\alpha, \bar{\gamma})$ , (the time averaged value of  $G(\alpha, t)$  over the counting period), which we will refer to as the pitch angle response function.  $G(\alpha, \bar{\gamma})$  is given by

$$G(\alpha, \bar{\gamma}) = \frac{1}{\Delta t} \int_t^{t+\Delta t} G(\alpha, t) dt \quad (4.8)$$



which we associated with the value  $\bar{\gamma}$  given by

$$\bar{\gamma} = \frac{1}{\Delta t} \int_t^{t+\Delta t} \gamma(+) dt \quad (4.9)$$

In Figure 4.6 we display  $G(\alpha, \bar{\gamma})$  for several values of  $\bar{\gamma}$ . As we used  $G(\alpha, \bar{\gamma})$  as a weighting function over each counting period it was always normalized so that it had a maximum value of one for each period.

With the pitch angle response function,  $G(\alpha, \bar{\gamma})$ , the pitch angle dependence was unfolded from the data for each of the three detectors. Since this involves taking data from approximately 22 consecutive data points the result at best represents a time average over 0.185 seconds and a pitch angle smoothing over 15 degree intervals.

The measured flux in any collection interval,  $i$ , which is given in terms of the number of counts,  $N_i$ , the geometrical factor,  $G$ , the collection time  $\Delta t$  and the efficiency  $E$  by the relation

$$F_i = \frac{N_i}{G \Delta t E} \quad (4.10)$$

is assumed to first order to come from all directions in the acceptance view of the collimator. As a statistical weight for the flux at pitch angle  $\alpha$ , we took the pitch angle response at  $\alpha$ ,  $G(\alpha, \bar{\gamma})$ . The average flux at a given pitch angle during one roll is given by the expression

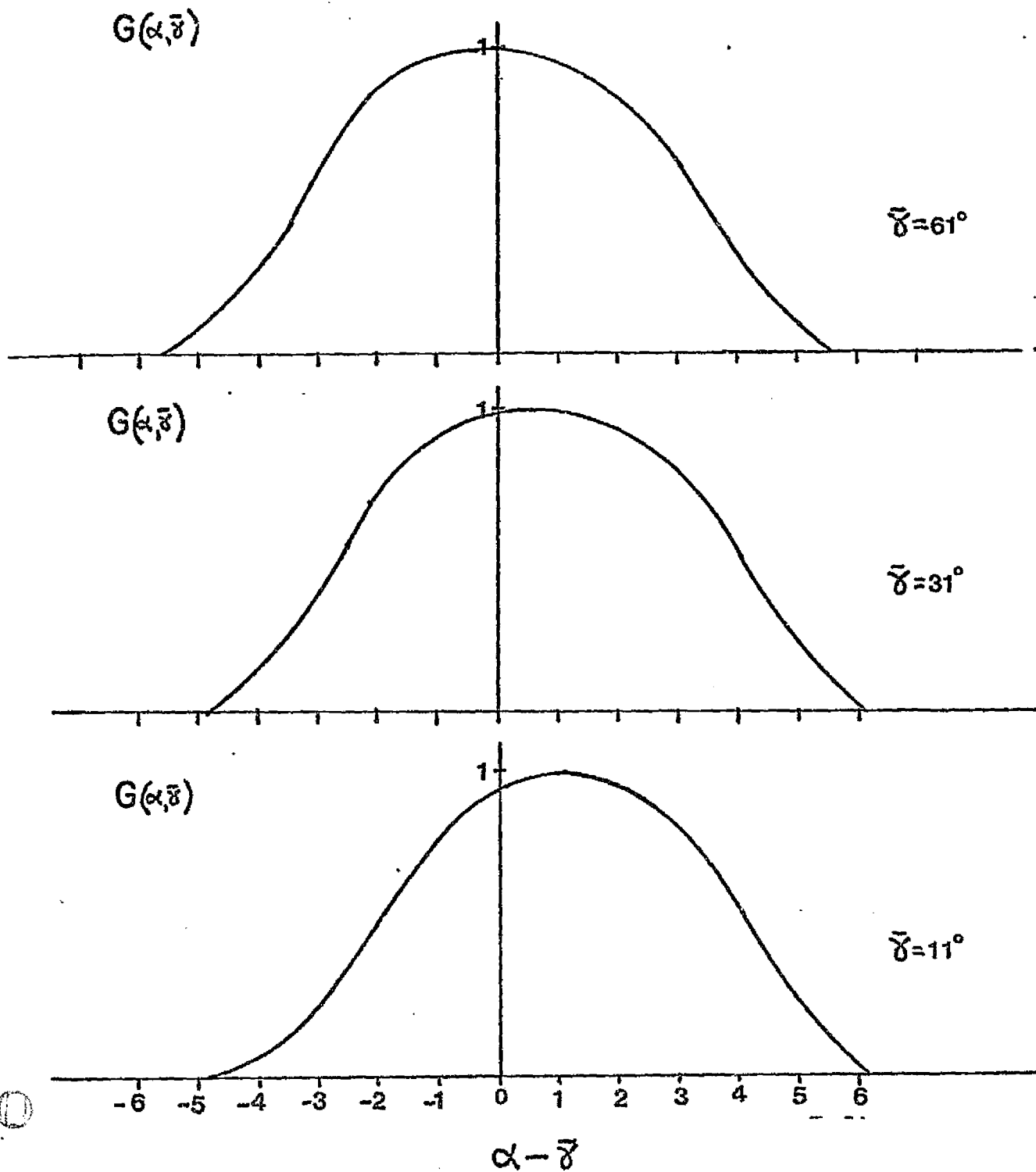


Figure 4.6. The pitch angle response function for several values of  $\bar{\gamma}$ , the average angle between the collimator axis and the magnetic field.

$$J(\alpha) = \frac{\sum_{i=1}^{22} F_i G(\alpha, \bar{\gamma}_i)}{\sum_{i=1}^{22} G(\alpha, \bar{\gamma}_i)} \quad (4.11)$$

It follows that the uncertainty  $\sigma_{J(\alpha)}$  is given by

$$\sigma_{J(\alpha)} = \frac{\sqrt{\sum_{i=1}^{22} G^2(\alpha, \bar{\gamma}_i) \left( \frac{N_i}{(Gx\Delta txE)^2} \right)}}{\sum_{i=1}^{22} G(\alpha, \bar{\gamma}_i)} \quad (4.12)$$

We have assumed  $\sigma_{N_i} = \sqrt{N_i}$  and that there is normal propagation of error. For the twenty-two points in a single roll of the rocket,  $G(\alpha, \bar{\gamma}_i)$  is typically zero for a given  $\alpha$  at all but 6 values of  $\bar{\gamma}_i$ . There are therefore only about six terms in each of the above sums for a specific pitch angle  $\alpha$ .

For each channel of each detector we could then produce pitch angle distributions of the type demonstrated by Figure 4.7. There are two data sets shown in each diagram in Figure 4.7. They are for corresponding energy channels for the 45 degree and 90 degree detectors. For much of the precession period of the rocket these detectors had overlapping pitch angle coverage during any one roll of the rocket. The detectors did not look at the same pitch angles simultaneously nor did the corresponding energy channels have the same response functions. We would not therefore expect them to record the same integrated flux at the same pitch angle. This accounts for the apparent inconsistency in the overlapping regions in Figure 4.7. We do expect that the representative energy spectra obtained at the overlapping pitch angles be equal within the limits of

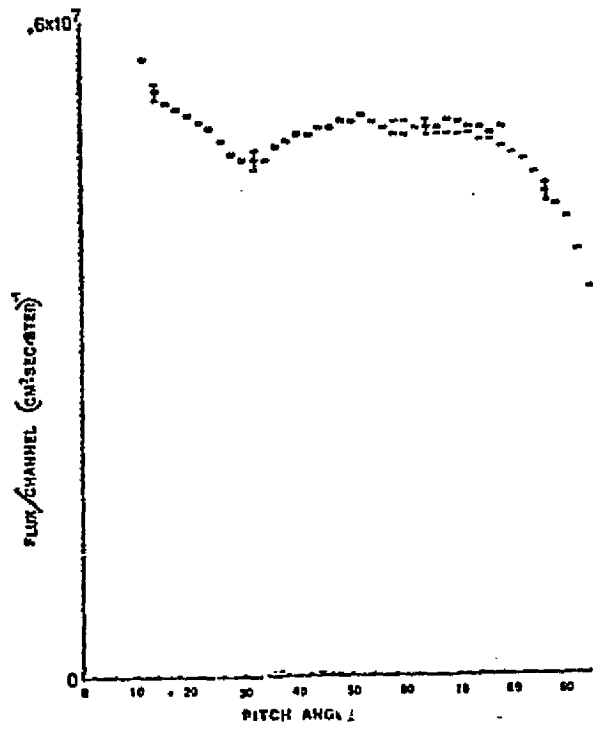
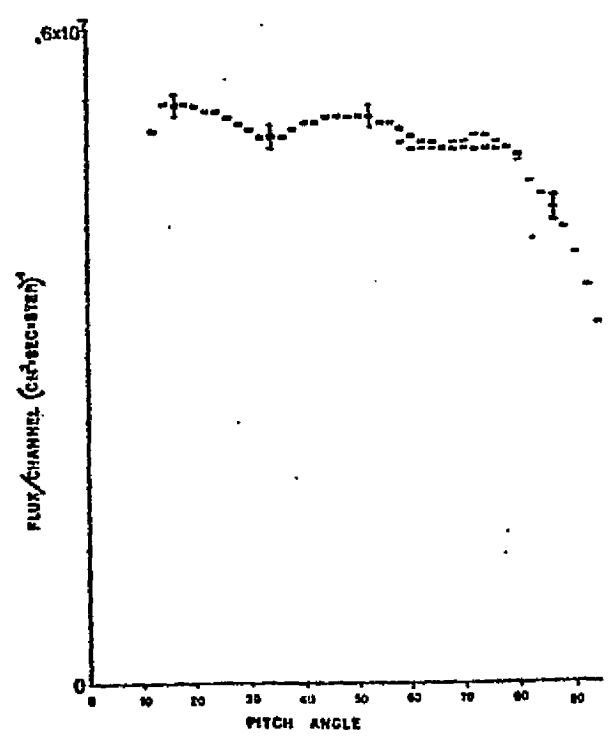
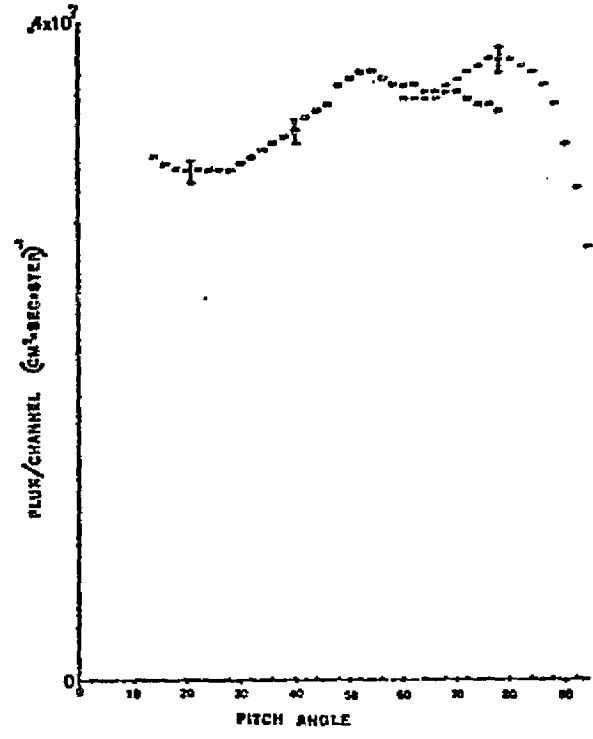
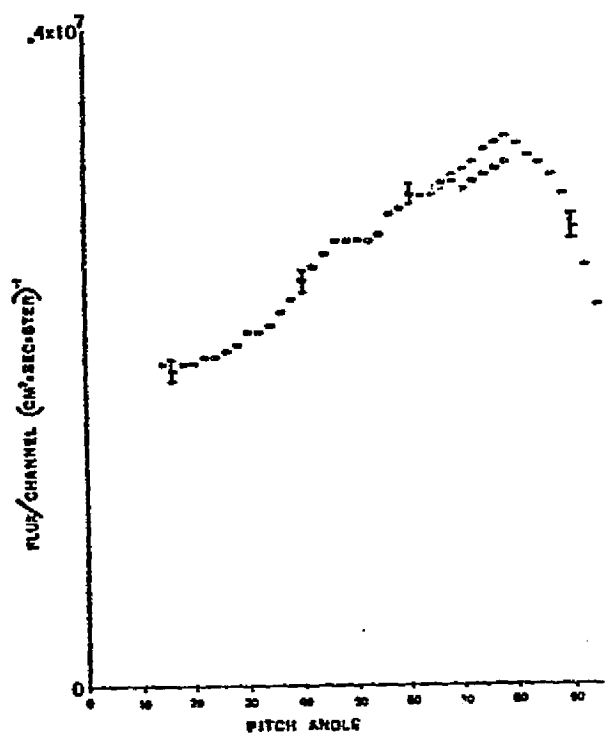


FIGURE 4.7. TYPICAL PITCH ANGLE DISTRIBUTIONS DETERMINED OVER ONE ROLL OF THE ROCKET.

uncertainty. Pitch angle distributions were produced for every roll of the rocket from time 80 seconds to time 300 seconds into the flight. We will discuss these distributions in section 4.E.

The pitch angle distributions enabled us to obtain an overall picture of the intensity variations on the time scale of one roll of the rocket. We defined the average unidirectional flux,  $J_{\mu}$ , over the pitch angles covered by each detector.  $J_{\mu}$  is defined by the relation

$$J_{\mu} = \frac{\int_0^{2\pi} \int_{\alpha_{\min}}^{\alpha_{\max}} J(\alpha) \sin \alpha \, d\alpha d\phi}{\int_0^{2\pi} \int_{\alpha_{\min}}^{\alpha_{\max}} \sin \alpha \, d\alpha d\phi} \quad (4.13)$$

$\alpha_{\min}$  and  $\alpha_{\max}$  are the pitch angle limits of the pitch angle coverage for a given detector.  $J_{\mu}$  has units of  $\text{cm}^{-2} \times \text{sec}^{-1} \times \text{ster}^{-1}$ . Figure 4.8a shows  $J_{\mu}$  for the first half of the flight for two channels of the  $45^{\circ}$  and  $90^{\circ}$  detectors. At 80 seconds the rocket had reached an altitude of 90 km so that even in the lowest energy channel there was little if any atmospheric energy degradation of the particles reaching the detector. A 40 keV electron will penetrate to about 87 km leaving most of its energy in the last 4 or 5 kilometers (Maeda, 1965). The fairly constant flux level for the first 15 seconds of data shown in Figure 4.8a is a feature of the precipitating particles therefore and not an atmospheric effect. At about 107 seconds there is a marked increase in the level of particle flux characterized by a steep increase in the counting rate. This steep increase in the counting rate occurred simultaneously in channels 1 through 7 of all three detectors to within the

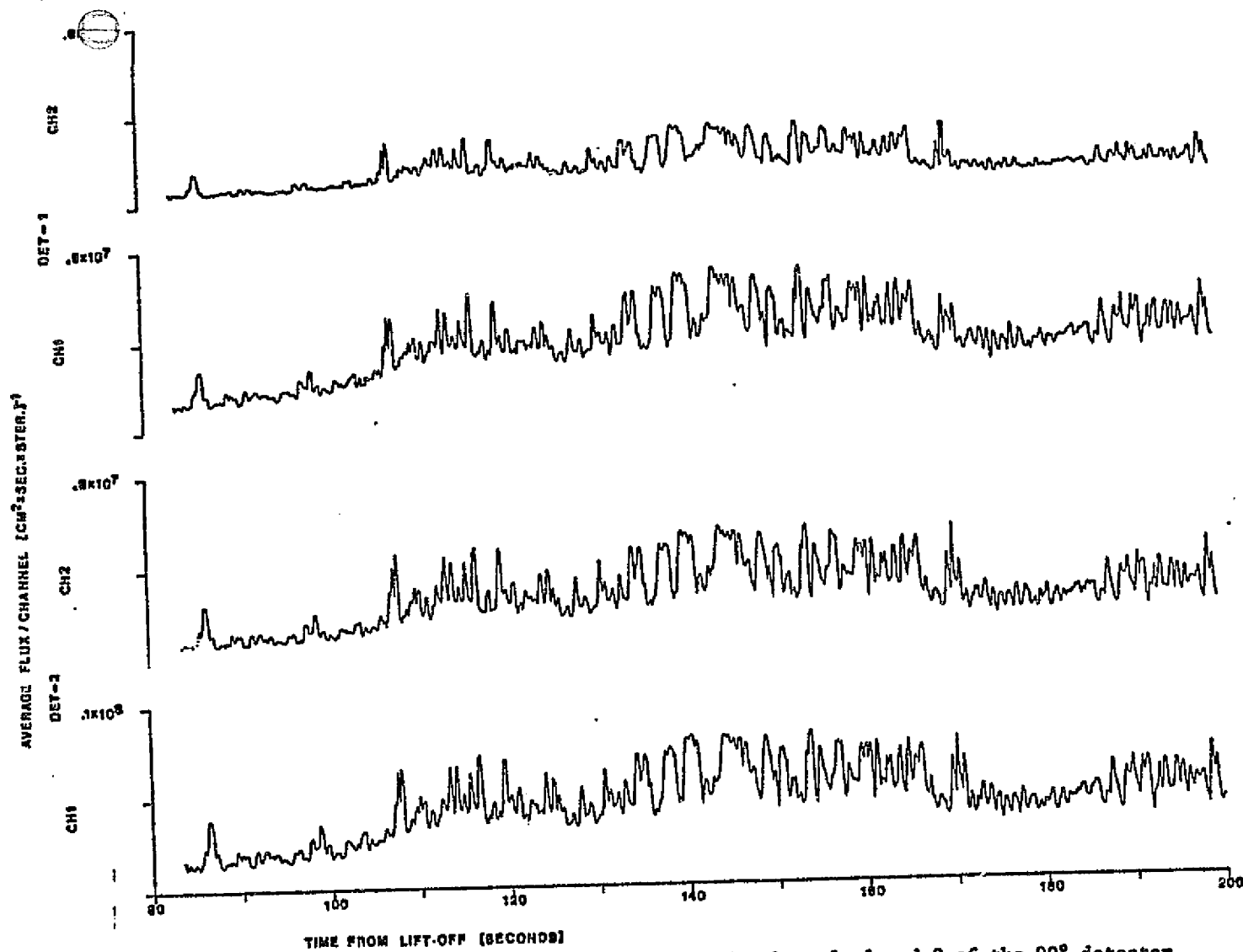


Figure 4.8a. The average unidirectional flux,  $J_u$ , in channels 1 and 2 of the 90° detector (det-1) and the 45° detector (det-2).

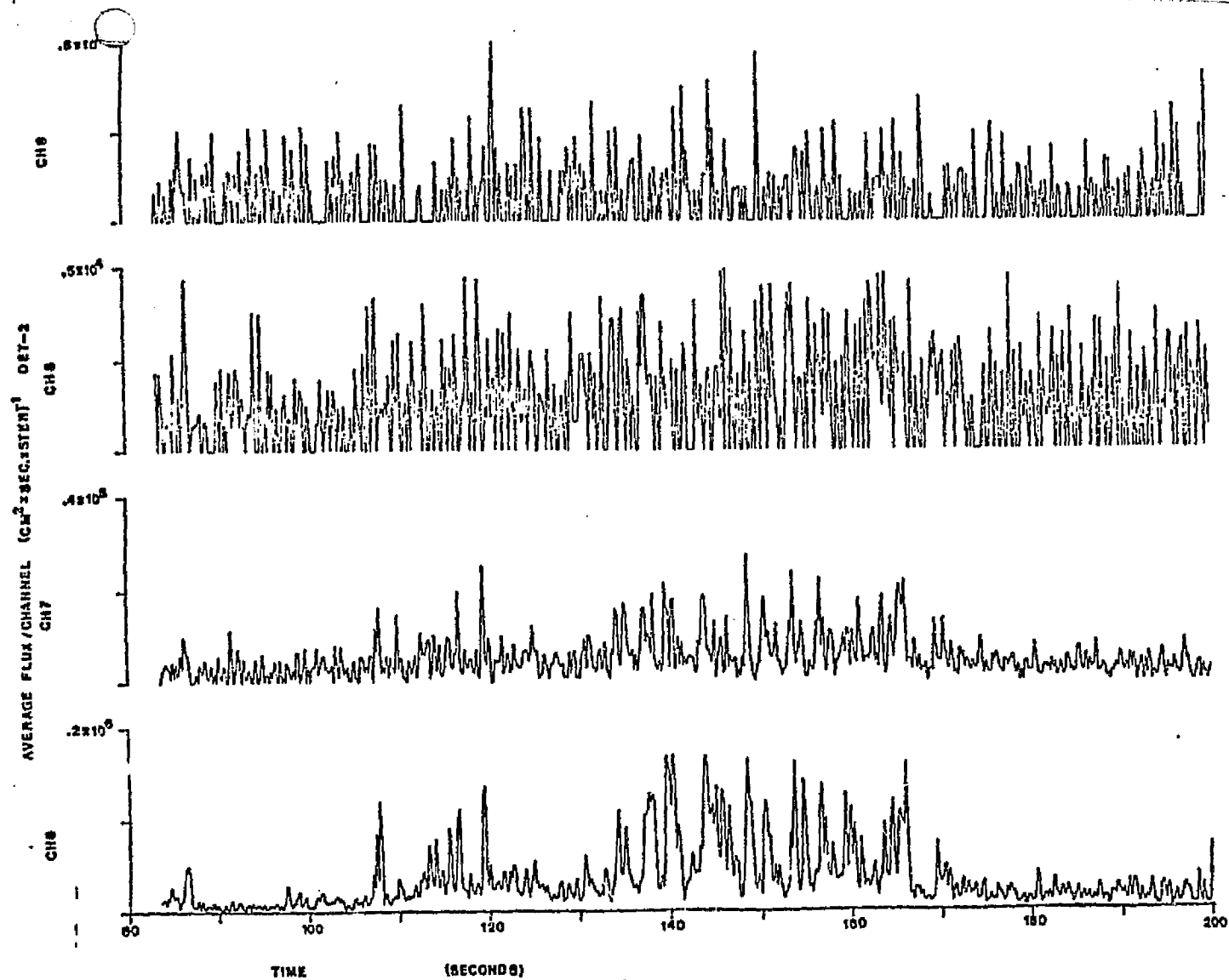


Figure 4.8b. The average unidirectional flux,  $J_{\mu}$ , in channels 6 through 9 of the 45° detector (det-2).

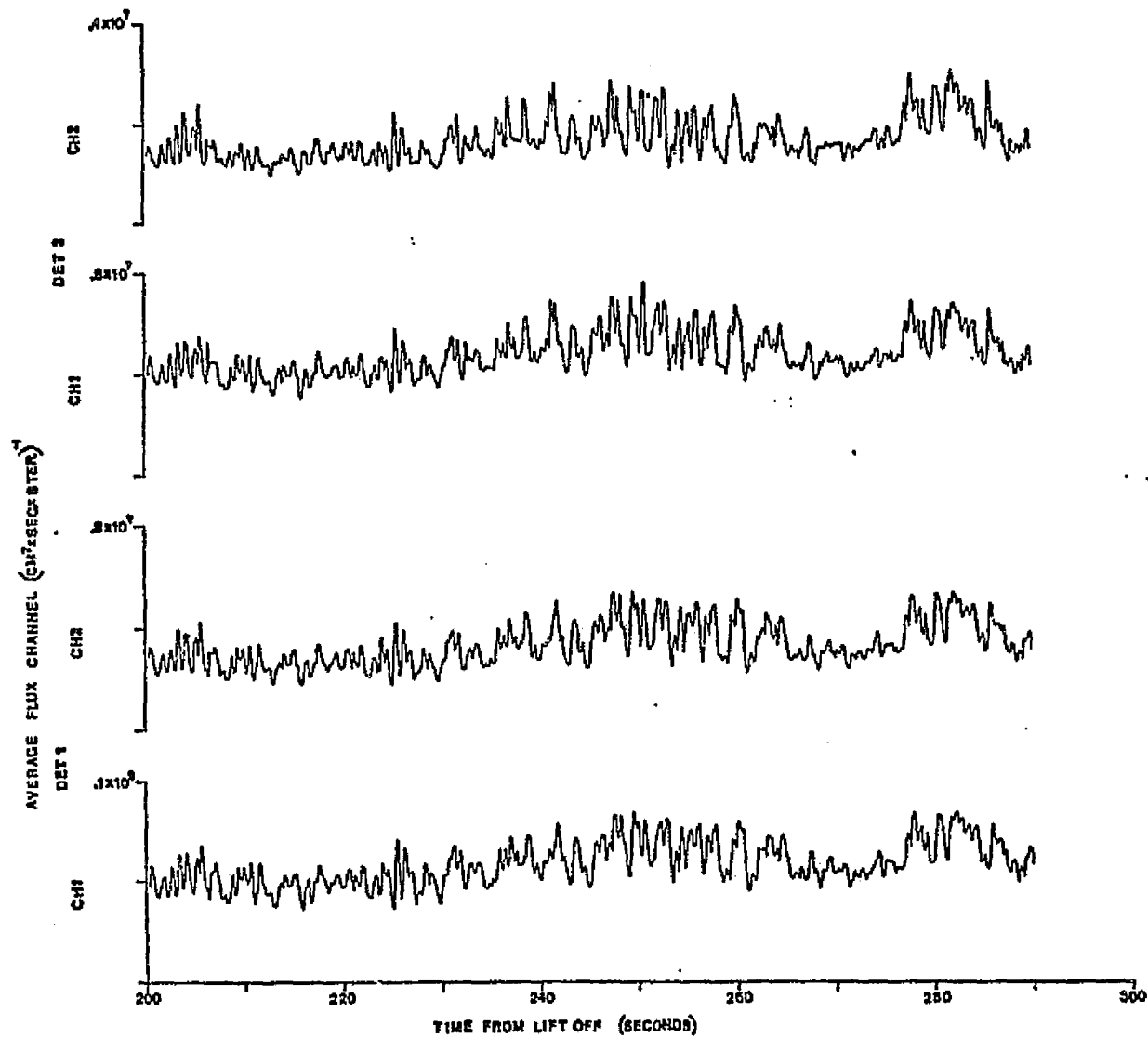


Figure 4. 8c. The average unidirectional flux,  $J_{\mu}$ , in several channels from 200 seconds to 300 seconds.



time resolution of .185 sec (one roll). The fractional increase in flux is much greater in the higher energy channels and can be seen in Figure 4.8b which shows the average unidirectional flux for channels 6 through 9 of the 45° detector. As is somewhat more evident from the higher energy channels there is a decrease in flux at 130 seconds and then another increase continuing until a rather abrupt drop-off at 170 seconds. We refer to these periods as bursts 1 and 2. There is another such burst beginning at about 230 seconds (Fig. 4.8c) continuing to 265 seconds and another from 278 seconds to 288 seconds. We call these bursts 3 and 4. The bursts are characterized by pulsations in intensity over which the flux changes by a factor of two in the lowest energy channel and by as much as ten in channels 6 and 7. Superimposed on the flux for the entire flight are short period pulsations which involve both large and small changes in the flux. We will refer to these as the fine structure. We will return to an analysis of these various features of the time structure in section IV-E and IV-F.

#### IV.D. The Energy Spectra

The broad response functions of the energy analyzers (see Figure 2.16) were capable of distinguishing only large features in the energy spectra. It is the common practice when looking for broad features to attempt to fit exponential spectra (as we discussed in Chapter II), power law or some similar general form that can give parameters that characterize the energy hardness and flux level. Assuming a spectral form,  $F(E)$ , which over any accumulation period is the average unidirectional differential flux over the aperture, the number of counts in the  $i$ th channel of the analyzer is given by

$$N_i = G \cdot \Delta t \cdot x \int_0^{E_{\max}} R_i(E) F(E) dE \quad (4.14)$$

$R_i(E)$  is the response function of the  $i$ th channels, as we have discussed in Chapter II,  $G$  is the geometrical factor, and  $\Delta t$  is the accumulation time. The  $i$ th accumulation will yield a measured count  $N_{im}$ . To fit an analytical form to  $F(E)$  we will define the chi-square parameter

$$\psi^2 = \sum_{i=1}^7 \frac{(N_{im} - N_i)^2}{N_{im}} \quad (4.15)$$

which will permit us to determine a least square fit to the measured data. The uncertainty for  $N_{im}$  will be assumed to be  $\sqrt{N_{im}}$  from Poisson statistics.  $\psi^2$  must be minimized with respect to the constant parameter that define the function  $F(E)$ .

For an exponential spectrum of the type discussed earlier one chooses

$$F(E) = J_1 \exp \{-E/E_0\} \quad (4.16)$$

with  $E$  and  $E_0$  in kev and  $J_1$  in particles/(cm<sup>2</sup> x sec ster kev) .

$\psi^2$  is set to a minimum value by satisfying the conditions

$$\frac{\partial \psi^2}{\partial J_1} = 0 \quad \text{and} \quad \frac{\partial \psi^2}{\partial E_0} = 0 \quad (4.17)$$

The appropriate values of  $J_0$  and  $E_0$  must be determined by numerical iteration because the exponential form does not yield a closed solution for  $E_0$  .

The identical procedure may be followed for a power law spectrum of the form

$$F(E) = J_1 E^{-x} \quad (4.18)$$

Both power law and exponential law fits to the spectra were attempted. They proved generally inadequate in representing the spectrum over the full range of energy. The exponential law was generally better than the power law. In Figure 4.9a, a best fit exponential law is shown by the solid line. The corresponding point spectrum is also shown with the appropriate error bars. We explain a little later how the point spectrum is determined. The exponential law consistently gave too large a flux in the lowest energy channels and too small a flux in the higher energy channels. The power law was generally inadequate across the entire spectrum. A very good fit to the data could always be obtained by

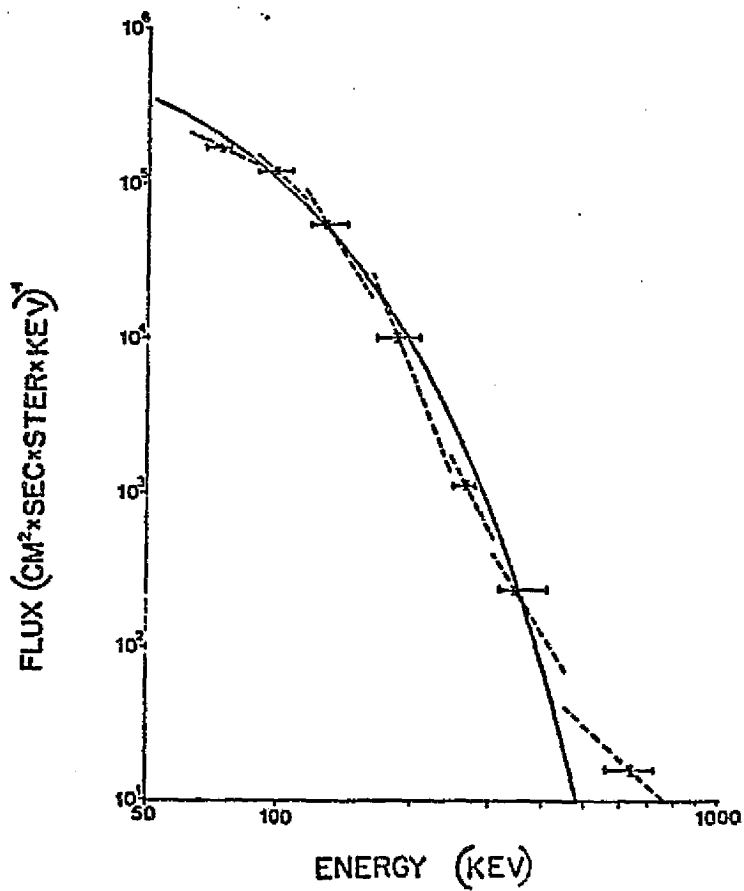
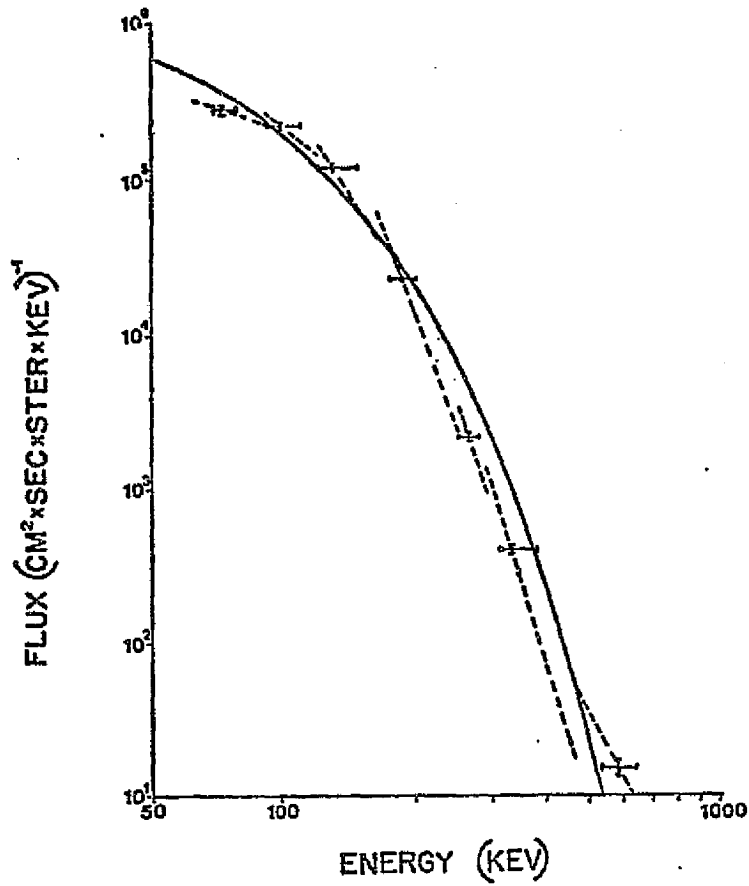


Figure 4.9 a and b. Different representations of the energy spectra.

combining the exponential and power laws into a four parameter fit of the form

$$F(E) = J_1 E^{-x} + J_2 \exp \{-E/E_0\} \quad (4.19)$$

but this complicated the iterative fitting procedures used on the computer to such an extent as to require a prohibitive amount of computational time to process the data from the entire flight. In an attempt to produce a better representation in reasonable computation time we developed an ad-hoc procedure for defining the spectrum which reproduced essentially the same spectrum as the four parameter fit given by equation (4.19). This is the point spectrum shown in Figures 4.9a and b and referred to above. This procedure guaranteed that the spectrum gave the correct count rate in each channel so that the error for the assigned flux was taken from the counting statistics. The error in the energy was taken to be the full width at half maximum of the response function of the channel folded with the resulting spectrum.

We assume that the spectrum in two adjacent channels may be represented by a power law.

$$F = J_1 E^{-x} \quad (4.20)$$

so that the counts in the two consecutive channels are given by

$$N_i = G\Delta t \int_0^{E_{\max}} R_i(E) J_1 E^{-x} dE \quad (4.21)$$

and

$$N_{i+1} = G\Delta t \int_0^{E_{\max}} R_{i+1}(E) J_1 E^{-x} dE \quad (4.22)$$

The ratio of counts

$$\frac{N_i}{N_{i+1}} = \frac{\int_0^{E_{\max}} R_i(E) E^{-x} dE}{\int_0^{E_{\max}} R_{i+1}(E) E^{-x} dE} \quad (4.23)$$

is strictly a function of the hardness and thereby automatically determines  $x$ . Computationally a table of ratios may be determined as a function of  $x$  and the values of  $x$  simply read from the table once the ratio is known.  $J_1$  is determined by

$$J_1 = \frac{N_i}{G\Delta t \int_0^{E_{\max}} R_i(E) E^{-x} dE} \quad (4.24)$$

once  $x$  is known. With the values of  $J_1$  and  $x$  determined, the average energy of a count in channel  $i$  is then given by the relation

$$\bar{E}_i = \frac{\int_0^{E_{\max}} R_i(E) E E^{-x} dE}{\int_0^{E_{\max}} R_i(E) E^{-x} dE} \quad (2.25)$$

The value of the spectrum is evaluated at  $\bar{E}_i$  and the spectral

point then chosen as

$$F_i = J_1 \bar{E}_i^{-x}, \bar{E}_i .$$

Spectra determined in this fashion are displayed in Figures 4.9a and b. The power law determined over each channel is drawn as a dashed line through the points. Figure 4.9b is the average spectra determined from the data over the entire flight.

#### IV.E. Energy And Pitch Angle Structure.

The reduced data from the REP experiment contains a tremendous amount of detail which would probably justify further months or years of labor to more fully elaborate and understand. Several broad features have emerged which we feel may fairly well illuminate the physics of the REP phenomenon.

Figure 4.10 shows a time display of the average integral unidirectional flux of precipitating particles shown in parallel with the average energy of these particles. In order to improve upon the time resolution of the data in Figures 4.8 these averages have been determined over a period of slightly more than one-half roll of the rocket .095 seconds. The time structure which emerges is much the same as that in Figures 4.8. There appears to be two types of precipitation; that during the bursts 1, 2, 3 and 4, and that during the interburst periods. The bursts are made up of short-bursts which have a fine structure superimposed upon them. The interburst periods have the fine structure pulsations which are superimposed on small bursts similar to the substructure of the large bursts. The burst and pulsing behavior in the integral flux is paralleled by a consistent behavior in the pitch angle distributions. In Figure 4.11a we show the pitch angle distribution at the peak of a large burst for several energies. In Figure 4.11b we show the pitch angle distribution at the valley between two pulsation peaks. There is pitch angle isotropy at the peaks and a loss cone anisotropy at the valleys. The loss cone is more pronounced for the higher energy particles. The consistency of this behavior is demonstrated by the time plots of pitch angle for the precipitating particles shown in Figures 4.12a, b, c, and d. The Figures 4.12 are for channels 3 and 4 of the 45-



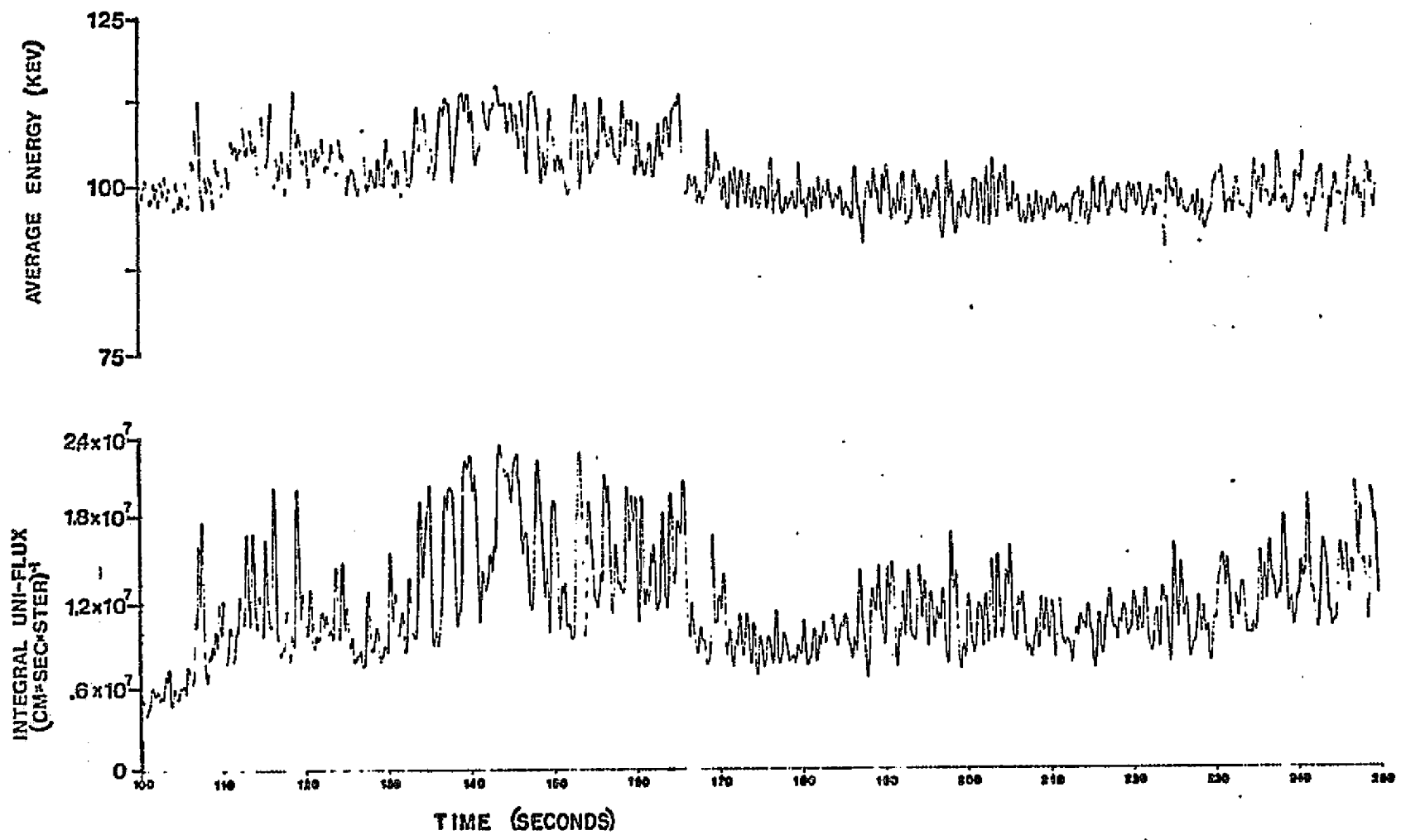


Figure 4.10. The integral flux shown in parallel with the average energy.

NORMALIZED FLUX

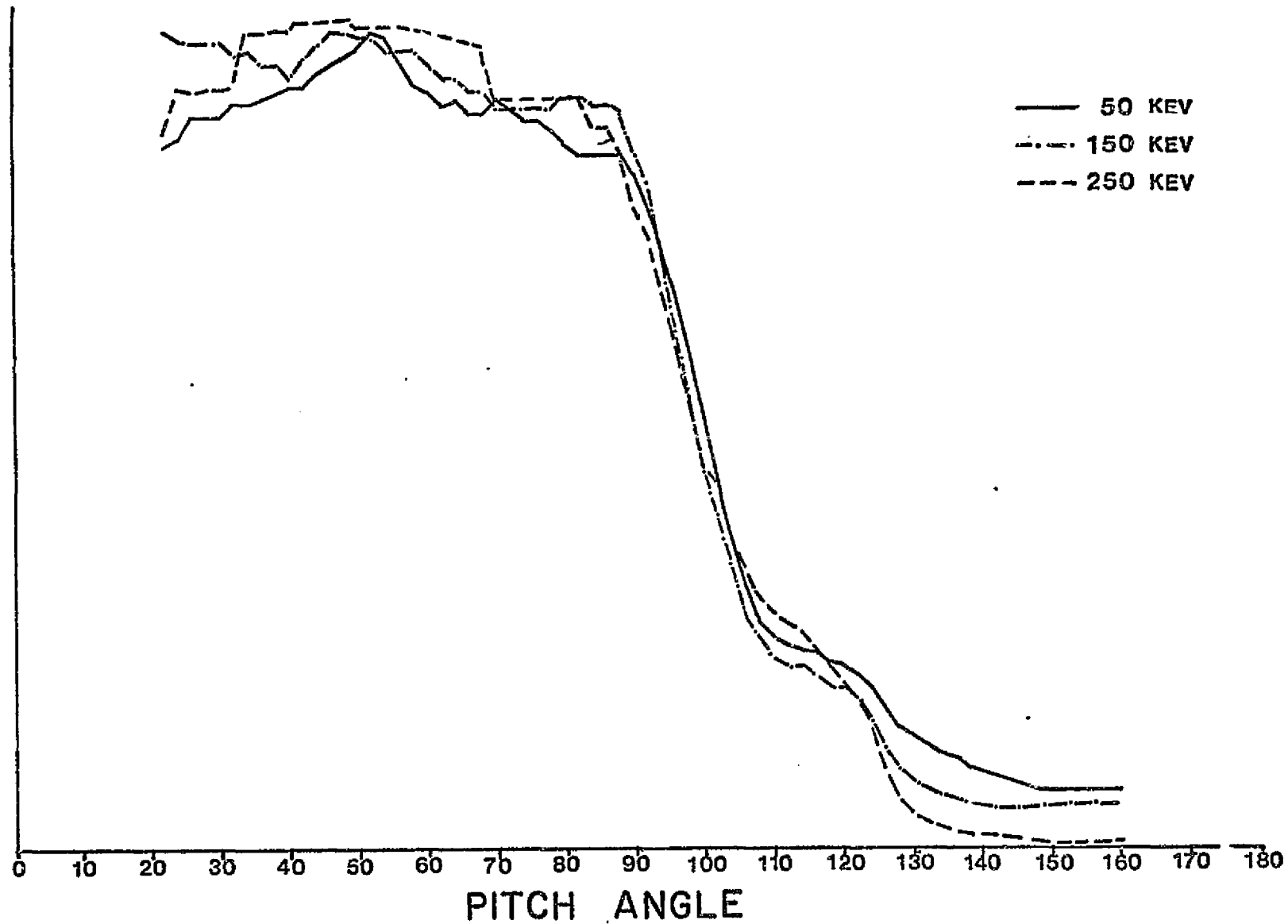


Figure 4.11a. The pitch angle distribution (interpolated to three energies and normalized to approximately the same peak value) shown at the peak of a pulsation.

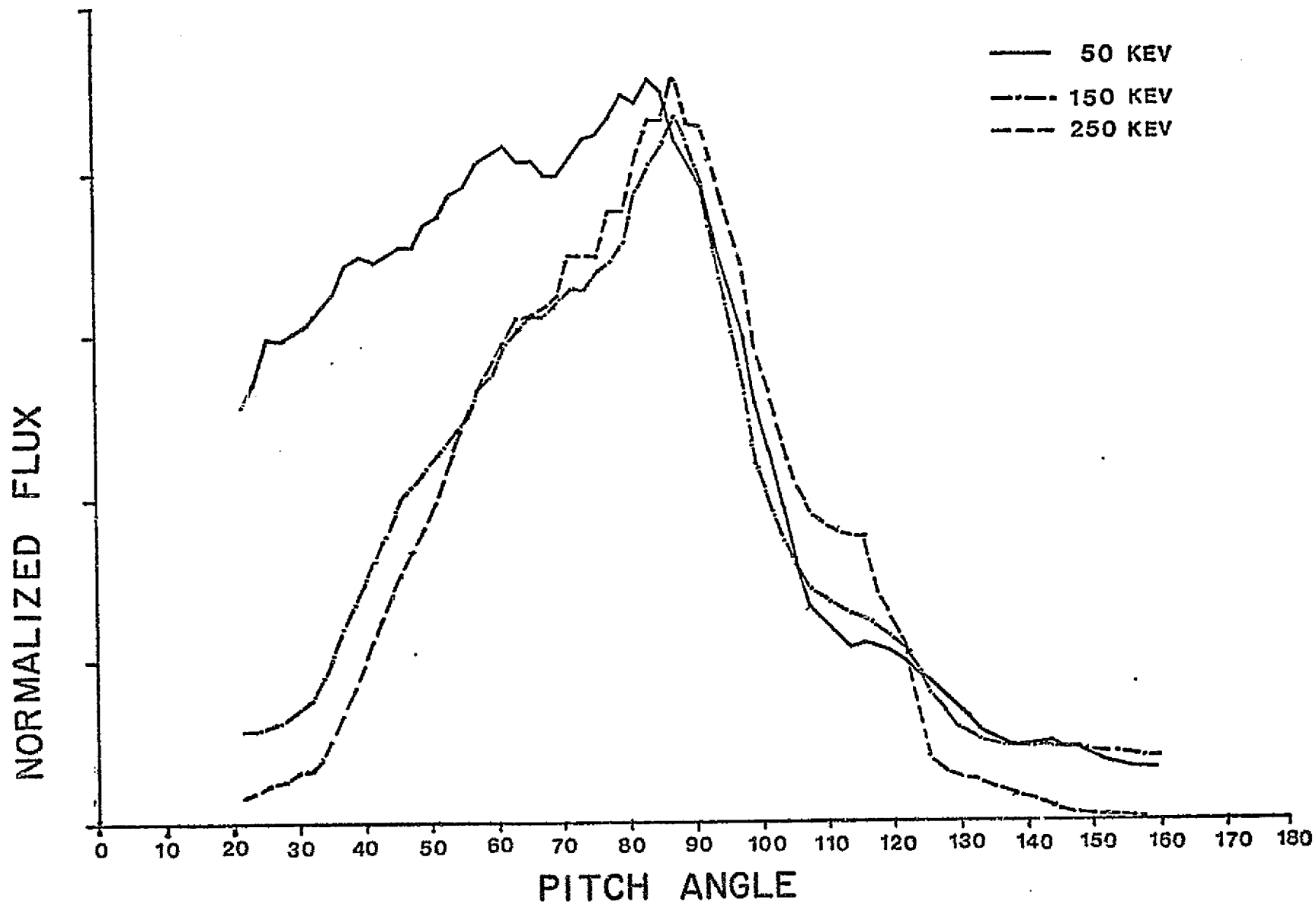


Figure 4.11b. The pitch angle distribution (interpolated to three energies and normalized to approximately the same peak value) shown at the valley between pulsations.

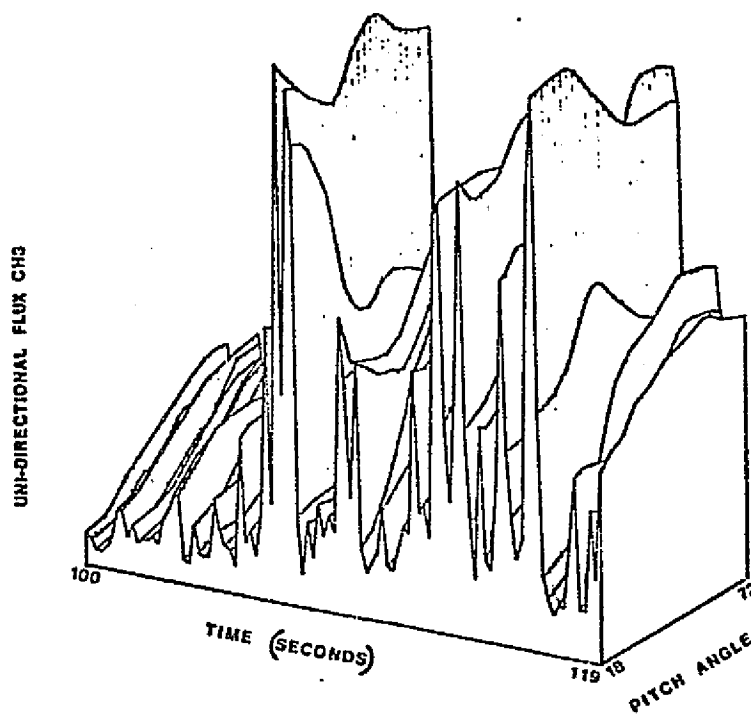
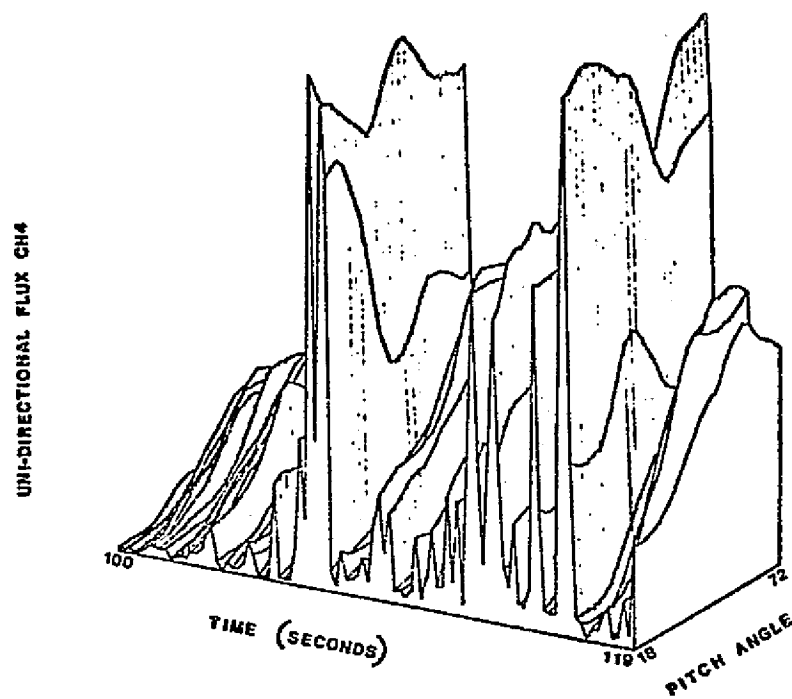


Figure 4.12 a and b. Pitch angle distributions over down coming particles for channels 3 and 4 from 100 seconds to 119 seconds.

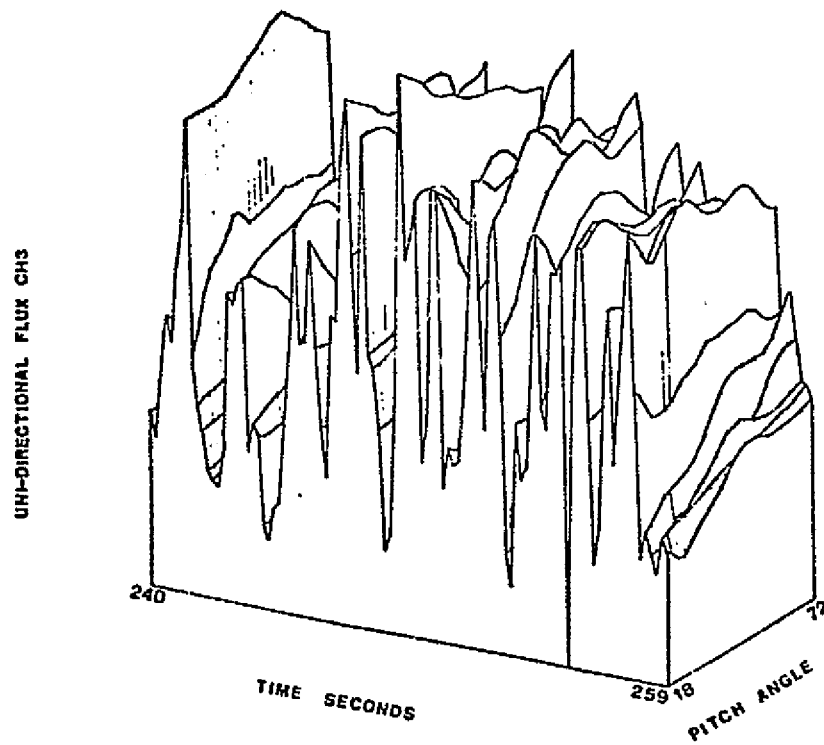
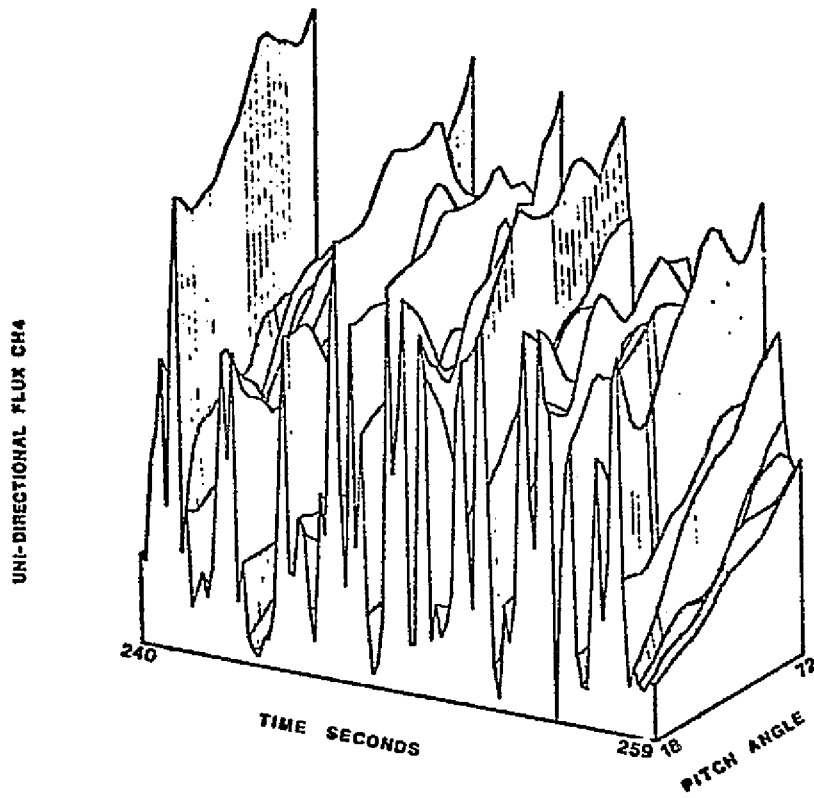


Figure 4.12 c and d. Pitch angle distributions over down coming particles for channels 3 and 4 from 240 seconds to 259 seconds.

degree detector taken over the periods of burst 1 and 3. The pitch angle distribution at the top of the bursts is more nearly isotropic the higher the flux level, but even at the lower levels there is a definite tendency toward isotropy as the flux increases. This behavior seems to be qualitatively the same for the large bursts, the small bursts, and even the fine structure pulsations.

Figure 4.10 shows that the average energy increases and decreases right along with the flux. This is of course a consequence of the more pronounced increases in the flux of the higher energy particles which may be seen in Figure 4.8. To within the time resolution of Figure 4.10, .095 seconds, the energy and the integral flux have a cross correlation which peaks strongly at zero. The change in the energy spectrum which accompanies the time variation in average energy is portrayed in Figures 4.13a and b where the spectra have been determined at adjacent peaks and valleys. The log-log scale in that figure may be misleading but a close examination shows that the proportional enhancement in the flux level is an increasing function of the energy.

A very clear picture of the precipitating electrons emerges from Figures 4.10 through 4.13. Particles appear in the loss cone simultaneously with an overall increased flux and an increased hardness. The increased hardness is brought about mainly by the enhancement of the high energy tail of the distribution. These particles out in the high energy tail are of course responsible for the event having been a REP in the first place, and we will pursue their origin in Chapter 5. We point out for emphasis at this point that most of the clear and positive results obtained from our data analysis are outlined in Figures 4.10 through 4.13.

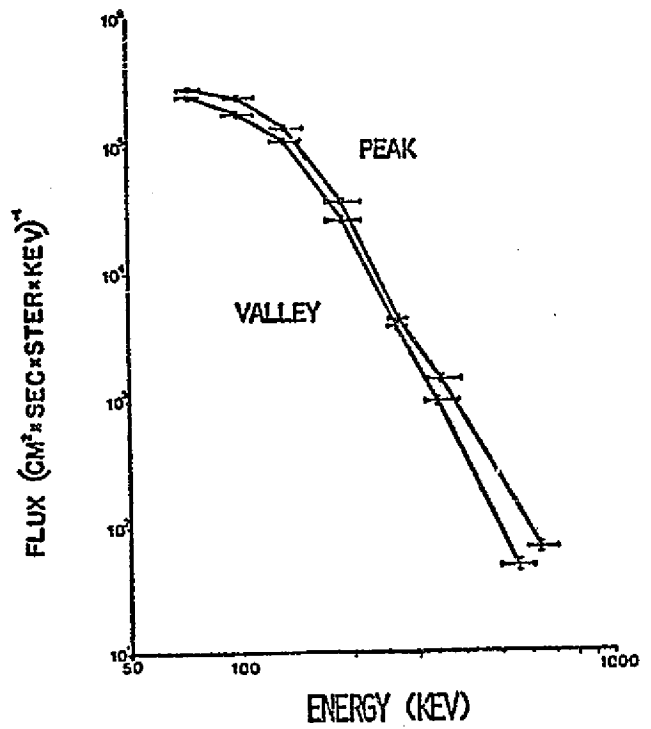
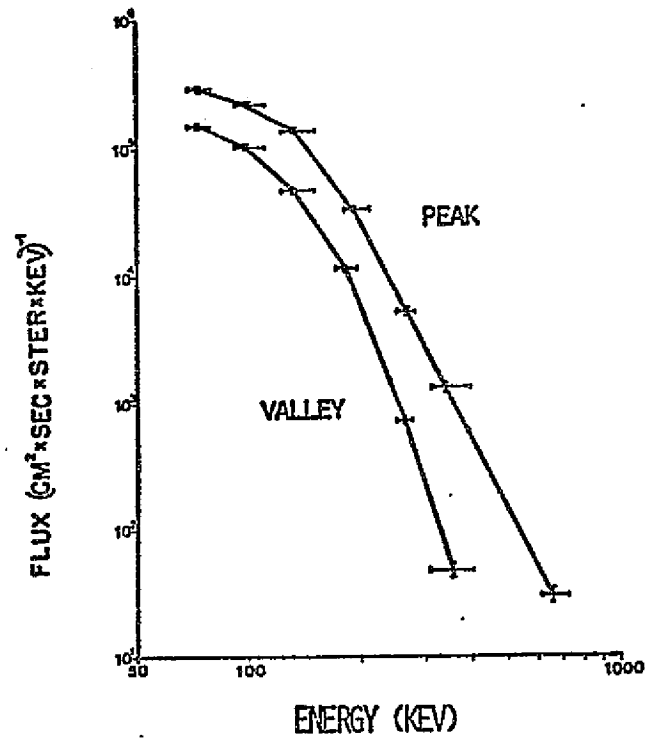


Figure 4.13a and b. Variation of energy spectra over pulsations.

#### IV.F. Time Series Analysis

The level of fluctuations which is so evident in Figures 4.8 and 4.10 suggests the possibility of strong frequency dependence in the REP. There are various forms of magnetospheric activity that have distinctive frequency characteristics which might be expected to appear in associated particle precipitation. It therefore seemed incumbent upon us to check the data systematically for frequency information.

As indicated previously the basic data accumulation period was .00853 seconds. This time period sets a theoretical limit on the frequency content of the data of about 58 hertz. (see below). While this is a very low frequency compared to the possible electron plasma and cyclotron frequencies that one expects, it certainly includes the range of geomagnetic micropulsations and ULF cyclotron waves that have been observed in the magnetosphere. Electron bounce times for Kev electrons are on the order of a second as well.

The rocket roll frequency is the dominant frequency present in the count rates from each of the detectors. This frequency is present because of the pitch angle anisotropy that existed to at least some small degree at all times during the flight. This periodicity is spacial. Any other spacial periodicity that exists in the pitch angle distribution will also be present in the raw count rates just as the roll periodicity is present. This sort of frequency information is indistinguishable from the overall fluctuations in the flux that may be present at all pitch angles. This is somewhat unsatisfying in that we would like to resolve the question as to whether the variations in flux levels that are present in Figures 4.6 are truly the basic time structure in the event or a strongly filtered component. The averaging time period for the data



in Figure 4.6 is .095 seconds which yields an upper frequency cutoff of about 5Hz (see below). We will demonstrate by a simple example how the higher frequencies are filtered by the averaging. This filtering does have the advantage of decreasing the effects of aliasing.

We suppose that the true time behavior of the flux may be represented by a function  $f(t)$  with a Fourier transform  $f(\omega)$ , which is related to the spectral density  $S(\omega)$  by the relation

$$S(\omega) = \frac{\pi}{T} |f(\omega)|^2 \quad (4.26)$$

$T$  is a period long with respect to all inverse frequencies of interest. When we sample the function  $f(t)$  by time averaging over a period  $T$  we actually create a new function  $f_{av}(t)$  defined by

$$f_{av}(t) = \frac{1}{T} \int_{t-T/2}^{t+T/2} f(t') dt' \quad (4.27)$$

which is sampled at evenly spaced points  $t_i$ . We trivially determine the Fourier transform of  $f_{av}(t)$  by substituting the Fourier transform of  $f(t)$  into equation (4.27) and interchanging the order of integration.

$$f_{av}(t) = \frac{1}{\sqrt{2\pi}} \int_{-\infty}^{\infty} f(\omega) \left\{ \frac{1}{T} \int_{t-T/2}^{t+T/2} e^{-i\omega t'} dt' \right\} \quad (4.28)$$

Carrying out the integration we find that

$$f_{av}(t) = \frac{1}{\sqrt{2\pi}} \int_{-\infty}^{\infty} f(\omega) \frac{\sin(\omega T/2)}{(\omega T/2)} e^{-i\omega t} d\omega \quad (4.29)$$

From which we identify

$$f_{av}(\omega) = f(\omega) \frac{\sin(\omega T/2)}{(\omega T/2)} \quad (4.30)$$

and the power spectral density

$$S_{av}(\omega) = S(\omega) \frac{\sin^2(\omega T/2)}{(\omega T/2)^2} \quad (4.31)$$

Those frequencies which satisfy the relation

$$\frac{\omega T}{2} = n\pi \quad (4.32)$$

are totally absent in  $S_{av}(\omega)$ . The half power point is at the frequency  $\omega_{1/2}$  determined by the relation

$$\sin^2\left(\frac{\omega_{1/2} T}{2}\right) = \frac{(\omega_{1/2} T)^2}{8} \quad (4.33)$$

with the power dropping off very rapidly beyond this frequency. (See Figure 4.14)

In the digital technique applied to determine the power spectral density we use a finite set of equally spaced data points. The useful frequency region will be from 0 to  $\pi/T$  radians per second since frequencies higher than  $\pi/T$  will be folded into the lower frequency

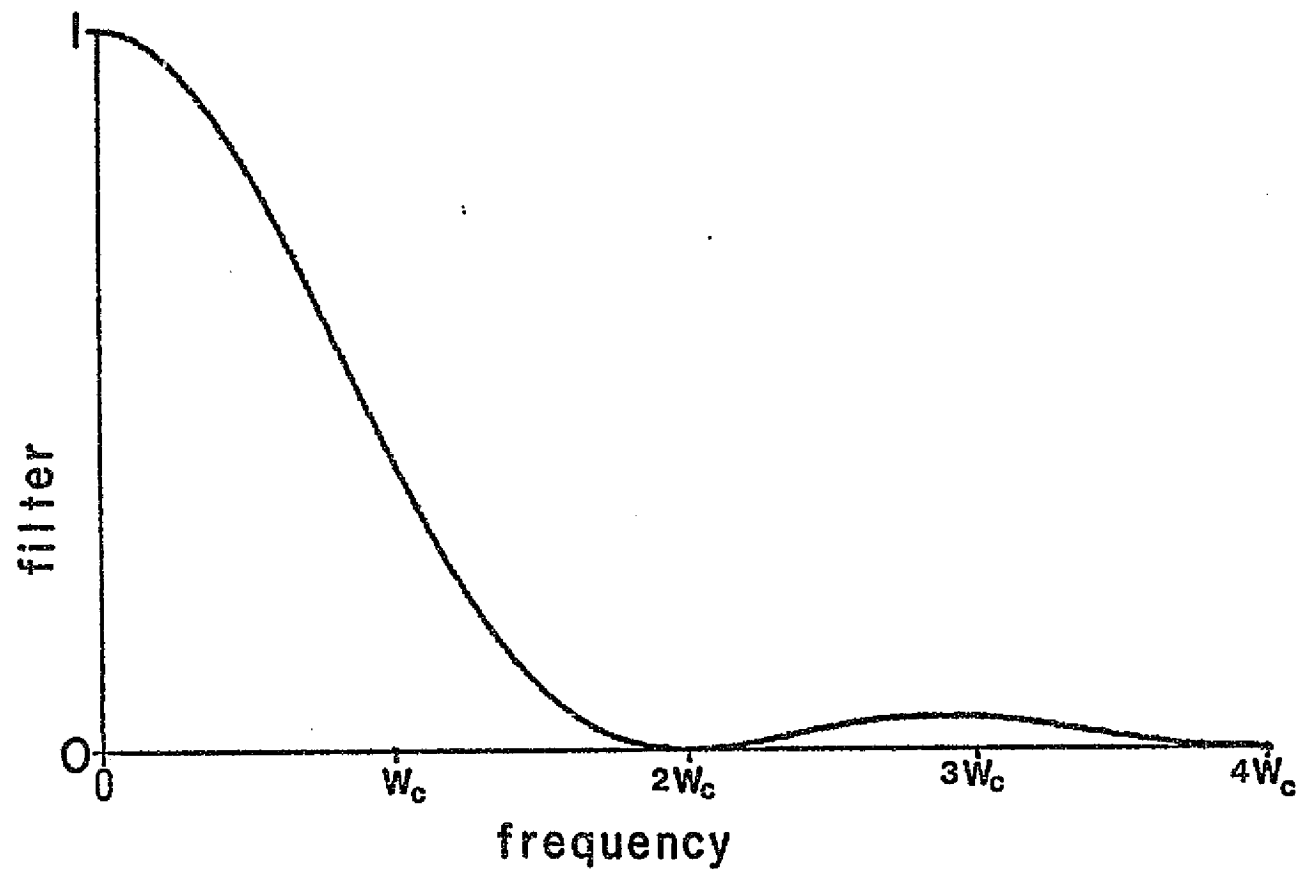


Figure 4.14. Effective frequency filter due to time averaged sampling.

range. The upper cut-off frequency is called the Nyquist frequency

$$\omega_c = \pi/T \quad (4.34)$$

The frequencies  $\omega_a$ , higher than the Nyquist frequency which are folded into frequencies,  $\omega$ , below the Nyquist frequency, are called aliased frequencies and they satisfy the relation

$$\omega_a = 2n\omega_c \pm \omega \quad (4.35)$$

with  $n$  being an integer (Bendat and Piersol, 1966). In our case aliasing is much less significant in that  $\omega_c$  is slightly greater than the half power frequency,  $\omega_{1/2}$ , so that all frequencies above  $\omega_c$  are fairly well filtered.

The frequency analysis was performed using standard digital techniques which may be found in Bendat and Piersol (1966). The definitions are repeated here for completeness.

$T$  is the basic data sampling interval and the deviation  $\hat{x}_n$  of the  $n$ th point in the series  $x_n$  is given by

$$\hat{x}_n = x_n - \bar{x} \quad (4.36)$$

with  $\bar{x}$  being the average value of  $x_n$  and  $x_n$  being the value of  $x(t)$  at  $t = nT$ .  $R_m$  is defined to be the autocorrelation coefficient at  $t = mT$  and is given by the relation

$$R_m = R(mT) = \frac{1}{N-m} \sum_{n=1}^{N-m} \hat{x}_n \hat{x}_{n+1} \quad (4.37)$$

We may then determine the raw estimate of the power spectral density  $S_r(f)$ .

$$S_r(f) = 2T \left\{ R_0 + 2 \sum_{m=1}^{M-1} R_m \cos \left( \frac{\pi m f}{f_c} \right) + R_M \cos \left( \frac{\pi M f}{f_c} \right) \right\} \quad (4.38)$$

In which we take  $f$  as the frequency in hertz so that  $f_c = w_c/2\pi$ .  $M$  is the maximum value of  $m$  where  $m$  is referred to as the number of lags.  $f$  in equation 4.34 is evaluated at even multiples of  $\frac{1}{M}$  our estimates the raw estimates have been smoothed with 'Hanning' formulas

$$\begin{aligned} S(f_n) &= .23 S(f_{n-1}) + .54 S_r(f_n) + .23 S_r(f_{n-1}) \\ S(f_0) &= .54 S_r(f_0) + .45 S_r(f_1) \\ S(f_M) &= .54 S_r(f_M) + .46 S_r(f_{M-1}) \end{aligned} \quad (4.39)$$

The standard error of  $S(f_n)$  is given by the relation

$$\sigma_f = \sqrt{\frac{M}{N}} S(f_n) \quad (4.40)$$

so that the maximum number of lags,  $M$ , must be chosen small with respect to the number of points,  $N$ .

The spectral analysis was performed on both the averaged data and the raw data. The averaged data had a time interval of .0938 seconds between points and therefore a Nyquist frequency of 5.33 Hz. This is a bit less than the rocket roll frequency of 5.463 Hz. The Nyquist frequency for the raw data set is 58.8 Hz. Figures 4.15 a & b show an example of the power spectral estimates over the first third of the flight for two energy channels from the averaged data set. There are four peaks which show up quite distinctly in these figures and are also present in the spectral estimates for all of the channels one through seven. These are the peaks at .2, .34, .64 and .906 Hz. In addition there are peaks at .453, .800 and 1.49 Hz which are more distinct the higher the energy of the channel. The standard error is indicated on the figure. As might be expected, the roll frequency has aliased into the spectral estimates at 5.2 Hz. As a result of the frequency filtering though its contribution to the power spectral estimate has been reduced by 62 per cent. All of the prominent peaks are sufficiently below the half power frequency so as to not warrant any correction.

The most significant feature of the power spectra in Figures 4.14a and 4.14b is the lack of any really dominant frequency. The fine structure time variation certainly appears to have a periodic structure. The power spectra indicates that there are in fact several low frequencies strongly present in this quasic-periodic behavior.

Figures 4.15a and b show examples of the power spectral estimates over the first third of the flight for two energy channels from the raw data. The largest peaks are from the roll variation which shows up out to as much as 5 harmonics. These very strong features tend to swamp any features too close to them. Just resolved from the first harmonic of the

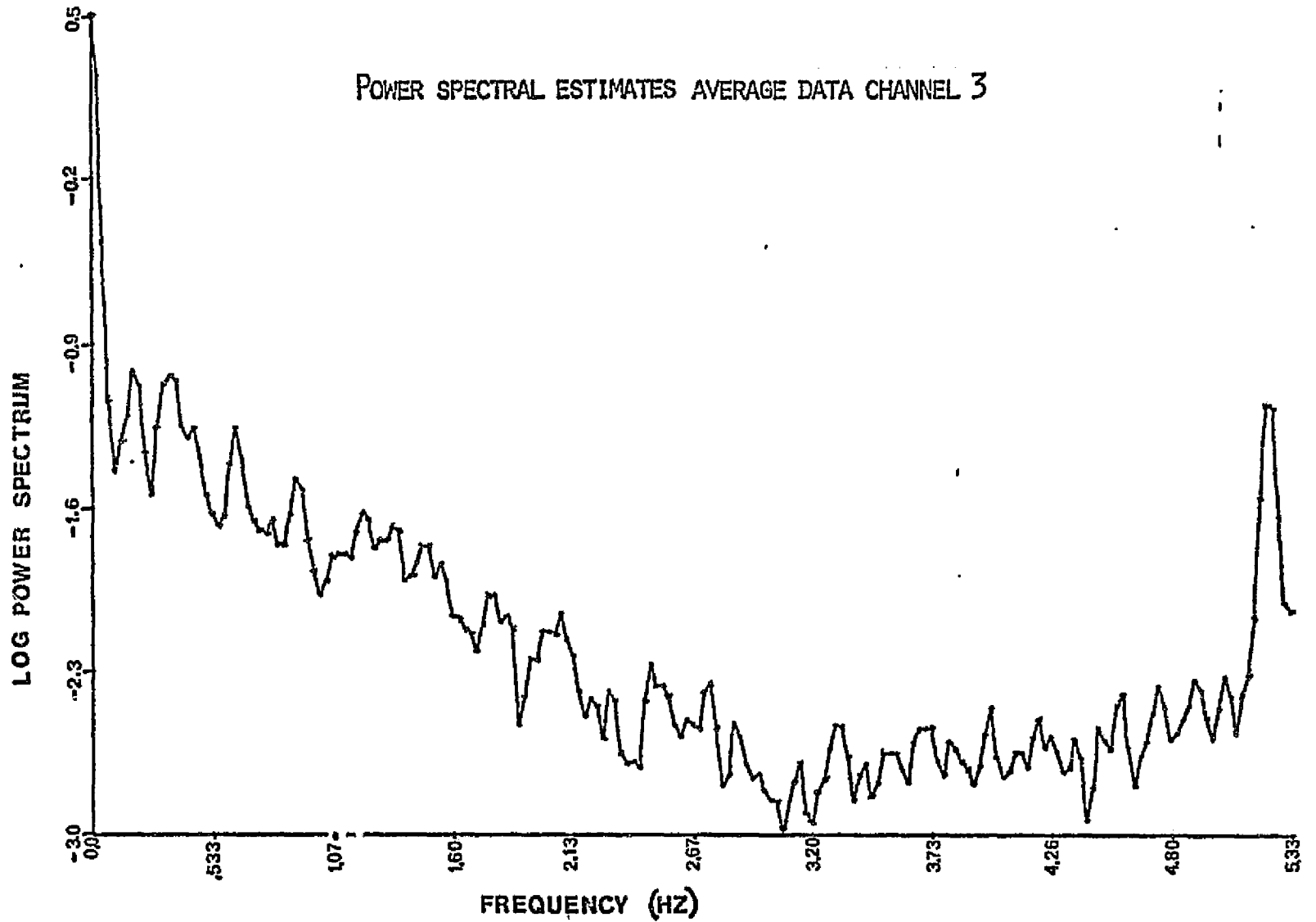


Figure 4.15a. Power spectral estimates over averaged data set for channel 3

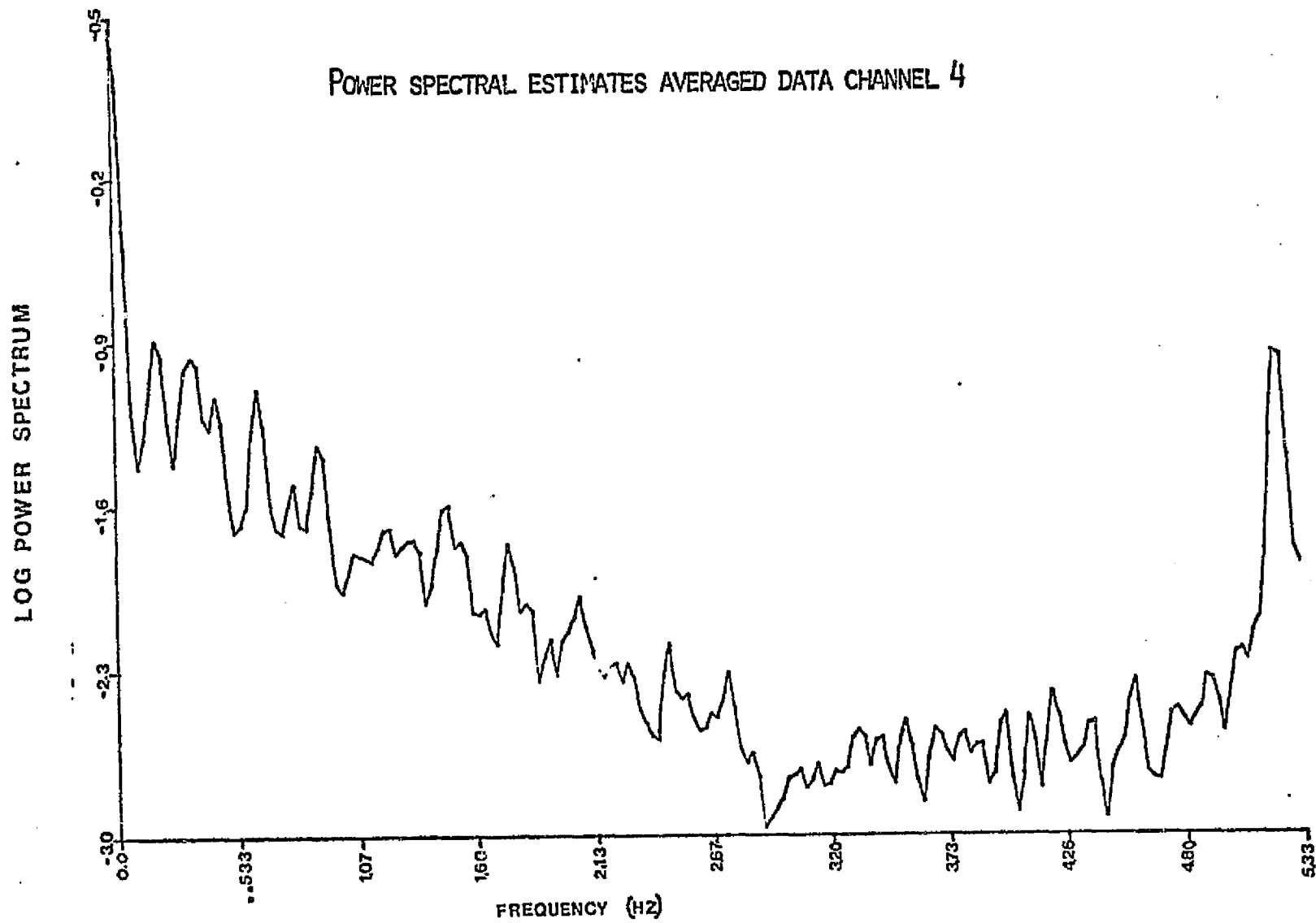


Figure 4.15b. Power spectral estimates over average data set for channel 4.



roll is a peak at 6.17 Hz which also appears at the second harmonic frequency of 12.34 Hz. 6.17 Hz is present in channels one through seven from the beginning to the end of the flight. There are evidently many peaks in the spectra which are statistically significant, though none of them dominate (with the exception of the roll frequency). These results leave us with more of an indication of what is not present in the data than any positive indication that we had hoped might emerge.

Using techniques similar to the power spectral estimates, cross-correlations were determined between the several energy channels. The expectation is that a precipitation mechanism acting over a finite region of space, sufficiently removed from the rocket, will lead to arrival time dispersion in the particle counts at different energies. As with the above results the information was of a negative rather than a positive nature. To within a time resolution of .00853 seconds the particle fluxes in all channels were most strongly correlated at a log time of 0 seconds. If 50 Kev and 600 Kev particles were simultaneously injected into the loss cone at the equator on an L shell of 6, they would arrive at the foot of the field line with a time separation of about .196 seconds. This is a time which is resolvable in our data. We have the problem though that the roll correlation may be so strong and broad as to swamp all other correlations that lay near by. The energy width of the various channels is also broad and would tend to broaden and decrease any true correlation of this sort. Lastly the finite width of any interaction region about the equator would also lead to a smearing of such a dispersion effect. We are left to conclude that the absence of such dispersion related correlations is not in itself definitive. Our time resolution is such though that if we were to take these results as

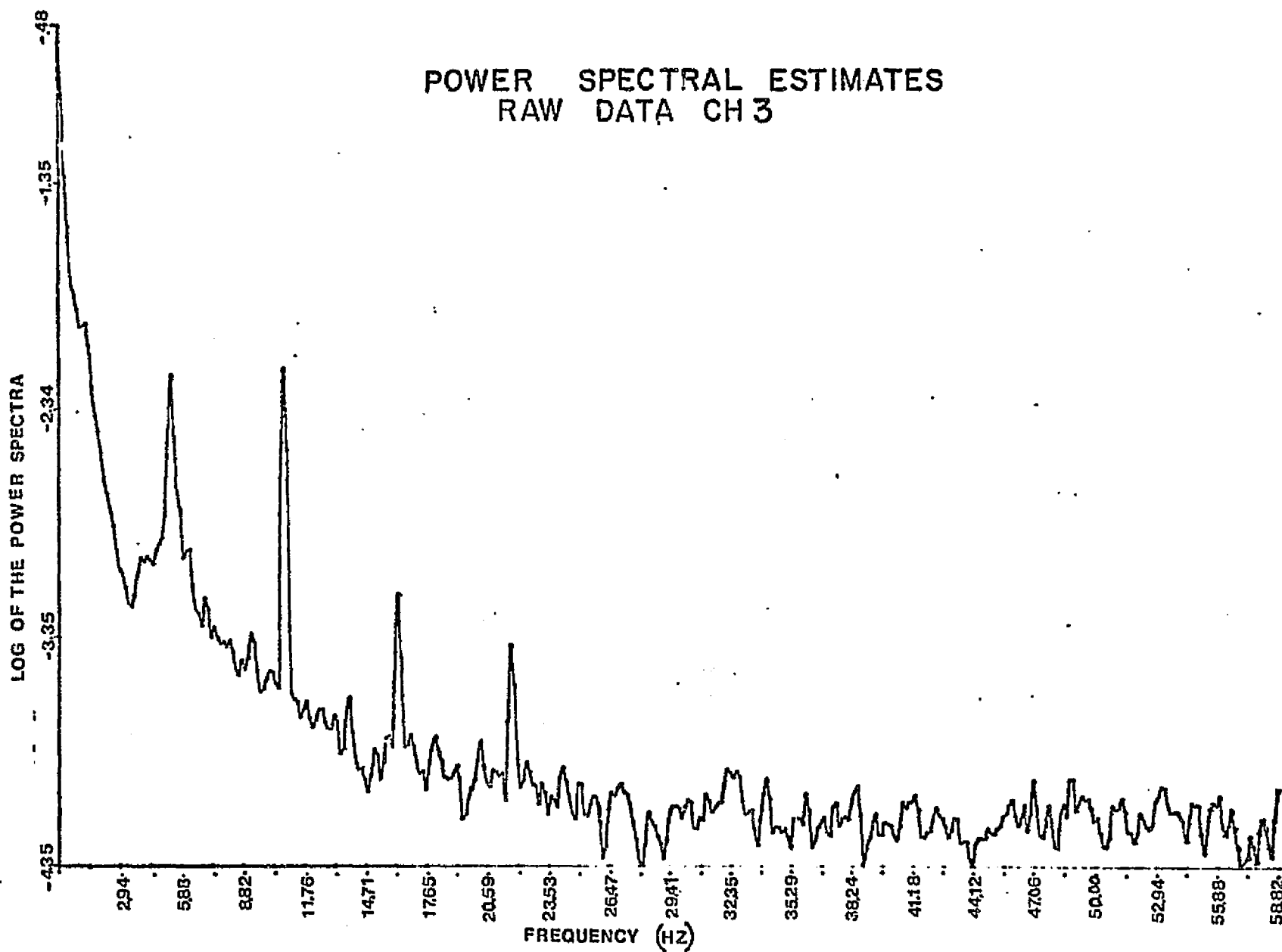


FIGURE 4.16a. POWER SPECTRAL ESTIMATES OVER RAW DATA SET FOR CHANNEL 3 FOR 10,000 DATA POINTS.

POWER SPECTRAL ESTIMATES  
RAW DATA CH 4

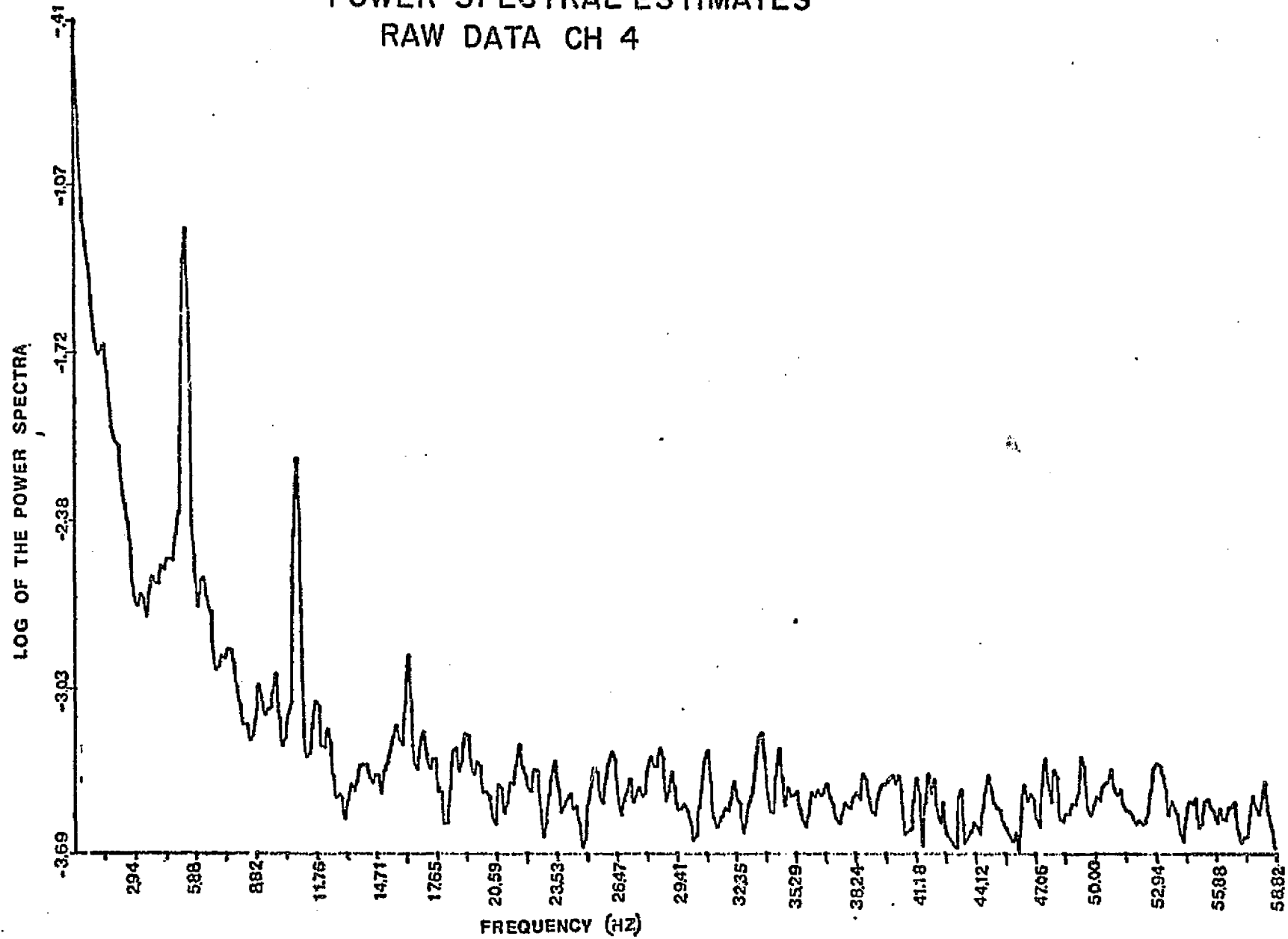


FIGURE 4.16B. POWER SPECTRAL ESTIMATES OVER RAW DATA SET CHANNEL 4 FOR 10,000 DATA POINTS.

definitive we would have to conclude that the interaction region was at most only some  $.3 R_E$  up the field line. We repeat though that we do not feel that this is at all definitive.

## CHAPTER V

### SOME THEORETICAL CONSIDERATIONS ON REP'S

#### V.A. The REP And The Trapped Particle Population

As has been indicated in the introduction, the REP is quite uncommon when compared to magnetic substorms (Bailey, 1968). If REP's are truly a substorm related phenomenon then some other features of the magnetosphere must determine when substorms will lead to REP's. Numerous papers have been published detailing the enhancements of trapped particles in the magnetosphere during and following magnetic substorms (see for instance Pfitzer and Winckler, 1968). The reports based upon data taken by synchronous satellites which have been located on the L = 6 field lines (Mozer, 1972; Bogott and Mozer, 1974) are of particular interest in this respect. Rosenberg et al (1972) compared the precipitated flux with the trapped particle flux at synchronous orbit for the REP events of 25 August 1967 and 11 August 1967. They determined that there were marked enhancements of the trapped particle population prior to the REP's probably due to substorm associated injection of particles on the night side of the magnetosphere. While the 25 August event was accompanied by significant enhancement of trapped relativistic electrons, the 11 August event was not. They concluded that there were at least two distinct subclasses of REP's. The best e-folding energy which would be fitted to our average fluxes was about 40 Kev. This corresponds very well with the hard component of the precipitated flux of the 11 August event (Rosenberg et al 1972). The e-folding energy of the hard component of the 25 August event was significantly greater than this. Though it is not conclusive the data does support that the REP of 31 May 1972 was

of the same class as the REP of 11 August 1967 and therefore might not have been associated with a significant enhancement in the trapped relativistic particle population. In our following considerations we have not made any attempt to draw any distinction between the two types of REP's but rather looked at the more general problem of how might relativistic electrons be produced in a post-substorm magnetosphere.

Many authors have discussed electron-cyclotron wave gyroresonant interactions (for example Kennel, 1966; Kennel and Petschek 1966; Kennel and Engelmann 1966; Lerche 1968; Coroniti and Kennel 1970) and it is generally accepted that these interactions are a major cause of diffusion of electrons into the magnetospheric loss cone. As described by Kennel and Petschek (1966) and many authors since, electron whistler interactions, under certain conditions, establish an upper limit to the stably trapped fluxes. The atmosphere at the foot of each field line establishes and maintains a loss cone anisotropy. Particles diffusing down into the loss cone tend to spread the anisotropy to pitch angles above the atmospheric loss cone. Whistler waves are unstable in the presence of such an anisotropy and will grow forcing particles down into the loss cone tending to remove the anisotropy. A complicated nonlinear equilibrium is established in which wave loss and growth and particle loss and diffusion all balance each other. A completely self consistent and general mathematical solution to such a problem has not been carried out. Kennel and Petschek (1966) attempted a solution but were forced to make many assumptions about the nature of sources and the form of the pitch angle anisotropy and therefore intended their model to be only semiquantitative. A long term study by Mozer (1972) of the trapped particle population on  $L = 6$  showed that electron fluxes rarely exceeded the limit predicted

by Kennel and Petschek (1966) and never exceeded that limit by more than a factor of two. The integral flux of electrons ( $E > 50$  Kev) that was observed during the REP of 31 May 1972 was at times at or slightly above the Kennel and Petschak stable limit. The particles observed at 150 km are mainly in a region of pitch angle space which corresponds to the equatorial loss cone and therefore normally exhibit lower fluxes than the trapped flux. It seemed reasonable following these considerations to examine the cyclotron resonant diffusion theory to determine if the inclusion of relativistic terms might not point the way to a possible production mechanism for REPs. A number of very interesting and possibly important points have emerged from our investigation.

#### V.B. The Whistler Dispersion Relations

The standard treatment (as exemplified by the above references) of the parallel propagating right hand cyclotron wave mode (referred to also as R-H mode and whistler mode) assumes a cold background plasma, the dielectric properties of which determine the wave dispersion relations. We say the cold plasma supports the plasma waves. The interactions of these 'cold plasma waves' with the distribution of highly energetic electrons are the wave particle interactions of interest. It is assumed that the effective number density of the 'superthermal' electrons is so low as to not affect the dielectric properties of the 'background' plasma. The complete dispersion relation for the RH-mode waves may be written

$$\frac{k^2 c^2}{\omega^2} = 1 + \frac{\omega_{pe}^2}{\omega(\Omega_{ce} - \omega)} - \frac{\omega_{pi}^2}{\omega(\Omega_{ci} + \omega)} \quad 5.1a$$

(Krall and Trivelpiece, 1973) with  $\omega_{pe}$  ( $\omega_{pi}$ ) and  $\Omega_{ce}$  ( $\Omega_{ci}$ ) being the electron (ion) plasma frequency and the electron (ion) gyrofrequency respectively. These frequencies are given by the relations

$$\omega_{p\alpha}^2 = \frac{4\pi n_{\alpha} e^2}{m_{\alpha}} \quad \text{and} \quad \Omega_{c\alpha} = \frac{eB}{m_{\alpha} c} \quad 5.2$$

with  $\alpha$  standing for the ion species,  $m_{\alpha}$  the ion mass and  $n_{\alpha}$  the number density of species  $\alpha$ . (We are using cgs gaussian units and will do so throughout this chapter and associated appendices).

For a neutral hydrogen plasma one has  $n_e = n_i$  and  $m_e/m_i = 5.4 \times 10^{-4}$  so that equation 5.1a may be written

$$\frac{k^2 c^2}{\omega^2} = 1 + \frac{\omega_{pe}^2}{(\Omega_{ce} - \omega)(\Omega_{ci} + \omega)} \quad 5.1b$$

For virtually all discussions of electron-whistler mode interactions in the magnetosphere the articles in the literature contain an approximate form of this dispersion relations. The assumption is made that

$$\Omega_{ci} < \omega \ll \Omega_{ce} \ll \omega_{pe} \quad 5.3$$

so that the dispersion relation may be written

$$\frac{k^2 c^2}{\omega^2} = \frac{\omega_{pe}^2}{\Omega_{ce}(\Omega_{ci} + \omega)} \quad 5.1c$$

When condition 5.3 is not met equations 5.1b and 5.1c yield greatly different results. In fact at the equator on the  $L = 6$  field line there are times when condition 5.3 is not true. Typical quiet time densities may run as high as  $5/\text{cm}^3$  (Chappel et al, 1970) while during



disturbed periods following substorms the density may be less than  $.1/\text{cm}^3$  (Williams and Lyons, 1974). Using a dipole field approximation the field  $B_0$  at the equator is given by

$$B_0 = \frac{.32}{L^3} \text{ gauss} \quad 5.4$$

This yields a value for  $\Omega_{ce}$  of 26 rad/sec. For  $n_0 = 5/\text{cm}^3$ ,  $\omega_{pe} \approx 126$  rad/sec and condition 5.3 can be met. For  $n_0 = 0.1/\text{cm}^3$ ,  $\omega_{pe} \approx 18$  rad/sec so that condition 5.3 cannot be satisfied. In Figure 5.1 we show the exact dispersion relation and the approximate dispersion relation for case of  $\omega_{pe} \approx 18$  rad/sec. For frequencies,  $\omega$ , below  $0.1 \Omega_{ce}$  the two dispersion relations are in fairly good agreement.

The range of frequencies that are dealt with in a theoretical treatment of the wave-particle interactions depends upon the energies of the particles of interest. These frequencies are determined through the resonance condition which is obtained in appendix B (see equation B.42). The resonance condition may be written

$$v_R = \frac{\omega - \Omega_{ce}/\gamma}{K} \quad 5.5$$

in which  $v_R$  is the particle velocity parallel to the magnetic field and  $\gamma$  is the relativistic mass correction.  $\omega$  and  $K$  are related through the dispersion relation. We will consider particles in the tens of Kev range to the near Mev range. With  $n_0 = 0.1/\text{cm}^3$  equation 5.5 combined with 5.1b tells us that a 60 Kev electron is resonant with a wave with  $\omega > .5 \Omega_{ce}$ . This is well out of the range of validity of the approximate dispersion relation.

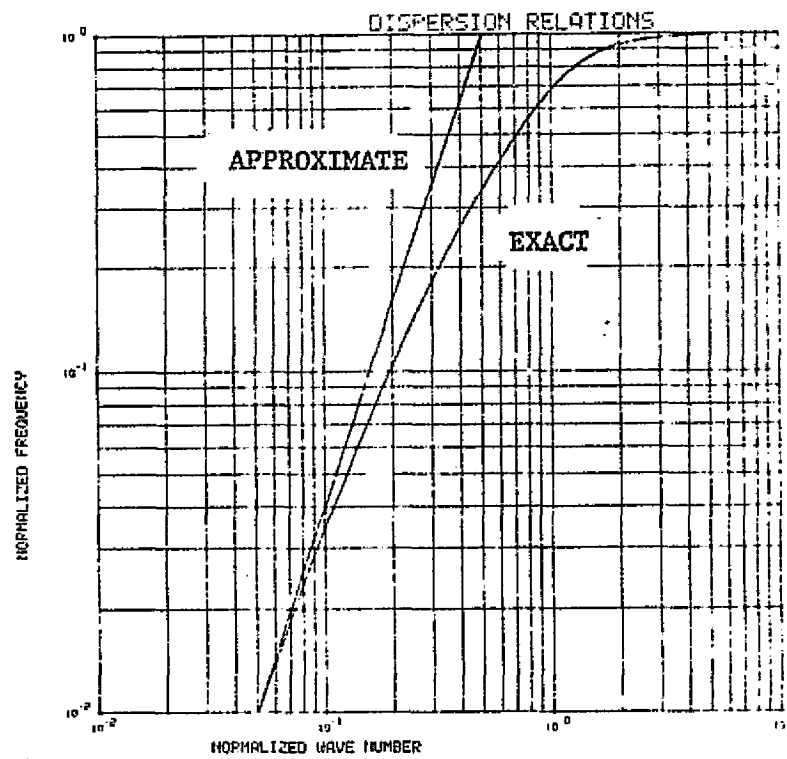


Figure 5.1. Approximate dispersion relation and the exact dispersion relation when  $\Omega_{ce} = 26$  khz and  $\omega_{pe} = 18$  khz.

137

From the above we are lead to conclude that during disturbed times when particle densities were low the full RH-mode dispersion relation must be used to model cyclotron wave-electron interactions. It is also important to point out that any theoretical predictions made using the approximate dispersion relation are at least questionable at times of low density exterior to the plasmopause.

### V.C. The Quasilinear Diffusion Equations

In the following we will use the full cold particle dispersion relation (eq. 5.1b) and the fully relativistic quasilinear diffusion equations, which we have derived in appendix B, to examine the electron-whistler interactions in a low density case as described above. In deriving the following equations we have assumed that there is a region of sufficient uniformity about the equator to treat the magnetic field and plasma as being equivalent to that in a uniform infinite plasma. This is a standard approximation the justification of which is to be found in the article by Kennel, 1966 and Kennel and Petschek, 1966. The set of quasilinear equations (see appendix B) are

$$\frac{\partial f_{eo}}{\partial t} = 4\pi e^2 \int_{-\infty}^{\infty} dK \left[ \frac{1}{P_{\perp}} \left\{ \frac{kv_{\perp}}{\omega} \frac{\partial}{\partial P_{\perp}} + \left(1 - \frac{kv_{\parallel}}{\omega}\right) \frac{\partial}{\partial P_{\parallel}} \right\} \left\{ \frac{P_{\perp} E_k \omega_{\perp}}{\left(kv_{\parallel} + \frac{\Omega_{ce}}{\gamma} - \omega\right)^2 + \omega_{\perp}^2} \right. \right. \\ \left. \left. \left( \frac{Kv_{\perp}}{\omega} \frac{\partial f_{eo}}{\partial P_{\perp}} + \left(1 - \frac{Kv_{\parallel}}{\omega}\right) \frac{\partial f_{eo}}{\partial P_{\parallel}} \right) \right\} + 4\pi^2 e^2 \left\{ \frac{1}{P_{\perp}} \left( \frac{Kv_{\perp}}{\omega} \frac{\partial}{\partial P_{\perp}} + \left(1 - \frac{Kv_{\parallel}}{\omega}\right) \frac{\partial}{\partial P_{\parallel}} \right) \right. \right. \\ \left. \left. \left( \frac{E_k P_{\perp}}{|v_{\parallel}|} \left\{ \frac{kv_{\perp}}{\omega} \frac{\partial f_{eo}}{\partial P_{\perp}} + \left(1 - \frac{kv_{\parallel}}{\omega}\right) \frac{\partial f_{eo}}{\partial P_{\parallel}} \right\} \right) \right\} \right] \quad \left| \quad k = \frac{\omega - \Omega_{ce}/\gamma}{v_{\parallel}} \right. \quad \underline{\text{B.50}}$$

$$\omega_I(k) = \frac{\pi^2 \omega_{peh}^2 m_e \int_0^\infty p_\perp^2 dp_\perp \frac{\partial f_{eo}}{\partial p_\perp} + \frac{k}{\omega} (v_\perp \frac{\partial f_{eo}}{\partial p_\parallel} - v_\parallel \frac{\partial f_{eo}}{\partial p_\perp})}{|k| \left[ \frac{2k_c^2}{\omega^2} + \frac{\omega \omega_{pe}^2 (2\omega - \Omega_{ce})}{(\Omega_{ce} - \omega)^2 (\omega + \Omega_{ci})^2} \right]} \quad |P_\parallel = P_R$$

B.45

$$E_k(t) = E_{k0} e^{2\omega_I t} \quad 5.6a$$

$$P_R = \gamma m_e \left( \frac{\omega - \Omega_{ce}}{k} \right) \quad 5.7$$

in which  $\omega_I(k)$  is the linear growth rate of waves of frequency  $\omega(k)$ ,  $E_k$  is the spectral energy density of these waves,  $\omega_{peh}$  is the plasma frequency associated with the number density of superthermal electrons,  $f_{eo}$  is the distribution function of superthermal electrons,  $d\Omega_k$  is a small solid angle about the parallel propagation vector of waves  $k$  and  $p_\perp$ ,  $p_\parallel$ ,  $v_\perp$  and  $v_\parallel$  are the momentum and velocity of the particles perpendicular and parallel to the magnetic field.  $f_{eo}$  is a function of time and momentum but is defined in such a way as to be spatially uniform (see appendix B). Azimuthal symmetry is assumed about the magnetic field.  $\partial f_{eo}/\partial t$  is the quasilinear change in the distribution function due to wave particle interactions. Equation B.50 is essentially a diffusion equation in momentum space. We have derived this equation by following the basic procedure of Drummond and Pines (1955), although the same results should be obtainable using a Fokker-Planck approach. To the extent that the approximations are appropriate to this set of equations should describe both the energy and pitch angle diffusion of the electrons due to interactions with whistler mode waves. It is a trivial exercise

to show that in the limit of nonrelativistic particles and pure pitch angle diffusion equation B.50 is identical to that given by Kennel, 1966.

For our later considerations we will modify equation 5.6 to the equivalent differential form

$$\frac{dE_k}{dt} = 2\omega_{I_k} E_k \quad 5.6B$$

and introduce a convective term which will allow wave energy to be removed from the equatorial interaction region at the wave group velocity.

We write this as

$$\frac{dE_k}{dt} = 2\omega_{I_k} E_k - \frac{v_g E_k}{L} \quad 5.6c$$

in which  $v_g$  is the wave group velocity and  $L$  is a length characterizing the size of the interaction region.

As formulated above  $f_{e0}$  is a function of  $p_{\perp}$  and  $p_{\parallel}$  where  $p_{\parallel}$  extends from  $-\infty$  to  $\infty$ . The dispersion relation 5.1b has two branches one for positive going waves and one for negative going waves, (Krall and Trivelpiece, 1973). We will make some symmetry arguments which will limit the domain in consideration as well as simplify some of our further discussion. We argue that there is no preferred direction parallel to the magnetic field so that as many particles move one way as the other. This is also true for waves. This leads to the following conclusions:

$$f_{eo}(p_{\parallel}, p_{\perp}) = f_{eo}(-p_{\parallel}, p_{\perp})$$

$$\frac{\partial f_{eo}}{\partial(-p_{\parallel})} = - \frac{\partial f_{eo}}{\partial p_{\parallel}} \quad 5.8$$

If we can reduce our considerations properly to the development of  $f_{eo}$  for positive  $p_{\parallel}$  we will automatically know it for  $-p_{\parallel}$ . This should be true for the wave spectrum as well. Knowing the spectral energy density of positive going waves is equivalent to knowing the wave spectrum for negative going waves.

Consider equation P.45 above for the linear growth rate. This expression must be evaluated with the resonance condition, equation 5.5, at each value of  $p_{\perp}$ . Equation 5.5 may also be written in terms of the resonant momentum

$$p_R = \frac{m_e (\gamma\omega - \Omega_{ce})}{k} \quad 5.9$$

As  $\gamma\omega$  may be larger than  $\Omega_{ce}$  (provided that  $\gamma$  is sufficiently large) there will be both positive and negative value  $p_R$ . In the non-relativistic limit the resonant momentum is always negative since  $\omega$  is always less than  $\Omega_{ce}$  (for cyclotron waves). We will restrict the range of  $p_{\parallel}$  to only positive values in equation B.45 by breaking equation 5.9 into two conditions

$$p_R = \begin{cases} \frac{m_e (\gamma\omega - \Omega_{ce})}{k}, & + \text{ resonance} \\ \frac{m_e (\Omega_{ce} - \gamma\omega)}{k}, & - \text{ resonance} \end{cases} \quad 5.10$$

with  $p_R$  always greater than zero. Equation B.45 then is rewritten as

$$\omega_I(k) = \frac{\pi^2 \omega_{pe}^2 \int_0^\infty p_\perp^2 dp_\perp \left\{ \frac{\partial f_{eo}}{\partial p_\perp} \pm \frac{k}{\omega} \left( v_\perp \frac{\partial f_{eo}}{\partial p_\parallel} - v_\parallel \frac{\partial f_{eo}}{\partial p_\perp} \right) \right\}}{|k| \left( \frac{2k^2 c^2}{\omega^2} + \frac{\omega \omega_{pe}^2 (2\omega - \Omega_{ce})}{(\Omega_{ce} - \omega)^2 (\omega + \Omega_{ci})^2} \right)} \Bigg|_{p_\parallel = p_R^\pm} \quad 5.11$$

in which we have used the symmetry conditions 5.8. We simply consider what happens to the positive going particles and assume the same must happen to the negative going ones.

#### V.D. The Implications of Pitch-Angle Anisotropy

At this juncture we will attempt to motivate the rest of our discussion by considering a particular class of distribution functions,  $f_{eo}(p_\perp, p_\parallel)$  and the implications of equation 5.11 for the linear growth rate with respect to this class of functions. It has been noted experimentally that substorm associated injections of energetic particles tend to be at flat pitch angles (Bogott and Mozer, 1974; Pfitzer and Winckler, 1968). The atmosphere at the foot of the field lines maintains a loss cone anisotropy even as other magnetospheric interactions work toward removing it. We will consider then a  $f_{eo}$  which is a monotonically decreasing function of energy but with a flat pitch angle distribution. Such a distribution may be written as

$$f_{eo}(p_\perp, p_\parallel) = \frac{n_1}{\pi^{3/2} (\Delta p_\perp)^2 \Delta p_\parallel} \exp \left\{ \frac{p_\perp^2}{\Delta p_\perp^2} - \frac{p_\parallel^2}{\Delta p_\parallel^2} \right\} \quad 5.12$$

in which  $\Delta p_\perp$  and  $\Delta p_\parallel$  are parameters which determine the relative partition of energy perpendicular and parallel to the magnetic field

and  $n_1$  is an effective particle number density. It is noted that

$$2\pi \int_0^\infty \int_{-\infty}^\infty \frac{n_1}{\pi^{3/2} (\Delta p_\perp)^2 \Delta p_\parallel} \exp\left\{-\frac{p_\perp^2}{\Delta p_\perp^2} - \frac{p_\parallel^2}{\Delta p_\parallel^2}\right\} p_\perp dp_\perp dp_\parallel = n_1 \quad 5.13$$

$f_{eo}$  is not strictly speaking a true loss cone distribution in that  $f_{eo}$  is not zero for  $p_\perp$  equal to zero. This may be corrected by multiplying  $f_{eo}$  by  $(\sin\alpha)^l$  where  $\alpha$  is the pitch angle and  $l$  is an integer. This only complicates the following analysis and does not change the conclusion we will arrive at. We will return to the loss cone problem later in our considerations.

$f_{eo}$  has the property that it can be made anisotropic perpendicular to the field line (a flat distribution), isotropic and anisotropic parallel to the field line (an oblong distribution). This is effected by controlling the ratio of  $\Delta p_\perp$  to  $\Delta p_\parallel$ . We will obtain flat distributions by always having  $\Delta p_\perp > \Delta p_\parallel$ .  $f_{eo}$  also fulfills the necessary condition that it satisfy the zeroth order linearized Vlasov equation which is equation B.5 in Appendix B with the right hand side set equal to zero.

Expression 5.11 for the linear growth rate represents a balance of energy. The waves interact with particles gaining energy from some and growing and losing energy to others and damping. The contribution at each value of  $p_\perp$  is determined by the expression under the integral sign. If the expression is negative then the waves are damping and therefore losing energy, if the expression is positive the opposite is true. By use of the dispersion relation 5.1b, the coefficient of the integral in equation 5.11 may be written



$$\frac{\pi^2 \omega_{pe}^2 m_e}{|k|} \left[ \frac{2}{\omega_{pe}^2} + \frac{2\Omega_{ce} \Omega_{ci} + \Omega_{ce} \omega (1 - \frac{2m_e}{m_i})}{(\Omega_{ci} + \omega)^2 (\Omega_{ce} - \omega)^2} \right]^{-1} \quad 5.14$$

which a simple examination demonstrates is always positive definite.

The term under the integral therefore controls the sign of the contribution at each  $p_{\perp}$ . Substitution of  $f_{eo}$  into this expression yields the relation

$$\frac{-2p_{\perp}}{(\Delta p_{\perp})^2} f_{eo} \left[ 1 \pm \frac{kv_{\parallel}}{\omega} \left( \frac{\Delta p_{\perp}^2}{\Delta p_{\parallel}^2} - 1 \right) \right] \quad 5.15$$

From symmetry condition B.49,  $k/\omega$  is always positive definite for forward propagating waves. The pitch angle anisotropy that we are considering has  $\Delta p_{\perp} > \Delta p_{\parallel}$ . It is concluded then that for + resonances expression 5.15 will always be less than zero. For minus resonances the sign of expression 5.15 will be controlled by  $kv_{\parallel}/\omega$ . This tells us that plus resonances absorb energy from the waves when there is this sort of pitch angle distribution. The result is immediately suggestive of a mechanism for enhancing the high energy portion of the distribution. This is so because plus resonances only occur when (from equation 5.10)

$$\gamma = \sqrt{1 + \frac{1}{m_e^2 c^2} (p_{\perp}^2 + p_{\parallel}^2)} > \frac{\Omega_{ce}}{\omega} \quad 5.16$$

When  $\gamma$  does vary significantly from unity we are of course in the relativistic regime.

### V.E. Scaling the Various Equations

We have found that the numerous equations and relations that we have had to deal with are more easily analyzed in a scaled form. As we will be considering a numerical analysis it seemed appropriate to introduce the scaling at this point. We define the following unitless parameters

$$\begin{aligned}
 p &= \frac{p}{m_e c}, & x &= \frac{\omega}{\Omega_{ce}}, & K &= \frac{kc}{\Omega_{ce}} \\
 \beta &= \frac{v}{c}, & \gamma &= \frac{E}{m_e c^2}, & \xi_k &= \frac{E_k}{m_e c^2} \\
 \tau &= t \Omega_{ce}, & \hat{f}_{eo}(P) &= f_{eo}(P) (m_e c)^3
 \end{aligned}
 \tag{5.17}$$

which form a consistent set that makes all our equations unitless.

The dispersion relation becomes:

$$K^2 = x^2 \left( 1 + \frac{x_{pe}^2}{(1-x)(R+x)} \right) \tag{5.19}$$

with  $x_{pe}^2 = \frac{\omega_{pe}^2}{\Omega_{ce}^2}$  and  $R = \frac{m_e}{m_i}$ . The scaled total electron energy,  $\gamma$ , is related to the momentum by:

$$\gamma = (1 + p_{\perp}^2 + p_{\parallel}^2)^{1/2} \tag{5.20}$$

The scaled linear growth rate is:

$$x_{\perp}(K) = \frac{\pi^2 x_{pe}^2 \int_0^{\infty} p_{\perp} dp_{\perp} \left\{ \frac{\partial \hat{f}_{eo}}{\partial p_{\perp}} \pm \frac{K}{x} \left( \beta_{\perp} \frac{\partial \hat{f}_{eo}}{\partial p_{\parallel}} - \beta_{\parallel} \frac{\partial \hat{f}_{eo}}{\partial p_{\perp}} \right) \right\}}{|K| \left[ \frac{2K^2}{x^2} + \frac{x x_{pe}^2 (2x-1)}{(1-x)^2 (x+R)^2} \right]} \Big|_{p_{\parallel} = p_R^{\pm}}
 \tag{5.21}$$

and the resonance condition becomes:

$$p_R^{\pm} = \frac{\gamma x - 1}{K}, \quad \gamma x > 1$$

$$\frac{1 - \gamma x}{K}, \quad \gamma x < 1$$
5.22

Finally we write the scaled diffusion equation as:

$$\frac{\hat{\partial} f_{eo}}{\partial \tau} = \frac{x_{pe}^2 \Omega_{ce}^3}{n_o c^3} \int_0^{\infty} dK \frac{1}{p_{\perp}} \frac{D_k}{D_{k,p}} \left[ \frac{p_{\perp} \xi_k x_I}{(K\beta_{\parallel} + \frac{1}{\gamma} - x)^2 + x_I^2} \frac{D_k \hat{f}_{eo}}{D_{k,p}} \right.$$

$$\left. + \sum_i \frac{x_{pe}^2 \Omega_{ce}^3}{n_o c^3} \pi \frac{1}{p_{\perp}} \frac{D_k}{D_{k,p}} \left( \frac{\xi_k p_{\perp}}{|\beta_{\parallel}|} \frac{D_k}{D_{k,p}} \right) \hat{f}_{eo} \right] \Big|_{K = K_{Ri}}$$
5.23

in which the sum  $i$  runs over the resonant values of  $K$  which satisfy the resonance condition for the particular values of  $p_{\perp}$  and  $p_{\parallel}$ .

The operator  $\frac{D_k}{D_{k,p}}$  is defined by

$$\frac{D_k}{D_{k,p}} = \frac{K\beta_{\perp}}{x} \frac{\partial}{\partial p_{\parallel}} + \left( 1 - \frac{K\beta_{\parallel}}{x} \right) \frac{\partial}{\partial p_{\perp}}$$
5.24

#### V.F. The Effects of Low Density

As has been demonstrated by many authors, cyclotron waves can be quite unstable in the presence of a flat distribution. A significant amount of energy may be transferred from the particle distribution to the waves. We will demonstrate that at low post-substorm densities outside the plasmopause that these waves will grow at the expense of the pitch angle anisotropy of the subrelativistic particles enabling the near relativistic particles undergoing plus resonances to feed on the increased wave energy. This will lead to an enhancement of the high

energy portion of the spectrum.

Figure 5.2 is a diagram of  $p_R^{\pm}$  (equation 5.22) for fixed values of  $p_{\perp}$  as a function of  $x$  at a value of  $n_0 = .1/\text{cm}^3$  (figure 5.2a) and  $n_0 = .2/\text{cm}^3$  (figure 5.2b). The fixed values of  $p_{\perp}$  increase upward. Plus resonances occur above the zero line of  $p_{\parallel}$  and minus resonance occur below the zero line. For a given frequency  $x$  the resonant parallel momentum,  $p_{\parallel}$ , for a given perpendicular momentum is a higher value for positive resonance for the  $n_0 = .1/\text{cm}^3$  case. The entire form of the resonant curves show that the positive values of  $p_{\parallel}$  achieve greater values for the lower density case. The higher  $p_{\parallel}$  for fixed  $p_{\perp}$  then the higher is the energy. The conclusion is then that lower density tends to enhance the relativistic nature of the interaction. It pushes it to higher energy.

#### V.G. Energy Diffusion and the Relativistic Case

It is generally argued that diffusion in pitch angle is far more important for cyclotron resonant interactions (Kennel, 1966; Kennel, 1969) than is energy diffusion. We would like to demonstrate that energy diffusion can be quite significant in the regime we are considering. To facilitate this demonstration we will transform equation 5.23 to energy pitch angle coordinates. We take

$$\gamma = \sqrt{1 + p_{\perp}^2 + p_{\parallel}^2}$$

5.25

$$\alpha = \tan^{-1} \left( \frac{p_{\perp}}{p_{\parallel}} \right)$$

The operator  $\frac{D_k}{D_k p}$  in energy pitch angle variables is expressed

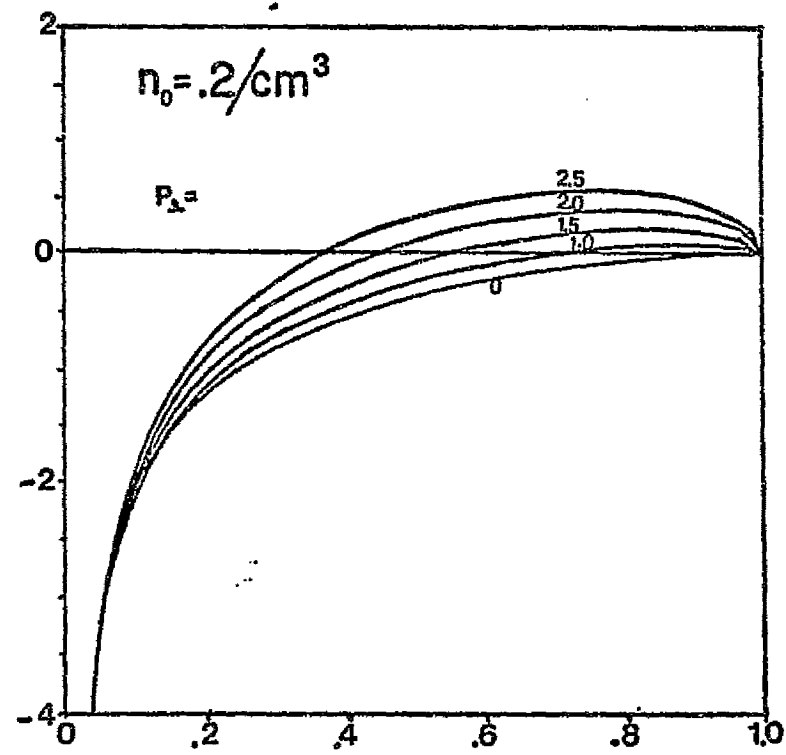
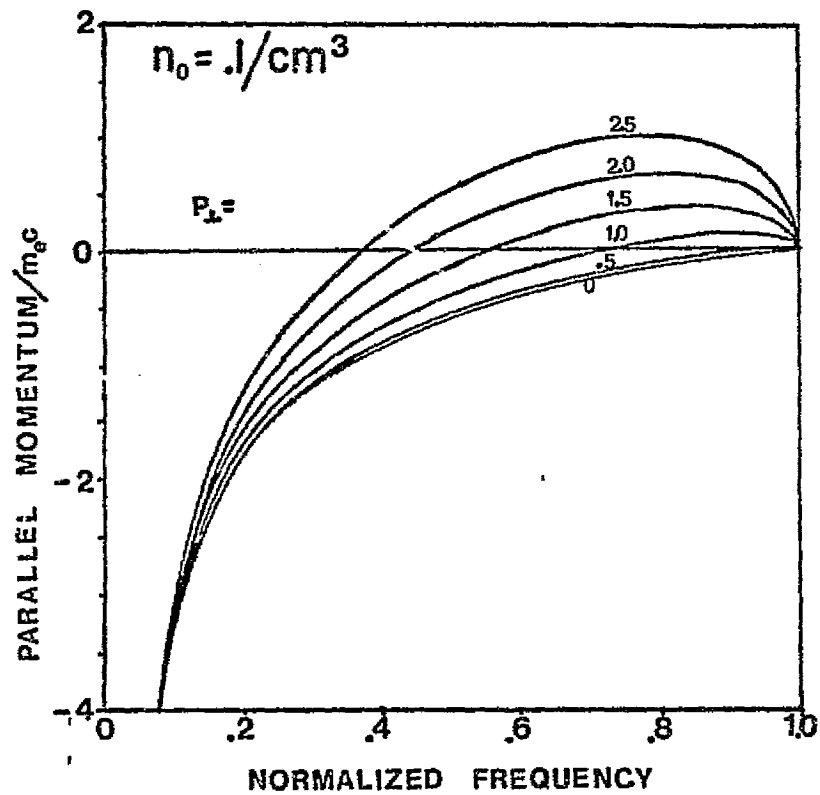


Figure 5.2. Resonant parallel momentum as a function of frequency and perpendicular momentum at two densities of electrons.

$$\frac{D_k}{D_{k^p}} = \frac{\sqrt{\gamma^2-1}}{\gamma} \sin \alpha \frac{\partial}{\partial \gamma} + \frac{\cos \alpha}{\sqrt{\gamma^2-1}} - \frac{K}{\gamma x} \frac{\partial}{\partial \alpha} \quad 5.26$$

which we write in mixed variables as:

$$\frac{D_k}{D_{k^p}} = \beta_{\perp} \frac{\partial}{\partial \gamma} + \left( \frac{\cos^2 \alpha}{p_{\parallel}} - \frac{K}{\gamma x} \right) \frac{\partial}{\partial \alpha} \quad 5.26a$$

The term  $\frac{K}{x}$  is the inverse of the scaled wave phase velocity. For  $x$  less than .1 the phase velocity is very small. Through most of the region of interest here it is of the order of 1/2 and fairly slowly varying.  $\beta_{\perp}$  has a maximum value of 1, but as the energy,  $\gamma$ , increases the term  $\frac{K}{\gamma x}$  decreases. Since most of the values are of order 1, the first term is as important as the second. The first is energy diffusion, the second is pitch angle diffusion. The importance of the first term is emphasized however, at high energy and steep pitch angle. When this is coupled with the fact that plus resonances absorb energy in wave-particle interaction we see that we may expect to see important energy diffusion taking place for relativistic particles at steep pitch angles.

#### V.H. Numerically Modeling the Quasi-linear Diffusion Equations

The equations B.50, B.45 and 5.6 form a closed set which describe to evolution in time of the distribution function,  $f(\gamma, \alpha, t)$  (or equivalently  $f(p_{\perp}, p_{\parallel}, t)$ ) and the spectral energy density  $E_k(t)$ , of cyclotron waves. It is probably impossible to determine solutions to these coupled integrodifferential equations in a closed analytic form.

We have however adopted a fairly standard procedure to determine the time behavior of  $f(\gamma, \alpha, t)$  numerically.  $f(\gamma, \alpha, t)$  is established on a numerical mesh. Equation B.45 is solved numerically for the growth rate at wave number  $K$ . An initial spectral energy density is assumed and equation 5.6 is solved numerically to determine  $E_k(t)$  after a small time increment  $\Delta t$ . With the new value of  $E_k(t)$  equation B.50 is evaluated to determine  $df/dt$  at each point on the mesh. The new  $f(\gamma, \alpha, t + \Delta t)$  is determined by

$$f(\gamma, \alpha, t + \Delta t) = f(\gamma, \alpha, t) + \frac{df}{dt} \Delta t \quad 5.27$$

With the new  $f(\gamma, \alpha, t)$  the process is repeated. This procedure can be continued as long as desired.

As formulated above the problem requires two dimensions and we have been unable to reduce it in any way to an equivalent one dimensional problem. The operator in equation (B.50) has numerous second derivatives inherent in it. Because of these second derivatives and the narrow range of instability a fine mesh was required. We were forced to smooth the first derivative in calculating second derivatives to remove obvious non-physical jagged behavior from the calculated second derivatives. The distribution function was defined over a  $91 \times 100$  (9100) point mesh and the wave spectra was defined over 200 points. The dispersion relation was also defined over a 200 point set and logarithmic interpolation used to determine values between the mesh point.

The initial distribution functions are characterized by the parameters  $n_1$ ,  $\Delta p_1$  and  $\Delta p_{11}$ . These values may be varied to establish different initial growth rates and the location of the instability in

frequency. The waves must grow up against the convective loss to a level at which they affect the distribution function sufficiently before any change occurs in the initial distribution function. Because of the very complex nature of the numerical calculations a very large amount of computation time is required. We have therefore only determined the value of  $\frac{dF}{dt}$  up to that time when  $\frac{dF}{dt}$  at any value of  $\gamma$  and  $\alpha$  becomes 1% of the initial value of  $f(\gamma, \alpha)$ . Typically we have taken the ratio of background particle density to effective superthermal particle density to be 10:1. In figures 5.3a and 5.3b we show the ratio of change of the distribution function at the 1% point for the initial conditions

$$n_0 = .1/\text{cm}^3$$

$$\frac{\omega_{pe}}{\Omega_{ce}} = .6 \quad 5.28$$

$$\frac{\Delta p_{\perp}}{\Delta p_{\parallel}} = 1.25$$

and  $\Delta p_{\perp}$  chosen to give an equivalent perpendicular temperature of 130 kev. To better represent the conditions in the magnetosphere we have established and maintained a three degree loss cone. All particles that appear in the loss cone are convected out of the interaction region. For clarity we have separated the region of negative change in the distribution (figure 5.4a) from the region of positive change in the distribution (figure 5.4b). The results very clearly demonstrate the validity of our conclusions based upon the linear analysis. The region of greatest negative change in the distribution runs in an arch from about 100 kev and 80 degrees pitch angle up to 300 kev and 75 degrees pitch angle. The waves are undergoing negative resonance with these particles



Figure 5.3—Rate of change of distribution with cold density 0.1 and anisotropy 1.25. Ration of electron frequencies 0.6.

152/W

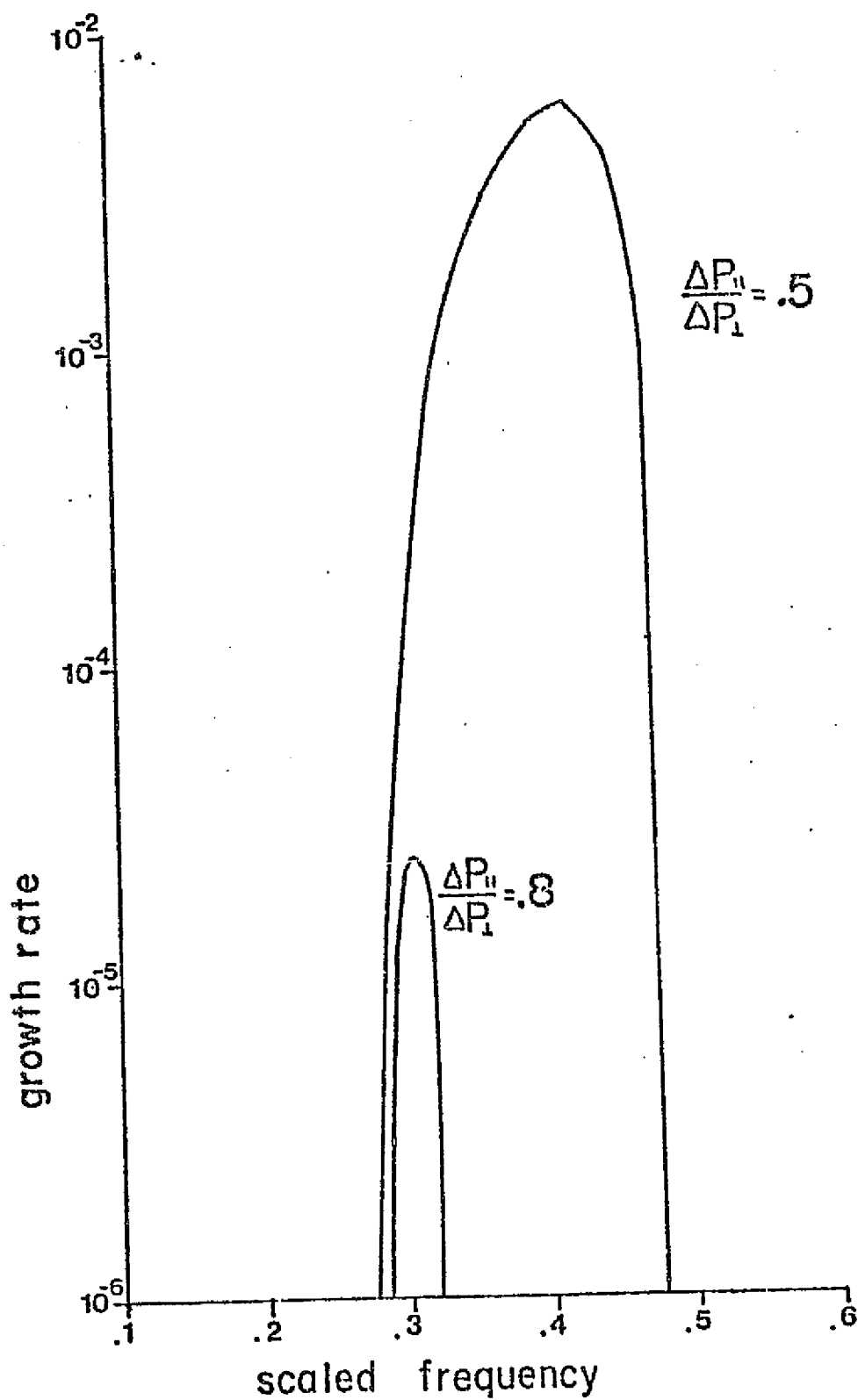


Figure 5.3. Growth rate at two anisotropy ratios.

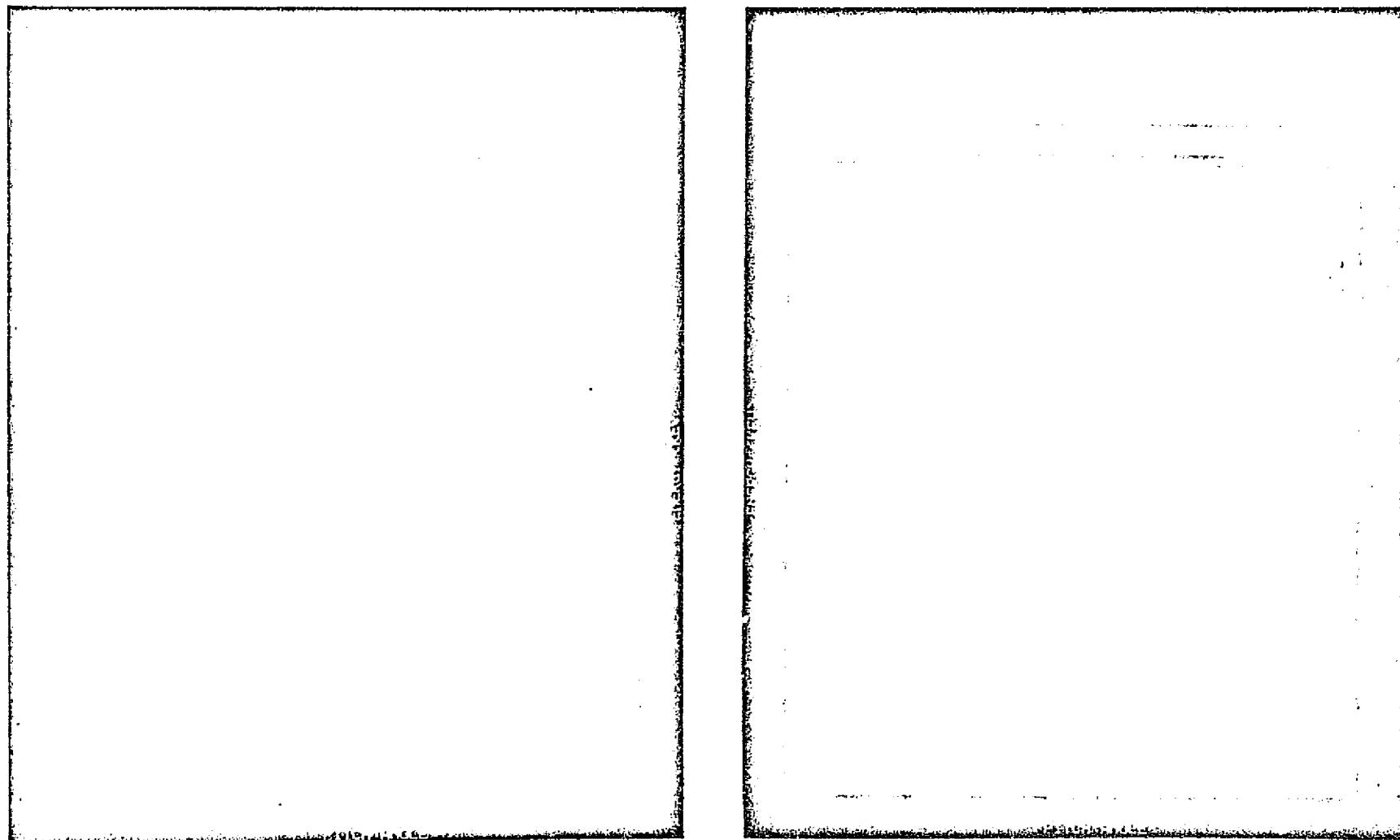


FIGURE 5.4 - RATE OF CHANGE OF DISTRIBUTION WITH COLD DENSITY 0.1 AND ANISOTROPY 1.25. RATIO OF ELECTRON FREQUENCIES 0.6.

and gaining energy from them due to their pitch angle anisotropy. The region of greatest positive growth (Figure 5.4b) runs in an arch from 300 kev and 80 degrees pitch angle up to 700 kev and 90 degree pitch angle. The waves are undergoing positive resonances with these particles and losing energy causing this region of the particle distribution to grow. As there are initially the least number of particles at high energy, the severest relative changes in the distribution will occur at high energy. The inverse growth rates minus the convective time loss yield an effective growth rate time for the instability. For the initial conditions 5.28 this time is on the order of 1 second.

The numerical results are in very good qualitative agreement with the experimental observations described in Chapter III. The relativistic particles are enhanced by the lower energy particles which should precipitate into the loss cone in a time like one over the growth rate (here about 1 second). We have of course varied the initial conditions to guarantee that the results would closely approximate to observations. A value of  $n_1$  of  $.01/\text{cm}^3$  (.1 of  $n_0$ ) yields the right magnitude for the observed integral fluxes. The fact that a set of initial conditions for this problem could be chosen that approximate the observations maybe quite fortuitous in that we have only attempted a very simplistic (though mathematically complex) model interaction. It is really the qualitative features which may carry over into a more complete model incorporating the complexities of drifting trapped particles with possible sources and sinks. The spectral shape of the precipitated particles as well as the time behavior will depend strongly on the rest

of the model. The point we have made here is that cyclotron resonant interactions will lead to the enhancement of the relativistic electron population at times of low electron density.

#### V.I. Conclusion

We have not examined the precipitation of the relativistic electrons directly, but only inferred that they should precipitate. A complete analysis should include a consideration of the electrostatic loss cone instability (F.W. Perkins, 1959) as well as possible parasitic interaction with background ion-cyclotron turbulence. It is possible to conceive of the foregoing theory as complementary to that presented by R. M. Thorne (1974). Thorne proposed a mechanism for producing REPs in which drifting protons injected on the nightside of the earth during a magnetic substorm would enter a so-called detached plasma region and would undergo strong pitch angle diffusion amplifying ion-cyclotron waves. The ion-cyclotron waves would in turn interact with very energetic electrons causing them to precipitate (move into the loss cone). The mechanism of Thorne (1974) does not explain the production of the energetic electrons but rather assumes they are present in the trapped particle flux. The theory does imply strong proton precipitation in association with the electron precipitation. Our theory explains the production of energetic electrons and does not require that there be accompanying protons (this agrees with our observations). In addition, our theory strongly couples the relativistic electrons to the precipitation of the lower energy electrons which also agrees very well with our observations. The growth of the relativistic electron population through the anomalous doppler interaction on the other hand does provide an

input of relativistic electrons for the theory of Thorne (1974) and in that sense the two theories complement each other.

There are two features of the REP theory which stand out as obvious indicators of its possible validity. The first is the association of very low cold plasma density at the equator with an ongoing REP ( $\omega_{pe} < \Omega_{ce}$ ) and the second a fairly narrow band of strong whistler turbulence again near the equator. In our numerical model the magnetic fields in the turbulence reached a level of about 10 mG over a band about 500 Hz wide before there was any appreciable change in the high energy portion of the distribution. Both of these measurements would have to be made on board a satellite. As there are presently and will be in the future satellites instrumented to make such measurements we may look forward to such measurements being made during an REP.

## APPENDIX A-1 - MODELING THE X-RAY PRODUCTION IN THE SHIELDING

The experimental data on x-ray production to be found in the literature is displayed in many different forms and not all of it was directly useable for our purposes. We have rescaled data taken from Berger and Seltzer (1968) and Rester, Dance and Davidson (1970). Figure A.1 is a composite of this data for copper or materials with  $z$  values very close to copper. The x-ray spectra emergent between 0 and 10 degrees for electrons of various energies normally incident on targets of thickness  $R$  (the particle range as defined in section 2.D) is plotted in units of photons/(keV x ster x electrons) for electron energies between 200 KeV and 2.0 MeV. For purposes of this calculation we extrapolated those energies not actually covered by the data.

Given the range  $R$  for various energy electrons the graphs in Figure A.1 yield the x-ray spectra at the depth  $R$ , at which the electron cones to rest. The x-rays are then propagated the remaining distance through the brass,  $d - R_0$ , where  $d$  is the thickness of the brass. The spectra is attenuated according to the law

$$I(E,E) = I_0(E,E_0) e^{-\mu_E(d-R_0)} \quad (A.1)$$

with  $I_0(E,E_0)$  the intensity of x-rays of energy  $E$  at  $R_0$  and  $E_0$  is the energy of the original electrons producing the x-rays. The coefficients  $\mu_E$  are tabulated in Liepunskii et al (1965) for numerous materials. The x-rays are attenuated again by the same law through the lead. For each incident electron energy there is an x-ray spectrum  $S(E,E)$  emergent from the lead. The x-ray spectrum is then folded with

157

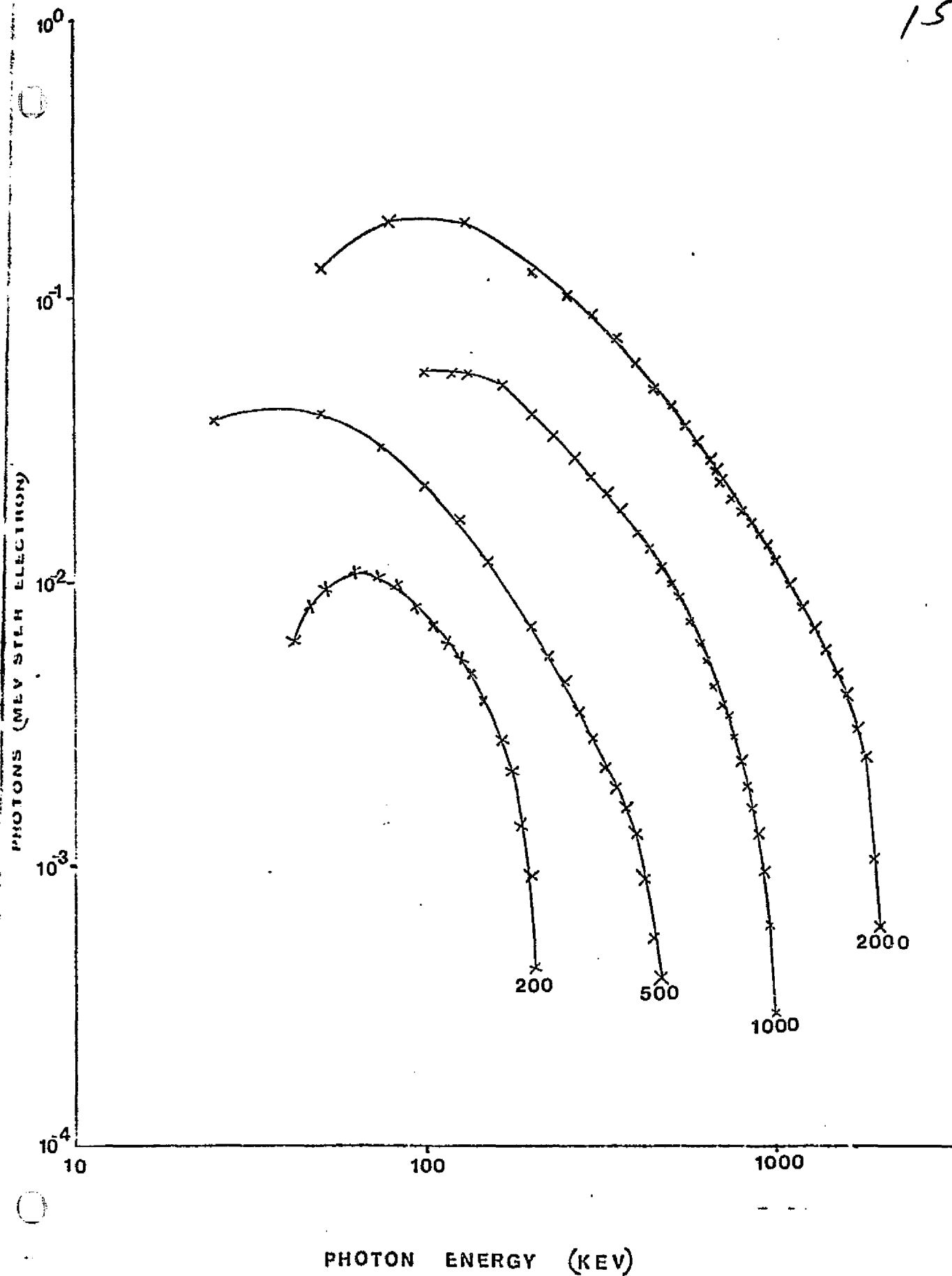


FIGURE A.1. BREMSSTRAHLUNG PRODUCTION IN TARGETS OF DEPTH  $R_0$  SCALED FROM BERGER AND SELTZER, 1968 AND RESTER ET AL, 1970



the electron spectrum  $F = \frac{J_0}{E_0} e^{-E/E_0}$ , so that the spectrum incident on the detector is given by

$$S(E) = \int S(E,E) F(E) dE \quad (\text{A.2})$$

The spectrum seen by the silicon detector will then be determined by the relation

$$S(E) = S(E)(1 - e^{-\mu_E \delta}) \quad (\text{A.3})$$

where  $\mu_E$  is the appropriate coefficient for silicon also tabulated in Leipunskii et al (1965) and  $\delta$  is the detector thickness.

The results of our model calculations are described in section II.2 of the text.

APPENDIX A-2 - ENERGY SCALING PARAMETER,  $E_r$

Many authors have scaled the transmission properties of thin foils for electrons in terms of an energy parameter, normally called  $E_r$  or  $E_c$ , which makes the transmission curve nearly independent of the foil thickness. This type of scaling is used through much of the literature on ionizing radiation and its various properties. Kanter (1961) credits Wecker (1941) with being the first experimenter to notice this scaling property. Using Wecker's definition, Kanter's  $E_c$  is determined by drawing the tangent to the transmission curve at the point of steepest slope and taking the tangent's intercept with the energy axis as the value of  $E_c$ .  $E_c$  is supposed to be that energy at which transmission just begins.

Berger and Seltzer in their various articles (see Bibliography) report the results of computer simulation for which the above definition would be a bit awkward. They have adopted the scaling energy  $E_r$  (range energy) which is defined as that incident energy which yields a total electron path length,  $r$ , in using the continuous slowing down approximation (CSA). The values of  $E_c$  and  $E_r$  are very close with  $E_c$  generally being a bit smaller than  $E_r$ . We have chosen to use  $E_r$  for all of our purposes since it is an easily obtained quantity. The data we have taken from Kanter (1961) (Figure 1.16a) has been rescaled from  $E_c$  to  $E_r$ .

APPENDIX A-3 - ANGULAR RESPONSE OF THE COLLIMATOR

For monodirectional flux of particles of uniform intensity over the aperture of the collimator it is simple to derive the response from geometrical consideration than from a vector analysis. We consider the flux as making a direction  $\alpha$  with the normal to the plane of the back aperture (and front aperture) of the collimator. (see Figure A-2). The front aperture will either obstruct the back aperture, partially shade it or have it completely exposed. The exposed area of the back of the collimator times the  $\cos\alpha$  will constitute the response of the collimator. For angles greater than 11.35 degrees the back aperture is completely shaded and the response is zero. For angles less than 3.60 degrees the back aperture is completely exposed and the response is simply  $\cos\alpha$  (effectively 1). For angles between 3.6 degrees and 11.35 degrees by simply projecting the shadow of the front aperture on the back aperture it may be determined that

$$R(\alpha) = \frac{1}{2} \pi r_1^2 - \int_{-x_i}^{x_i} \left( \sqrt{r_2^2 - x^2} - \sqrt{r_1^2 - x^2} \right) \cos\alpha \, dx$$

$$-h \sin\theta < \bar{x}_i \qquad \theta_{min} < \theta < \theta_p$$

$$R(\alpha) = \int_{-x_i}^{x_i} \left( \sqrt{r_2^2 - x^2} - \sqrt{r_1^2 - x^2} \right) \cos\alpha \, dx - h \sin\alpha \, x_i$$

$$\theta_p < \theta < \theta_{max}$$

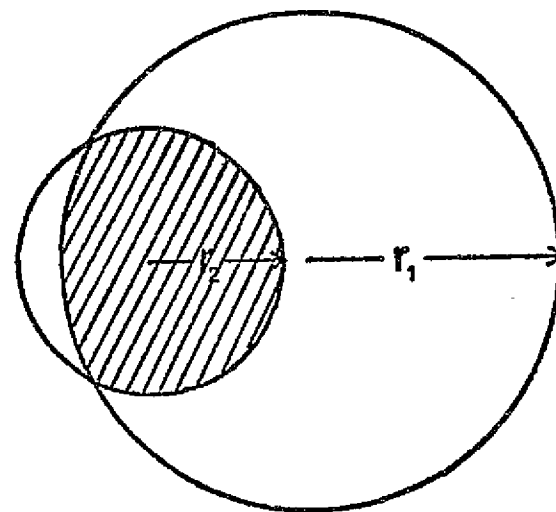
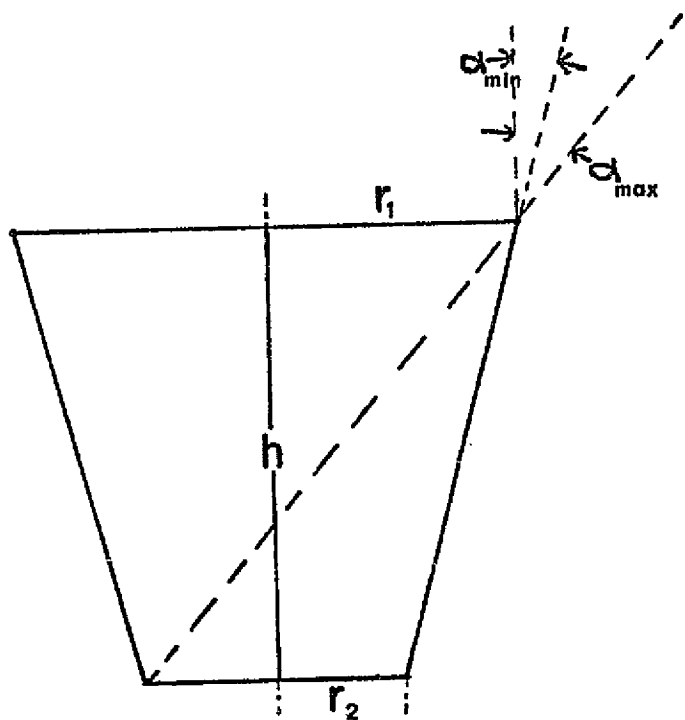


FIGURE A.2. GEOMETRY FOR THE ANGULAR RESPONSE OF THE COLLIMATOR.

$$x_i = \sqrt{r_1^2 + \left\{ \frac{h^2 \sin^2 \alpha + (r_1^2 - r_2^2)^2 \cos^2 \alpha}{2h \sin \alpha \cos \alpha} \right\}^2}$$

$$r_1 > r_2$$

The integrals may be easily performed giving the relations

$$R(\alpha) = \frac{\pi r_1^2}{2} \cos \alpha - \left\{ x_i \left( \sqrt{r_2^2 - x_i^2} - \sqrt{r_1^2 - x_i^2} \right) - r_2^2 \sin^{-1} \left( \frac{x_i}{r_2} \right) - r_1^2 \sin^{-1} \left( \frac{x_i}{r_1} \right) \right\} \\ \cos \alpha - 2hx_i \sin \alpha \quad \theta_{\min} < \theta < \theta_p$$

$$R(\alpha) = \left\{ x_i \left( \sqrt{r_2^2 - x_i^2} - \sqrt{r_1^2 - x_i^2} \right) - r_2^2 \sin^{-1} \left( \frac{x_i}{r_2} \right) - r_1^2 \sin^{-1} \left( \frac{x_i}{r_1} \right) \right\} \cos \alpha \\ - < x_i h \sin \alpha \quad d_p < d < d_{\max}$$

and  $\alpha_p$  is the angle at which the projected front aperture intercepts the two ends of the diagonal of the back aperture.

APPENDIX B - DERIVATION OF A FULLY RELATIVISTIC QUASILINEAR  
DIFFUSION EQUATION FOR CYCLOTRON RESONANT INTERACTIONS

We followed the quasilinear formalism outlined in Krall and Trivelpiece (Krall and Trivelpiece, 1973). We will assume that there is an interaction region centered at the equator of sufficient uniformity and size to define a uniform static magnetic field  $B_0$  and a spacially smooth distribution function

$$f_{\alpha 0}(\underline{p}, t) = \frac{1}{V} \int d^3x f_{\alpha}(x, \underline{p}, t) \quad (B.1)$$

so that perturbations satisfy the relation

$$f_{\alpha}(x, \underline{p}, t) = f_{\alpha 0}(\underline{p}, t) + f_{\alpha 1}(x, \underline{p}, t) \quad (B.2)$$

and therefore

$$\frac{1}{V} \int d^3x f_{\alpha 1}(x, \underline{p}, t) = 0 \quad (B.2a)$$

We will make the same assumption for all perturbed field quantities

$$\underline{B}_0 = \frac{1}{V} \int d^3x \underline{B} \quad (B.3)$$

$$0 = \frac{1}{V} \int d^3x \underline{E}$$

with

$$\underline{B}(\underline{x}, t) = \underline{B}_0 + \underline{B}_1(\underline{x}, t)$$

$$\underline{E}(\underline{x}, t) = \underline{E}_1(\underline{x}, t)$$

We substitute these values in to the Vlasov equation and expand so that

$$\begin{aligned} \frac{\partial f_{\alpha 0}}{\partial t} + q_{\alpha} \left( \frac{\underline{v} \times \underline{B}_0}{c} \right) \cdot \frac{\partial f_{\alpha 0}}{\partial \underline{p}} + \frac{\partial f_{\alpha 1}}{\partial t} + \underline{v} \cdot \frac{\partial f_{\alpha 1}}{\partial \underline{x}} + q_{\alpha} \left( \frac{\underline{v} \times \underline{B}_0}{c} \right) \cdot \frac{\partial f_{\alpha 1}}{\partial \underline{p}} = \\ - q_{\alpha} \left( \underline{E}_1 + \frac{\underline{v} \times \underline{B}_1}{c} \right) \cdot \frac{\partial f_{\alpha 0}}{\partial \underline{p}} - q_{\alpha} \left( \underline{E}_1 + \frac{\underline{v} \times \underline{B}_1}{c} \right) \cdot \frac{\partial f_{\alpha 1}}{\partial \underline{p}} \end{aligned} \quad (\text{B.4})$$

We take the spacial average and use condition B.2.a

$$\left[ \frac{\partial}{\partial t} + q_{\alpha} \frac{\underline{v} \times \underline{B}_0}{c} \cdot \frac{\partial}{\partial \underline{p}} \right] f_{\alpha 0} = - \frac{q_{\alpha}}{V} \int d^3x \left[ \left( \underline{E}_1 + \frac{\underline{v} \times \underline{B}_1}{c} \right) \cdot \frac{\partial f_{\alpha 1}}{\partial \underline{p}} \right] \quad (\text{B.5})$$

Equation B.5 tells us that the time derivative of the spacial uniform distribution function is proportional to a product of perturbed quantities and is itself therefore a second order correction. The quasi-linear approximation consists in solving the first order equations for perturbed quantities and substituting these into equation B.5 to determine  $\frac{df_{\alpha 0}}{dt}$ . Dropping second order terms then in equation B.4 we have the standard perturbed Vlasov equation

(B.6)

$$\left[ \frac{\partial}{\partial t} + \underline{v} \cdot \frac{\partial}{\partial \underline{x}} + q_{\alpha} \left( \frac{\underline{v} \times \underline{B}_0}{c} \right) \cdot \frac{\partial}{\partial \underline{p}} \right] f_{\alpha 1} = - q_{\alpha} \left( \underline{E}_1 + \frac{\underline{v} \times \underline{B}_1}{c} \right) \cdot \frac{\partial f_{\alpha 0}}{\partial \underline{p}}$$

As we wish to retain all relativistic terms we solve this completely

here using the method of characteristics which can be found in most standard textbooks on Plasma Physics (see Krall and Trivelpiece).

One recognizes that equation B.6 may be written

$$\frac{df_{\alpha 1}}{dt} = -q_{\alpha} \left( \underline{E}_1 + \frac{\underline{v} \times \underline{B}_1}{c} \right) \cdot \frac{\partial f_{\alpha 0}}{\partial \underline{p}} \quad (\text{B.7})$$

where the operation  $\frac{d}{dt}$  is evaluated along the trajectories of unperturbed particles in the uniform magnetic field. We integrate both sides of B.7 from  $-\infty$  to  $t$  and assume that the perturbed quantities were zero at  $-\infty$ . We then have that

$$f_{\alpha 1}(t, \underline{x}) = -q_{\alpha} \int_{-\infty}^t \left( \underline{E}'_1 + \frac{\underline{v}' \times \underline{B}'_1}{c} \right) \cdot \frac{\partial f_{\alpha 0}}{\partial \underline{p}'} dt' \quad (\text{B.8})$$

where we must remember that  $\underline{E}_1$  and  $\underline{B}_1$  are functions of  $\underline{x}'$ ,  $\underline{v}'$  and  $\underline{p}$  the parameters of the unperturbed trajectories. We now choose  $\underline{x}'$ ,  $\underline{v}'$  and  $\underline{p}'$  in such a manner that

$$\begin{aligned} \underline{x}'(t'=t) &= \underline{x} \\ \underline{v}'(t'=t) &= \underline{v} \\ \underline{p}'(t'=t) &= \underline{p} \end{aligned} \quad (\text{B.9})$$

We take  $\hat{k}$  along the magnetic field and  $\hat{\phi}$  as the azimuthal direction about the field with

$$\begin{aligned} \underline{v} &= v_{\parallel} \hat{k} + v_{\perp} \hat{\phi} \\ \underline{p} &= p_{\parallel} \hat{k} + p_{\perp} \hat{\phi} \end{aligned}$$



then

$$\begin{aligned}
 z' &= z + v_{\parallel} (t' - t) \\
 x' &= x - \frac{v_{\perp}}{\omega_{c\alpha}} \sin(\phi - \omega_{c\alpha} (t' - t)) + \frac{v_{\perp}}{\omega_{c\alpha}} \sin\phi \\
 y' &= y + \frac{v_{\perp}}{\omega_{c\alpha}} \cos(\phi - \omega_{c\alpha} (t' - t)) - \frac{v_{\perp}}{\omega_{c\alpha}} \cos\phi \\
 p'_x &= p_x \cos(\phi - \omega_{c\alpha} (t' - t)) \\
 p'_y &= p_y \sin(\phi - \omega_{c\alpha} (t' - t))
 \end{aligned} \tag{B.10}$$

where  $\omega_{c\alpha}$  is the cyclotron frequency for the particle of mass  $m_{\alpha}$  such that

$$\omega_{c\alpha} = \frac{q B_0}{\gamma m_{\alpha} c} \tag{B.11}$$

and  $\gamma \equiv (1 - \frac{v^2}{c^2})^{-1/2}$  is the relativistic mass correction.

If we now replace all functions of  $x$  and  $x'$  in B.8 by their Fourier integral representations such that

$$f_{\alpha l k}(t, \underline{x}) = \frac{1}{(2\pi)^3} \int d^3 k e^{i \underline{k} \cdot \underline{x}} f_{\alpha l k}(t) \tag{B.12}$$

and change the order of integration of  $\underline{k}$  and  $t$  equation B.8 becomes

$$f_{\alpha l k}(\underline{p}, t) e^{i \underline{k} \cdot \underline{x}} = -q \int_{-\infty}^t dt' \left( \underline{E}_{\perp l k} + \frac{\underline{v} \times \underline{B}_{\perp l k}}{c} \right) \cdot \frac{\partial f_{\alpha 0}}{\partial \underline{p}} e^{i \underline{k} \cdot \underline{x}'} dt' \tag{B.13}$$

We repeat the procedure over all functions of  $t$  and  $t'$  with

$$f_{\alpha 1k}(\underline{p}, t) = \frac{1}{(2\pi)} \int d\omega e^{-i\omega t} f_{\alpha 1k}(\underline{p}, \omega) \quad (\text{B.14})$$

and divide the resulting equation by  $e^{i\mathbf{k} \cdot \underline{x} - i\omega k}$ . Equation B.13 now becomes

$$f_{\alpha 1k}(\underline{p}, \omega) = -q \int_{-\infty}^t dt' \left( \frac{\underline{E}_{1k}}{\omega}(\omega) + \frac{v \times \underline{B}_{1k}(\omega)}{c} \right) \cdot \frac{\partial f_{\alpha 0}}{\partial \underline{p}} e^{i\mathbf{k} \cdot (\underline{x}' - \underline{x})} e^{-i\omega(t' - t)} dt' \quad (\text{B.15})$$

It is convenient to let  $t' - t = \tau$  and  $\underline{x}' - \underline{x} = \Delta \underline{x}$  in equation B.15. The orientation of the  $x$  and  $y$  axes is arbitrary so that we may let  $k_x = k$  and  $k_y = 0$  without any loss of generality.

The term in the exponential on the right side of B.15 is expanded

$$\underline{k} \cdot \Delta \underline{x}(\tau) - \omega \tau = \frac{k v_{\perp}}{\omega c \alpha} (\sin \phi - \sin(\phi - \omega \frac{\tau}{c \alpha})) + (k_{\parallel} v_{\parallel} - \omega) \tau \quad (\text{B.16})$$

To evaluate the integral the vector term must be expanded. Using Maxwell's equations the perturbed quantity  $\underline{B}_{1k}(\omega)$  can be related to the perturbed quantity  $\underline{E}_{1k}(\omega)$

$$\underline{B}_{1k}(\omega) = \frac{k \times \underline{E}_{1k}(\omega)}{\omega} \quad (\text{B.17})$$

Equation (B.17) is substituted into (B.15) and the vector product expanded, yielding the result

(B.18)

$$f_{\alpha l k}(\underline{p}, \omega) = -q \int_{-\infty}^0 dt \left\{ E_{x l k}(\omega) \left[ \frac{v'_x}{\omega} k_{\parallel} \frac{\partial f_{\alpha 0}}{\partial p_{\parallel}} + \left( 1 - \frac{v_{\parallel} k_{\parallel}}{\omega} \right) 2 \frac{\partial f_{\alpha 0}}{\partial p_{\perp}^2} p'_x \right] + \right. \\ E_{y l k}(\omega) \left[ \frac{v'_y}{\omega} k_{\parallel} \frac{\partial f_{\alpha 0}}{\partial p_{\parallel}} + \left( 1 - \frac{v_{\parallel} k_{\parallel}}{\omega} \right) 2 \frac{\partial f_{\alpha 0}}{\partial p_{\perp}^2} p'_y \right] + E_{z l k}(\omega) \left[ \frac{2v_{\parallel}}{\omega} \frac{\partial f_{\alpha 0}}{\partial p_{\perp}^2} k_{\perp} p'_x - \right. \\ \left. \left. \frac{v'_x}{\omega} k_{\perp} \frac{\partial f_{\alpha 0}}{\partial p_{\parallel}} + \frac{\partial f_{\alpha 0}}{\partial p_{\parallel}} \right] \right\} e^{i \underline{k} \cdot \underline{\Delta x}} e^{-i \omega \tau}$$

where we have let

$$\frac{\partial f_{\alpha 0}}{\partial p'_x} = \cos(\phi - \omega_{c\alpha} \tau) \frac{\partial f_{\alpha 0}}{\partial p_{\perp}} \quad (B.19)$$

$$\frac{\partial f_{\alpha 0}}{\partial p'_y} = \sin(\phi - \omega_{c\alpha} \tau) \frac{\partial f_{\alpha 0}}{\partial p_{\perp}}$$

The integrals in equation (B.18) are only of three types which may be evaluated using one of the three following relations which may be found in Watson (1965).

$$e^{i b \sin \theta} = \sum_{n=-\infty}^{\infty} J_n(b) e^{i n \theta} \quad (B.20)$$

$$\sin \theta e^{i b \sin \theta} = -i \sum_{n=-\infty}^{\infty} 1/2 (J_{n-1}(b) - J_{n+1}(b)) e^{i n \theta}$$

(B.20 cont.)

$$\cos\theta e^{ibs\sin\theta} = \sum_{n=-\infty}^{\infty} \frac{J_n(b)}{b} n e^{in\theta}$$

Where  $J_n(b)$  is the Bessel function of the first kind of order  $n$ . The three types of integrals are then written

(B.21)

$$\begin{aligned} & \int_{-\infty}^0 d\tau e^{ibs\sin\phi} e^{-ibs\sin(\phi-\omega_{c\alpha}\tau)} e^{i(k_{\parallel}v_{\parallel}-\omega)\tau} \\ &= e^{ibs\sin\phi} \sum_{n=-\infty}^{\infty} \int_{-\infty}^0 d\tau J_n(b) e^{-in\phi} e^{i(k_{\parallel}v_{\parallel}+n\omega_{c\alpha}-\omega)\tau} \\ & \int_{-\infty}^0 d\tau e^{ibs\sin\phi} e^{-ibs\sin(\phi-\omega_{c\alpha}\tau)} e^{i(k_{\parallel}v_{\parallel}-\omega)\tau} \sin(\phi-\omega_{c\alpha}\tau) = \\ & i e^{ibs\sin\phi} \sum_{n=-\infty}^{\infty} \int_{-\infty}^0 \frac{1}{2} (J_{n-1}(b) - J_{n+1}(b)) e^{-in\phi} e^{i(k_{\parallel}v_{\parallel}+n\omega_{c\alpha}-\omega)\tau} d\tau \\ & \int_{-\infty}^0 d\tau e^{ibs\sin\phi} e^{-ibs\sin(\phi-\omega_{c\alpha}\tau)} e^{i(k_{\parallel}v_{\parallel}-\omega)\tau} \cos(\phi-\omega_{c\alpha}\tau) = \\ & e^{ibs\sin\phi} \sum_{n=-\infty}^{\infty} \int_{-\infty}^0 d\tau \frac{J_n(b)}{b} n e^{-in\phi} e^{i(k_{\parallel}v_{\parallel}+n\omega_{c\alpha}-\omega)\tau} \end{aligned}$$

where we have taken  $b = \frac{k_{\parallel} v_{\parallel}}{\omega_{c\alpha}}$ .

The quantities  $\omega$  is complex and is taken as

$$\omega = \omega_R + i\omega_I \quad (\text{B.22})$$

In the case that  $\omega_I > 0$ , so that  $e^{\omega_I t} = 0$  at  $t = -\infty$ , the three expressions become

$$-ie^{i b \sin \phi} \sum_{n=-\infty}^{\infty} \frac{J_n(b) e^{-in\phi}}{k_{\parallel} v_{\parallel} + n\omega \quad c\alpha^{-\omega}} \quad (\text{B.23})$$

$$e^{i b \sin \phi} \sum_{n=-\infty}^{\infty} \frac{1}{2} \frac{(J_{n-1}(b) - J_{n+1}(b)) e^{-in\phi}}{k_{\parallel} v_{\parallel} + n\omega \quad c\alpha^{-\omega}}$$

$$-ie^{i b \sin \phi} \sum_{n=-\infty}^{\infty} \frac{\frac{J_n(b)}{b} n e^{-in\phi}}{k_{\parallel} v_{\parallel} + n\omega \quad c\alpha^{-\omega}}$$

At this point we simplify our considerations greatly by considering only parallel propagating transverse waves and let  $k_{\perp} = 0$  and noting that

$$\frac{nJ_n(b)}{b} = \frac{1}{2} (J_{n-1}(b) + J_{n+1}(b))$$

and

$$J_n(0) = 0 \quad n \neq 0$$

$$J_n(0) = 1 \quad n = 0$$

Equation B.18 may then be reduced to

$$f_{\alpha k}(\underline{p}, \omega) = -q \left\{ \frac{1}{2} o_1 \left[ \frac{-iE_x + E_y}{k_{||} v_{||} + \omega c\alpha} e^{-i\phi} \right] + \frac{1}{2} o_1 \left[ \frac{-iE_x - E_y}{k_{||} v_{||} - \omega c\alpha} e^{i\phi} \right] \right\} \quad (\text{B.24})$$

with

$$o_1 = \frac{k_{||} v_{||}}{\omega} \frac{\partial f_{\alpha 0}}{\partial p_{||}} + \left(1 - \frac{k_{||} v_{||}}{\omega}\right) 2p_{\perp} \frac{\partial f_{\alpha 0}}{\partial p_{\perp}^2}$$

Using the standard transformation for left and right handed circularly polarized waves we let

$$\begin{aligned} E_R &= E_x + iE_y \\ E_L &= E_x - iE_y \end{aligned} \quad (\text{B.25})$$

and

$$f_{\alpha k}(\underline{p}, \omega) = \frac{iq}{2} o_1 \left\{ \frac{E_R e^{-i\phi}}{k_{||} v_{||} + \omega c\alpha} + \frac{E_L e^{i\phi}}{k_{||} v_{||} - \omega c\alpha} \right\} \quad (\text{B.26})$$

$f_{\alpha k}(\underline{p}, \omega)$  from equation B.26 now defines the first order perturbed quantity which is now placed back in equation (B.5) to determine the second order time derivative of the initial spacially averaged distribution function. Substituting the Fourier integrals on the right hand side of equation (B.5) we have

$$\frac{df_{\alpha 0}}{dt} = -\frac{q\alpha}{V(2\pi)^3} \iint d^3k d^3k' \int (E_{\perp k}(\omega) + \frac{v \times B_{\perp k}(\omega)}{c}) \quad (\text{B.27})$$

(B.27 cont.)

$$\cdot \frac{\partial f_{\alpha 1 k'}(\omega)}{\partial \underline{p}} e^{i \underline{k} \cdot \underline{x}} e^{i \underline{k}' \cdot \underline{x}} d^3 x$$

and we identify

$$\frac{1}{(2\pi)^3} \int e^{i \underline{k} \cdot \underline{x}} e^{i \underline{k}' \cdot \underline{x}} d^3 x = \delta(\underline{k} + \underline{k}')$$

with the result

(B.28)

$$\frac{df_{\alpha 0}}{dt} = - \frac{a}{(2\pi)^3} \int \frac{d^3 k}{v} \left( \underline{E}_{-1k}(\omega) + \frac{v \times \underline{B}_{-1k}(\omega)}{c} \right) \cdot \frac{\partial f_{\alpha 1-k}(\omega)}{\partial \underline{p}}$$

Since we require that  $f_{\alpha}$  be real, then

$$f_{\alpha 1-k} = f_{\alpha 1k}^*$$

Again we expand the vector product replacing  $\underline{B}_{-1k}(\omega)$  in terms of  $\underline{E}_{-1k}(\omega)$ . Using the relation

$$\underline{E}_x \cos \phi + \underline{E}_y \sin \phi = \frac{1}{2} \left[ \underline{E}_R e^{-i\phi} + \underline{E}_L e^{i\phi} \right] \quad (\text{B.29})$$

the vector product becomes

$$\frac{1}{2} \left\{ \underline{E}_R e^{-i\phi} (A - iB) + \underline{E}_L e^{i\phi} (A + iB) \right\} f_{\alpha 1k}^*(\omega) \quad (\text{B.30})$$

with the operators

$$A = \left( 1 - \frac{kv_{\parallel}}{\omega} \right) \frac{\partial}{\partial p_{\perp}} + \frac{kv_{\parallel}}{\omega} \frac{\partial}{\partial p_{\parallel}} \quad (\text{B.31})$$

(B.31 cont.)

$$B = \left(1 - \frac{k_{\parallel} v_{\parallel}}{\omega}\right) \frac{1}{p_{\perp}} \frac{\partial}{\partial \phi}$$

Evaluating the terms in B.31 with equation B.26 yields

(B.32)

$$\begin{aligned} \frac{1}{2} E_L e^{+i\phi} (A+iB) f_{\alpha 1k}^*(\omega) &= \frac{-iq}{4} \left\{ \left[ A - \frac{1}{p_{\perp}} \left(1 - \frac{k_{\parallel} v_{\parallel}}{\omega}\right) \right] \frac{E_R^* E_L e^{2i\phi}}{k_{\parallel} v_{\parallel} + \omega_{c\alpha} - \omega} \right. \\ &\quad \left. + \left[ A + \frac{1}{p_{\perp}} \left(1 - \frac{k_{\parallel} v_{\parallel}}{\omega}\right) \right] \frac{|E_L|^2}{k_{\parallel} v_{\parallel} - \omega_{c\alpha} - \omega} \right\} A f_{\alpha 0} \\ \frac{1}{2} E_R e^{-i\phi} (A-iB) f_{\alpha 1k}^*(\omega) &= \frac{-iq}{4} \left\{ \left[ A + \frac{1}{p_{\perp}} \left(1 - \frac{k_{\parallel} v_{\parallel}}{\omega}\right) \right] \frac{|E_R|^2}{k_{\parallel} v_{\parallel} + \omega_{c\alpha} - \omega} \right. \\ &\quad \left. + \left[ A - \frac{1}{p_{\perp}} \left(1 - \frac{k_{\parallel} v_{\parallel}}{\omega}\right) \right] \frac{E_L^* E_R e^{-2i\phi}}{k_{\parallel} v_{\parallel} - \omega_{c\alpha} - \omega} \right\} A f_{\alpha 0} \end{aligned}$$

The parameter  $\phi$  was the arbitrary initial phase angle between  $p_{\perp}$  and the x-axis. This will be assumed to be a random quantity. We will integrate both sides of equation (B.28) then over  $\phi$  from 0 to  $2\pi$  and divide both sides by  $2\pi$

(B.33)

$$\frac{df_{\alpha 0}}{dt} = \frac{-q}{2\pi} \int_0^{2\pi} \int \left( E_{\perp 1k}(\omega) + \frac{v_{\perp} B_{\perp 1k}(\omega)}{c} \right) \cdot \frac{\partial f_{\alpha 1k}^*(\omega)}{\partial p_{\perp}} d^3 k d\phi$$

and note that  $\int_0^{2\pi} e^{+2i\phi} d\phi = 0$ .

We now have



$$\frac{df_{\alpha 0}}{dt} = \frac{2\pi i q^2}{8\pi V} \int \frac{d^3 k}{(2\pi)^3} \left[ A + \frac{1}{P_1} \left( 1 - \frac{k_{\parallel} v_{\parallel}}{\omega} \right) \right] \left[ \frac{|E_R|^2}{k_{\parallel} v_{\parallel} + \omega_{c\alpha} - \omega} + \frac{|E_L|^2}{k_{\parallel} v_{\parallel} - \omega_{c\alpha} - \omega} \right] A f_0 \quad (\text{B.34})$$

We will use the standard definition of the spectral energy density (Krall and Trivelpiece, 1973) with

$$\left\langle \frac{|E|^2}{8\pi} \right\rangle = \frac{1}{V} \int \frac{\vec{E}_k \cdot \vec{E}_k^*}{8\pi} \frac{d^3 k}{(2\pi)^3} = \int \epsilon_k d^3 k \quad (\text{B.35})$$

and from the definition B.25

$$|E_R|^2 = |E_L|^2 = E_x^2 + E_y^2$$

we may finally write

$$\frac{df_{\alpha 0}}{dt} = 2\pi i q^2 \int d^3 k \left[ A + \frac{1}{P} \left( 1 - \frac{k_{\parallel} v_{\parallel}}{\omega} \right) \right] \left[ \frac{\epsilon_{kR}}{k v_{\parallel} + \omega_{c\alpha} - \omega} + \frac{\epsilon_{kL}}{k v_{\parallel} - \omega_{c\alpha} - \omega} \right] A f_0 \quad (\text{B.36})$$

This may be written in the more symmetric form (we let  $k_{\parallel} = k$  for convenience of notation)

$$\frac{df_{\alpha 0}}{dt} = 2\pi i q^2 \int d^3 k \frac{1}{P_1} \left[ \frac{k v_{\parallel}}{\omega} \frac{\partial}{\partial p_{\parallel}} + \left( 1 - \frac{k v_{\parallel}}{\omega} \right) \frac{\partial}{\partial p_{\perp}} \right] \left\{ P_1 \left( \frac{\epsilon_{kR}}{k v_{\parallel} + \omega_{c\alpha} - \omega} + \frac{\epsilon_{kL}}{k v_{\parallel} - \omega_{c\alpha} - \omega} \right) \left[ \frac{k v_{\parallel}}{\omega} \frac{\partial}{\partial p_{\parallel}} + \left( 1 - \frac{k v_{\parallel}}{\omega} \right) \frac{\partial}{\partial p_{\perp}} \right] f_0 \right\} \quad (\text{B.37})$$

The dispersion relation which relates  $\omega$  and  $k$  in equation B.37 must be determined before B.37 may be evaluated

The dispersion relation is determined by standard techniques of linear plasma theory. Using Maxwell's equations with the assumption of transverse waves it is easy to determine that

$$\left(\frac{c^2 k^2}{\omega^2} - 1\right) \underline{E}_{\perp k}(\omega) + \frac{4\pi}{i\omega} \sum_{\alpha} q_{\alpha} n_{\alpha} \int d^3 p_{\perp} v_{\perp} f_{\perp \alpha k}(\underline{p}, \omega) = 0 \quad (\text{B.38})$$

where  $n_{\alpha}$  is the density of the  $\alpha$ -species.

$$\text{With } \underline{v} = v_{\perp} (e^{i\phi} \hat{e}_R + e^{-i\phi} \hat{e}_L) + v_{\parallel} \hat{k} \text{ and}$$

$\underline{E} = E_R \hat{e}_R + E_L \hat{e}_L$ , where  $\hat{e}_R$  and  $\hat{e}_L$  are the basis vectors for the right and left hand circular representations. Equating vectors component wise (B.38) becomes

$$\left(1 - \frac{c^2 k^2}{\omega^2}\right) - \frac{4\pi}{i\omega} \sum_{\alpha} q_{\alpha} n_{\alpha} \int d^3 p_{\perp} v_{\perp} e^{i\phi} f_{\alpha k} = 0 \quad (\text{B.39})$$

$$\left(1 - \frac{c^2 k^2}{\omega^2}\right) - \frac{4\pi}{i} \sum_{\alpha} q_{\alpha} n_{\alpha} \int d^3 p_{\perp} v_{\perp} e^{-i\phi} f_{\alpha k} = 0$$

We will integrate over  $\phi$  in equations (B.39) in which

$$d^3 p = p_{\perp} dp_{\perp} dp_{\parallel} d\phi$$

as in equation (B.32) cross terms of the form  $e^{2i\phi}$  and  $e^{-2i\phi}$  drop

out and we are left with the Landau dielectric for R and L mode cyclotron waves

$$D_{\text{FL}}(k, \omega) = 1 - \frac{c^2 k^2}{\omega^2} - \frac{\pi}{\omega} \sum_{\alpha} \omega_{\text{p}\alpha}^2 m_{\alpha} \times \quad (\text{B.40})$$

$$\int_{\text{P}_L} dp_L dp_{\perp} dp_{\parallel} \left\{ \frac{kv_{\parallel}}{\omega} \frac{\partial f_{\alpha 0}}{\partial p_{\parallel}} + \left( 1 - \frac{kv_{\parallel}}{\omega} \right) \frac{\partial f_{\alpha 0}}{\partial p_{\perp}} \right\} \frac{v_{\perp}}{kv_{\parallel} \pm \omega_{\text{c}\alpha} - \omega}$$

The plasma frequency of species- $\alpha$  is given by

$$\omega_{\text{p}\alpha}^2 = \frac{4\pi n_{\alpha} q^2}{m_{\alpha}}$$

The standard approximation requires that  $\omega_{\text{I}} \ll \omega_{\text{E}}$  so that  $D(k, \omega)$  may be expanded in a power series in  $\omega_{\text{I}}$  giving the value of  $\omega_{\text{I}}$  as

$$\omega_{\text{I}} = \frac{-D_{\text{I}}}{\frac{\partial D_{\text{R}}}{\partial \omega_{\text{R}}}} \quad (\text{B.41})$$

We have taken  $D = D_{\text{R}} + iD_{\text{I}}$ . The imaginary part of  $D(k, \omega)$  comes from the  $p$  integration in equation (B.40) where the relation

$$\lim_{\omega_{\text{I}} \rightarrow 0} \int dp_{\parallel} \frac{F(p_{\parallel})}{kv_{\parallel} \pm \omega_{\text{c}\alpha} - \omega} = \int_{\text{P}} \frac{F(p_{\parallel})}{kv_{\parallel} \pm \omega_{\text{c}\alpha} - \omega} + \frac{i\pi \gamma m_{\alpha} F(p_{\parallel})}{|k|} \Big|_{p_{\parallel} = \text{P}_R} \quad (\text{B.42})$$

with  $\int$  as the Cauchy principal value and  $\text{P}_R = \gamma m_{\alpha} \left( \frac{\omega - \omega_{\text{c}\alpha}}{k} \right)$ , determines  $D_{\text{I}}$ .

Using relations B.40, B.41, and B.42 we determine

(B.43)

$$D_I = \frac{-\pi^2}{|k|\omega} \sum_{\alpha} \omega_{p\alpha}^2 \int \gamma_{p\alpha} dp_{\alpha} \left\{ \frac{kv_{\alpha}}{\omega} \frac{\partial f_{\alpha 0}}{\partial p_{\alpha}} + \left( 1 - \frac{kv_{\parallel}}{\omega} \right) \frac{\partial f_{\alpha 0}}{\partial p_{\parallel}} \right\} v_{\alpha} \Big|_{p_{\alpha} = p_R}$$

At this point we consider that we have three plasma components, a relatively cold electron and proton gas (at about 2000°K) and a super thermal electron component. We will assume that there is over all charge neutrality with

$$n_{ec} \approx n_{pc} = n_0$$

and

(B.43)

$$n_{eH} = n_1 \ll n_0$$

where  $n_{ec}$ ,  $n_{pc}$  and  $n_{eH}$  are the respective densities of the cold electron, cold proton and super thermal electron components. Conditions B.43 allow us to take the real part of the dielectric  $D_R(k, \omega)$  strictly from the cold plasma components and the imaginary part of the dielectric  $D_I$  strictly from the super thermal component. (Montgomery and Tidman, 1964). We arrive finally then at the relations

$$D_R(k, \omega) = 1 - \frac{\omega_{pe}^2}{\omega(\omega + \Omega_{ce})} - \frac{\omega_{pi}^2}{\omega(\omega + \Omega_{ci})} - \frac{k_{ce}^2}{\omega^2} = 0 \quad (B.44)$$

and with  $\Omega_{cd} = \frac{eB}{m_{\alpha}c}$

$$\omega_I(k, \omega) = \frac{\pi^2 \omega_{pe}^2 \int p_{\perp}^2 dp_{\perp} \left\{ \frac{\partial f_{eo}}{\partial p_{\perp}} - \frac{k}{\omega} \left( v_{\perp} \frac{\partial f_{eo}}{\partial p_{\parallel}} - v_{\parallel} \frac{\partial f_{eo}}{\partial p_{\perp}} \right) \right\} \Big|_{p_{\parallel} = p_R}}{|k| \left( \frac{2k_c^2}{\omega^2} + \frac{\omega_{pe}^2 (2\omega - \omega_{ce})}{(\omega_{ci} + \omega)^2 (\omega_{ce} - \omega)^2} \right)} \quad (B.45)$$

We not return to equation (B.37) which we will further specialize.

Letting

$$d^3k = 2\pi k_{\perp} dk_{\perp} dk_{\parallel}$$

and formally defining

$$\epsilon_{k_{\parallel}} = 2\pi \int_0^{\infty} \epsilon_k k_{\perp} d_{\perp} \quad (B.47)$$

Equation (B.37) then becomes.

$$\begin{aligned} \frac{df_{eo}}{dt} = 2\pi e^2 \int_{-\infty}^{\infty} dk \frac{1}{p_{\perp}} \left( \left[ \frac{kv_{\perp}}{\omega_R} \frac{\partial}{\partial p_{\parallel}} + \left( 1 - \frac{kv_{\parallel}}{\omega_R} \right) \frac{\partial}{\partial p_{\perp}} \right] \right) \Bigg\} p_{\perp} \quad (\otimes) \\ \left( \frac{\epsilon_{KR}}{kv_{\parallel} + \omega_{ce} - \omega} + \frac{\epsilon_{KL}}{kv_{\parallel} - \omega_{ce} - \omega} \right) \left[ \frac{kv_{\perp}}{\omega_R} \frac{\partial}{\partial p_{\parallel}} + \left( 1 - \frac{kv_{\parallel}}{\omega_R} \right) \frac{\partial}{\partial p_{\perp}} \right] f_{oe} \Bigg\} + \\ \left[ \frac{-kv_{\perp}}{\omega_R(-k)} \frac{\partial}{\partial p_{\parallel}} + \left( 1 - \frac{-kv_{\parallel}}{\omega_R(-k)} \right) \frac{\partial}{\partial p_{\perp}} \right] \Bigg\} p_{\perp} \quad (\otimes) \\ \left( \frac{\epsilon_{-kR}}{-kv_{\parallel} + \omega_{ce} - \omega(-k)} + \frac{\epsilon_{-kL}}{-kv_{\parallel} - \omega_{ce} - \omega(-k)} \right) \left[ \frac{-kv_{\perp}}{\omega_R(-k)} \frac{\partial}{\partial p_{\parallel}} + \left( 1 - \frac{-kv_{\parallel}}{\omega_R(-k)} \right) \frac{\partial}{\partial p_{\perp}} \right] f_{oe} \Bigg\} \end{aligned} \quad (B.48)$$

With the symmetry relations

$$\omega_R(x,t) = -\omega_R(-k,t)$$

$$\omega_I(k,t) = +\omega_I(-k,t)$$

and

(B.49)

$$\epsilon_{-kL} = \epsilon_{kR}$$

$$\epsilon_{-kR} = \epsilon_{kL}$$

(Krall and Trivelpiece, 1973), we see that the terms under the integral cancel except for their imaginary parts.

To this point we have retained the LH-mode denominator because as we see it provides the term necessary to cancel the real term under the integral in equation (B.48). This guarantees that the term on the right hand side is completely real. When we determine the imaginary part of (B.48) with the help of relation (B.42) we obtain four terms; two terms for RH-mode and two terms for LH-mode. At this point we may drop the LH-mode since it makes no further contribution. Equation (B.48) now may be written (again  $k = k$ )

$$\begin{aligned} \frac{df_{eo}}{dt} = & + 4\pi e^2 \int_{-\infty}^{\infty} \left( \frac{1}{p_{\perp}} \left\{ \frac{kv_{\perp}}{\omega} \frac{\partial}{\partial p_{\perp}} + \left( 1 - \frac{kv_{\parallel}}{\omega} \right) \frac{\partial}{\partial p_{\parallel}} \right\} \left\{ p_{\perp} \epsilon_k \omega_I \right. \right. \\ & \left. \left. \frac{1}{(kv_{\parallel} + \omega_{ce} - \omega)^2 + \omega_I^2} \left[ \frac{kv_{\perp}}{\omega} \frac{\partial}{\partial p_{\perp}} + \left( 1 - \frac{kv_{\parallel}}{\omega} \right) \frac{\partial}{\partial p_{\parallel}} \right] f_{oe} \right\} \right) \\ & + \frac{4\pi^2 e^2}{|v_{\parallel}|} k^2 d\Omega_k \left[ \frac{1}{p_{\perp}} \left\{ \frac{kv_{\perp}}{\omega} \frac{\partial}{\partial p_{\perp}} + \left( 1 - \frac{kv_{\parallel}}{\omega} \right) \frac{\partial}{\partial p_{\parallel}} \right\} \left\{ p_{\perp} \epsilon_k \right. \right. \\ & \left. \left. \left( \frac{kv_{\perp}}{\omega} \frac{\partial}{\partial p_{\perp}} + \left( 1 - \frac{kv_{\parallel}}{\omega} \right) \frac{\partial}{\partial p_{\parallel}} \right) f_{oe} \right] \Big|_k = \frac{\omega - \omega_{ce}}{v_{\parallel}} \right. \end{aligned} \quad \text{(B.50)}$$

The first term (which is under the integral) is referred to as the non-resonant diffusion term and the second term (which is not under the integral) is referred to as the resonant diffusion term.

We use equations (B.50) and (B.45) as the starting point for our discussion in the text.

## SELECTED BIBLIOGRAPHY

- Akasofu, S., Polar and Magnetospheric Substorms, Springer-Verlag, New York Inc., New York, 1968.
- Ansari, Z. A., A peculiar type of daytime absorption in the auroral zone, J. Geophys. Res., 70, 3117, 1965.
- Bailey, D. K. and M. A. Pomerantz, Relativistic electron precipitation into the mesosphere at subauroral latitudes, J. Geophys. Res., 70, 5823, 1965.
- Bailey, D. K., Some quantitative aspects of electron precipitation in and near the auroral zone, Reviews of Geoph., 6, 289, 1968.
- Bendat, J. S. and A. G. Piersol, Measurement and Analysis of Random Data, John-Wiley and Sons, Inc., New York, 1966.
- Berger, M. J., and S. M. Seltzwe, Studies in penetration of charged particles in matter, Nuclear Sci. Series, Report #39, Commission on Nuclear Science, National Academy of Science, NRC Commission on Nuclear Science pub. 1133, 1964.
- Berger, M. J., and S. M. Seltzer, Penetration of electrons and associated Bremsstrahlung through aluminum targets, Protection Against Space Radiation, NASA SP-169, 20, 1968.
- Berger, M. J. and S. M. Seltzer, Bremsstrahlung in the atmosphere, J. Atmospheric and Terrestrial Physics, 34, 85, 1972.
- Berger, M. J., S. M. Seltzer, and K. Maeda, Energy deposition by auroral electrons in the atmosphere, J. Atmospheric and Terrestrial Physics, 32, 1015, 1970.
- Berger, M. J., S. M. Seltzer, and K. Maeda, Some new results on electron transport in the atmosphere, to be published in J. Atmospheric and Terrestrial Physics, 1975.
- Berger, M. J., S. M. Seltzer, S. E. Chappell, J. C. Humphreys, and J. W. Motz, Table of Response Functions for Silicon Electron Detectors, NBS Technical Note 489, 1969.
- Bethe, H., Theorie des durchgangs schneller korpuskular-strahlen durch materie, Annalen der Physik, 5, 325, 1930.
- Bogott, F. H., and F. S. Mozer, Drifting energetic particle bunches observed on ATS 5, J. Geophys. Res., 75, 1825, 1974.
- Brice, N., Harnessing the energy in the radiation belts, J. Geophys. Res., 76, 4698, 1971.
- Brice, N., and C. Lucas, Influence of magnetospheric convection and polar wind on loss of electrons from the outer radiation belts,



- J. Geophys. Res., 76, 900, 1971.
- Buechner, W. W., R. J. Van de Graaff, E. A. Burrill, and A. Sperduto, Thick-target x-ray production from 1250 to 2350 kilovolts, Physical Review, 74, 1348, 1948.
- Carpenter, D. L., Whistler studies of plasmopause in the magnetosphere, J. Geophys. Res., 71, 693, 1966.
- Carpenter, D. L., and R. L. Smith, Whistler measurements of electron density in the magnetosphere, Reviews Geophys., 2, 415, 1964.
- Chappel, C. R., K. K. Harris, and G. W. Sharp, A study of the influence of magnetic activity on the location of the plasmopause as measured by OGO 5, J. Geophys. Res., 75, 50, 1970.
- Chappel, C. R., K. K. Harris, and G. W. Sharp, The dayside of the plasmopause, J. Geophys. Res., 76, 7632, 1971.
- Cocke, W. J., and J. H. Cornwall, Theoretical simulation of micro-pulsations, J. Geophys. Res., 72, 2843, 1967.
- Cornwall, J. W., F. V. Coroniti, and R. M. Thorne, Turbulent loss of ring current protons, J. Geophys. Res., 75, 4699, 1970.
- Coroniti, F. V., and C. F. Kennel, Electron precipitation pulsations, J. Geophys. Res., 75, 1279, 1970.
- Coroniti, F. V., R. W. Fredricks and R. White, Instability of ring current protons beyond the plasmopause during injection events, J. Geophys. Res., 77, 6243, 1972.
- Davidson, R. C., and D. A. Hammer, Nonequilibrium energy constants associated with large-amplitude electron whistlers, Physics of Fluids, 15, 1282, 1972.
- Dearnaley, G., and D. L. Northrop, Semiconductor Counters for Nuclear Radiations, John Wiley & Sons, Inc., New York, 1966.
- Dessler, A. J., Solar wind interactions and the magnetosphere, Physics of the Magnetosphere, Ed. R. L. Carovillano, J. F. McClay, and H. R. Radoski, D. Reidel Publishing Company, Dordrecht, Holland, 1968.
- Drummond, N. E., Quasilinear theory of plasma turbulence, Plasma Physics, International Atomic Energy Agency, Vienna, 1965.
- Drummond, N. W., and D. Pines, Non-linear stability of plasma oscillations, Nuclear Fusion, Suppl, Part 3, 1049, 1962.
- Engle, R. D. Non-linear stability of the extraordinary wave in the plasma, Physics of Fluids, 8, 939, 1965
- Feldstein, Y. I., Polar auroras, polar substorms, and their relationships with the dynamics of the magnetosphere, Proceedings of the

International Symposium on the Physics of the Magnetosphere, Ed. D. J. Williams and G. D. Mead, American Geophysical Union, 1968.

- Gendrin, R. J., Pitch angle diffusion of low energy protons due to gyroresonant wave interactions, J. Atmospheric and Terrestrial Physics, 30, 1313, 1968.
- Goldstein, H., Classical Mechanics, Addison-Wesley, New York, 1950.
- Hardy, A. C., M. D. Lopez, and T. T. White, A parametric technique of computing primary electron dose, Trans. American Nuclear Soc., 10, 383, 1967.
- Hass, G., W. R. Hunter, and R. Tousey, Reflectance of evaporated Aluminum in the vacuum ultraviolet, J. Optical Soc. American, 46, 1009, 1956.
- Hass, G., and J. E. Waylonis, Optical constants and reflectance and transmittance of evaporated aluminum in the visible and ultraviolet, J. Optical Soc. America, 51, 719, 1961.
- Hillas, A. M., Cosmic Rays, Pergamon Press, Oxford, 1972.
- Kanter, H., Electron scattering by thin foils for energies below 10 kev, Physical Review, 121, 461, 1961.
- Kennel, C. F., Low frequency whistler mode, Physics of Fluids, 9, 2190 1966.
- Kennel, C. F., Consequences of a magnetospheric plasma, Reviews of Geophys., 7, 379, 1969.
- Kennel, C. F., and R. D. Englemann, Velocity space diffusion from weak plasma turbulence in a magnetic field, Physics of Fluids, 9, 2377, 1966.
- Kennel, C. F., and H. E. Petschek, Limit on stably trapped particle fluxes, J. Geophys. Res., 71, 1, 1966.
- Kobetich, E. J., and R. Katz, Energy deposition by electron beams and delta-rays, Physical Review, 170, 170, 1968.
- Kock, H. M., and J. W. Motz, Bremsstrahlung cross-section formulas and related data, Reviews of Modern Physics, 31, 920, 1947.
- Krall, N. W., and A. W. Trivelpiece, Principles of Plasma Physics McGraw Hill Book Co., New York, 1973.
- Leipunskii, O. I. B. V. Novozhilov, and V. N. Sakharov, The Propagation of Gamma Quanta in Matter, Vol. 6, Pergamon Press, 1965.
- Lerche, I., Space charge waves and isotropy of the Galactic cosmic ray plasma, Physics of Fluids, 10, 1071, 1967.

- Lezniak, T. W., and J. R. Winckler, Structure of the magnetopause at  $6.6 R_E$  in terms of 50 to 150 keV electrons, J. Geophys. Res., 73, 5733, 1968.
- Lezniak, T. W., and J. R. Winckler, Experimental study of magnetospheric motions and the acceleration of energetic electron during substorms, J. Geophys. Res., 75, 7075, 1970.
- Liemohn, H., VLF and ULF whistler amplification, J. Geophys. Res., 72, 39, 1967.
- Little, C. G. and H. Lembach, Some measurement of high-latitude ionospheric absorption using extraterrestrial radio waves, Proc. I. R. E., 46, 334, 1958.
- Lyons, L., and R. M. Thorne, The magnetospheric reflection of whistlers, Planetary and Space Science, 18, 1753, 1970.
- Lyons, L., and R. M. Thorne, Parasitic pitch angle diffusion of radiation belt particles by ion cyclotron waves, J. Geophys. Res., 77, 5608, 1972.
- Lyons, L., R. M. Thorne and C. F. Kennel, Electron pitch-angle diffusion driven by oblique whistler-mode turbulence, J. Plasma Physics, 6, 589, 1971.
- Lyons, L., R. M. Thorne and C. F. Kennel, Pitch-angle diffusion of radiation belt electrons within the plasmasphere, J. Geophys. Res., 77, 3455, 1972.
- Meada, K., Diffusion of low energy electrons in the atmosphere, J. Atmospheric and Terrestrial Physics, 27, 259, 1965.
- Matthews, D. L., and D. J. Simons, Observations of relativistic electron precipitation at L=6, J. Geophys. Res., 78, 7539, 1973.
- Miller, W., J. W. Motz, and C. Cialella, Thick-target bremsstrahlung spectra for 1.00, 1.25, and 1.40 MeV electrons, Physical Review, 96, 1344, 1954.
- Montgomery, D., and D. A. Tidman, Plasma Kinetic Theory, McGraw-Hill, New York, 1964.
- Mozer, F. S., Particle-flux limits in synchronous orbit, J. Geophys. Res., 77, 2401, 1972.
- Ness, N. F., The geomagnetic tail, Magnetospheric Physics: Proc. of the International Symposium on the Physics of the Magnetosphere, Ed. D. J. Williams and G. D. Mead, American Geophysical Union, 1968.
- Northcliffe, L. C., and R. F. Schilling, Range and stopping power tables for heavy ions, Nuclear Data Tables A7, 233, 1970.

- Ortner, J., and W. Riedler, A smooth type of cosmic noise absorption, Nature, 204, 1181, 1964.
- Ossakow, S. L., E. Ott and I. Haber, Theory and computer simulation of whistler turbulence and velocity space diffusion in the magnetospheric plasma, J. Geophys. Res., 78, 2945, 1973.
- Parks, G. K., and J. R. Winckler, Acceleration of energetic electrons observed at the synchronous altitude during magnetospheric substorms, J. Geophys. Res., 73, 5786, 1968.
- Pfitzer, K. A., and J. R. Winckler, Experimental observation of large addition to the electron inner radiation belt after a solar flare event, J. Geophys. Res., 73, 5792, 1968.
- Rester, D. H., W. E. Dance and J. H. Derrickson, Thick target bremsstrahlung produced in electron bombardment of targets of Be, Sn, and Au in the energy range 0.2-2.8 Mev, Journal of Applied Physics, 41, 568, 1970.
- Roberts, C. S., Pitch-angle diffusion of electrons in the magnetosphere, Reviews of Geophysics and Space Physics, 7, 305, 1969.
- Roberts, C. S., and M. Schulz, Bounce resonant scattering of particles trapped in the Earth's magnetospheric field, J. Geophys. Res., 73, 7361, 1968.
- Rosenberg, T. J., L. J. Lanzerotti, D. K. Bailey, and J. D. Pierson, Energy spectra in relativistic electron precipitation events, Journal of Atmospheric and Terrestrial Physics, 34, 1977, 1972.
- Rossi, B., and S. Olbert, Introduction to the Physics of Space, McGraw-Hill Book Company, 1970.
- Roux, A., and J. Solomon, Self-consistent solution of the quasi-linear theory. Application to the spectral shape of the VLF waves in the magnetosphere, Journal of Atmospheric and Terrestrial Physics, 33, 1457, 1971.
- Sen, H. K., and A. A. Wyller, Generalization of the Appleton-Hartue magneto-ionic formula, Phys. Rev. Lett., 4, 355, 1960.
- Stassinopoulos, E. G., World Maps and Constant B, L, and FLUX Contours, NASA-SP-3054, NASA, Greenbelt, Md., 1968.
- Taylor, J. M., Semiconductor Particle Detectors, Butterworth Inc., Washington, 1963.
- Thorne, R. M., Unducted whistler evidence for secondary peak in the electron energy spectrum near 10 kev, J. Geophys. Res., 73, 4895, 1968.
- Thorne, R. M., A possible cause of dayside relativistic electron

precipitation events, Journal of Atmospheric and Terrestrial Physics, 36, 635, 1974

Thorne, R. M., and C. F. Kennel, Relativistic electron precipitation during magnetic storm main phase, J. Geophys. Res., 76, 4446, 1971.

Thorne, R. M., and C. F. Kennel, Locating the magnetospheric ring current, Comments Astrophys. and Space Science, 3, 115, 1971.

Thorne, R. M., E. J. Smith, R. K. Burton, and R. E. Holzer, Banded hiss emission from the plasmopause, J. Geophys. Res., 78, 1581, 1973.

Tverskoi, B. A., Theory of turbulent acceleration of charged particles in a plasma, JETP, 26, 1032, 1963.

Van Allen, J. A., Charged particles in the Magnetosphere, Magnetospheric Physics: Proc. of the International Symposium on the Physics of the Magnetosphere, Ed. D. J. Williams and G. D. Mead, American Geophysical Union, 1968.

Wecker, F., Neue messungen der absorption ruckdiffusion und sekundarstrahlenegung mittelschneller kathodenstrahlen in aluminum und gold, Annaleon der Physik, 40, 405, 1941.

Whittaker, E. T., and G. N. Watson, A Course of Modern Analysis, Cambridge University Press, 1965.

Wiley, R. E., and F. D. Barish, Plots of Geomagnetic Field Geometry, Technical Report No. AFWL-TR-69-144, Air Force Weapons Laboratory, Albuquerque, New Mexico, 1966.

Williams, D. J. and L. R. Lyons, The proton ring current and its interaction with the plasmopause: storm recovery phase, J. Geophys. Res., 79, 4195, 1974.

Williams D. J., and L. R. Lyons, Further aspects of the proton ring current interaction with the plasmopause: main and recovery phases, J. Geophys. Res., (to be published 1975).

Williamson, C., and J. P. Bougot, Tables of range and rate of energy loss of charged particles of energy .5 to 150 Mev, Rappt. CEA 2189, Centre Etudes Nucl., Saclay, France, 1962.

Yakimenko, V. L., Absorption of waves in a plasma (quasi-linear approximation), JETP, 17, 1032, 1963.

VITA

Name: David Jay Simons

Permanent address: 85 Joya Loop, Los Alamos, New Mexico, 87544

Degree and date to be conferred: Ph.D., 1975

Date of birth: [REDACTED]

Place of birth: [REDACTED]

Secondary education: Forest Hills High School, New York, N. Y.,

U. S. Grant High School, Los Angeles, Calif., 1961.

Collegiate institutions attended	Dates	Degree	Date of Degree
University of California, Berkely	1961-1966	AB	1966
University of Maryland, College Park	1969-1975	Ph.D.	1975

Major: Astrophysics and Geophysics

Minor: General Physics

Publications and Presentations to Learned Societies:

Matthews, D. L. and D. J. Simons, Observations of relativistic electron precipitation at  $L=6$ , J. Geophys. Res., 78, 7539, 1976.

Simons, D. J. and D. L. Matthews, Detailed Measurement of energetic electrons in a REP event, EOS, 54 Transactions, American Geophysical Union, 421, 1973.

Pongratz, M. B., K. Papadopoulos, and D. J. Simons, Observations of the bump-in tail instability in auroral electrons, EOS, Transactions, American Geophysical Union, 54, 421, 1973.

Simons, D. J., and D. L. Matthews, Production of relativistic electrons on  $L=6$  during times of post substorm electron density, EOS, 56, Transactions, American Geophysical Union, 1174, 1974.

Pongratz, M. B., J. Wolcott, C. Keady, and D. J. Simons, Aircraft observations of equatorial nightglow emissions of atomic oxygen 6300 Å and 5577 Å, EOS, 56, Transactions, American Geophysical Union, 1152, 1974.

Positions held: Jan. 1963 to April 1967, Research Data Analyst, Lawrence Radiation Laboratory, University of California, Berkeley, California.

April 1967 to April 1969, United State Peace Corps Volunteer, U. S. Peace Corps, Lagos, Nigeria.

PRECEDING PAGE BLANK NOT FILMED

Positions held: September 1969 to Jan. 1971, Graduate Teaching Assistant, Department of Physics, University of Maryland, College Park, Maryland.

January 1971 to September 1974, Graduate Research Assistant, Institute for Fluid Dynamics and Applied Mathematics, University of Maryland, College Park Maryland.

September 1974 to present, Senior Scientist, EG & G, Inc., Los Alamos, New Mexico.